An Enquiry Concerning Charmless Semileptonic Decays of Bottom Mesons

A dissertation presented

by

Kris Somboon Chaisanguanthum

to

The Department of Physics

in partial fulfillment of the requirements
for the degree of
Doctor of Philosophy
in the subject of
Physics

Harvard University
Cambridge, Massachusetts

May 2008

Professor Masahiro Morii Kris Somboon Chaisanguanthum

An Enquiry Concerning Charmless Semileptonic Decays of Bottom Mesons

Abstract

The branching fractions for the decays $B \to P\ell\nu_\ell$, where P are the pseudoscalar charmless mesons $\pi^\pm$, π^0, η and η' and ℓ is an electron or muon, are measured with B^0 and $B^\pm$ mesons found in the recoil of a second B meson decaying as $B \to D\ell\nu_\ell$ or $B \to D^*\ell\nu_\ell$. The measurements are based on a data set of $348\,\mathrm{fb}^{-1}$ of e^+e^- collisions at $\sqrt{s} = 10.58\,\mathrm{GeV}$ recorded with the *BABAR* detector. Assuming isospin symmetry, measured pionic branching fractions are combined into

$$\mathcal{B}(B^0 \to \pi^-\ell^+\nu_\ell) = (1.54 \pm 0.17_{(\mathrm{stat})} \pm 0.09_{(\mathrm{syst})}) \times 10^{-4}.$$

First evidence of the $B^+ \to \eta\ell^+\nu_\ell$ decay is seen; its branching fraction is measured to be

$$\mathcal{B}(B^+ \to \eta\ell^+\nu_\ell) = (0.64 \pm 0.20_{(\mathrm{stat})} \pm 0.03_{(\mathrm{syst})}) \times 10^{-4}.$$

It is determined that

$$\mathcal{B}(B^+ \to \eta'\ell^+\nu_\ell) < 0.47 \times 10^{-4}$$

to 90% confidence. Partial branching fractions for the pionic decays in ranges of the momentum transfer and various published calculations of the $B \to \pi$ hadronic form factor are used to obtain values of the magnitude of the Cabibbo-Kobayashi-Maskawa matrix element V_{ub} between 3.61 and 4.07×10^{-3}.

Table of contents

Acknowledgements

Thank you,

...Masahiro Morii, without whose guidance and infinite patience this would not be possible. I am as surprised as you are that I've made it this far.

...Alan Weinstein, George Brandenburg, Michael Schmitt and Melissa Franklin, for whose tutelage and generosity over the years I will forever be indebted.

...all I've intersected in the Harvard *BABAR* group: Stephen, Eunil, Kevin, Jinwei, Corry.

...Maria, Caolionn, Ayana and Michael, for acknowledging me in their respective dissertations [1, 2, 3, 4] and for a plethora of other reasons into which I cannot go now.

...Tae Min, for letting me win (at graduating).

...the political dynasty of Jesse and Adam.

...Nathaniel and Wesley, my graduate school chums.

...my East Coast shorties, Victoria and Leah.

...Christie, my favorite lesbian, and Megan,[1] who comes in a respectable second.

...Millie and Rhiju, for, among other things, your hospitality in Seattle; I had a splendid time.

...Seth (Pants), for breaking all of my theories, and, also, Adele.

...Jared, my BFF; KIT, TCCIC, etc.

...Greg—hell yeah!

...Abigail, Cassandra, Barbara, Ryan and Jack, who have been like a family to me.

...Roslyn (and Paul), Mom, Michael[2] (and Marsha) and Dad, who have also been like a family to me.

[1] Megan Toby is my girlfriend.

[2] Thank you especially, Michael, for your insights on heavy quark effective theory, which proved instrumental in the development of §2.1.

in memoriam

Daniel Satchyu Weiss

(1979 - 2007)

The world is a better place for having known you.

Chapter 1

On the importance of $|V_{ub}|$

In the Standard Model of particle physics, the weak and electromagnetic interactions are described by a manifestly chiral $SU(2) \times U(1)$ gauge symmetry which is broken by a scalar Higgs field ϕ with a nonzero vacuum expectation value.

Where the fields W^a and B and coupling constants g and g' correspond to the $SU(2)$ and $U(1)$ components of the gauge group respectively, the covariant derivative D_μ of a fermion field with $U(1)$ charge y is given by

$$D_\mu = \partial_\mu - igW_\mu^a T^a - ig'yB_\mu; \tag{1.1}$$

T^a are $SU(2)$ generators[1] [5]. In this framework, left-handed quark fields are paired in doublets Q_{Li} in the spinor representation of $SU(2)$:

$$\begin{pmatrix} u_L \\ d_L \end{pmatrix}, \begin{pmatrix} c_L \\ s_L \end{pmatrix} \text{ and } \begin{pmatrix} t_L \\ b_L \end{pmatrix} \tag{1.2}$$

with $U(1)$ charge $y = 1/6$. Right-handed quark fields u_R, d_R, etc. are $SU(2)$ singlets and do

[1] We use the convention that, in the spinor representation, $T^1 = \frac{1}{2}\begin{pmatrix} 0 & 1 \\ 1 & 0 \end{pmatrix}$, $T^2 = \frac{1}{2}\begin{pmatrix} 0 & -i \\ i & 0 \end{pmatrix}$ and $T^3 = \frac{1}{2}\begin{pmatrix} 1 & 0 \\ 0 & -1 \end{pmatrix}$.

not couple to W^a. The covariant derivative leads to kinetic terms in the Lagrangian density:

$$\begin{aligned}\Delta\mathcal{L}_{\text{kinetic}} &= \overline{Q}_{Li}(i\gamma^\mu D_\mu)Q_{Li} \\ &= \cdots + g\gamma^\mu \overline{Q}_{Li} W^a_\mu T^a Q_{Li} + \cdots .\end{aligned} \tag{1.3}$$

Charged weak fields take the form $W^\pm = \frac{1}{\sqrt{2}}(W^1 \mp iW^2)$; the terms in Equation 1.3 describing the coupling of quarks to these fields, where $u_{Li} = u_L, c_L, t_L$ and so forth, are

$$\Delta\mathcal{L}_{\text{charged}} = \frac{g}{\sqrt{2}}\big(W^+_\mu(\overline{u}_{Li}\gamma^\mu d_{Li}) + W^-_\mu(\overline{d}_{Li}\gamma^\mu u_{Li})\big), \tag{1.4}$$

i.e., charged weak currents couple left-handed up-type and down-type quarks within the same doublet. Electromagnetic and neutral weak interactions, mediated by (linear combinations of) W^3 and B, do not change quark flavor.

The Cabbibo-Kobayashi-Maskawa matrix V_{CKM} arises from Yukawa coupling of quark fields to the Higgs field [6]; these interactions take the general form

$$\Delta\mathcal{L}_{\text{Yukawa}} = -Y^d_{ij}\overline{Q}_{Li}\phi d_{Rj} - Y^u_{ij}\overline{Q}_{Li}\epsilon\phi^* u_{Rj} + [\text{Hermitian conjugate}], \tag{1.5}$$

with ϵ the ($SU(2)$ spinor) antisymmetric tensor; $Y^{u,d}$ descibe the strength of the Yukawa couplings. The Higgs field takes a vacuum expectation value, written canonically, in the same representation, as the $SU(2)$ spinor $\langle\phi\rangle = (0, v/\sqrt{2})$; Equation 1.5 becomes

$$\Delta\mathcal{L}_{\text{Yukawa}} = \frac{v}{\sqrt{2}}\left(-Y^d_{ij}\overline{d}_{Li}d_{Rj} - Y^u_{ij}\overline{u}_{Li}u_{Rj}\right) + [\text{Hermitian conjugate}], \tag{1.6}$$

giving rise to quark mass matrices $M^{u,d} = vY^{u,d}/\sqrt{2}$, which can be diagonalized to $\tilde{M}^{u,d}$ via the transformation

$$\tilde{M}^{u,d} = V^{u,d}_L M^{u,d} V^{u,d\dagger}_R, \tag{1.7}$$

where $V^{u,d}_{L,R}$ are unitary matrices relating quark mass eigenstates $u'_{Li} \equiv (V^u_L)_{ij}u_{Lj}$, etc. to the natural weak flavor eigenstates as defined by the $SU(2)$ doublets described above. With the definition $V_{\text{CKM}} \equiv V^u_L V^{d\dagger}_L$, Equation 1.4 is written in terms of quark mass eigenstates as

$$\Delta\mathcal{L}_{\text{charged}} = \frac{g}{\sqrt{2}}\left(W^+_\mu \overline{u}'_{Li}(V_{\text{CKM}})_{ij}\gamma^\mu d'_{Lj} + W^-_\mu \overline{d}'_{Li}(V^\dagger_{\text{CKM}})_{ij}\gamma^\mu u'_{Lj}\right). \tag{1.8}$$

In this form, it is transparent that $V_{\rm CKM}$ describes quark mixing, i.e., weak coupling between different quark mass eigenstates; it is natural to write $V_{\rm CKM}$ as

$$V_{\rm CKM} \equiv \begin{pmatrix} V_{ud} & V_{us} & V_{ub} \\ V_{cd} & V_{cs} & V_{cb} \\ V_{td} & V_{ts} & V_{tb} \end{pmatrix}. \tag{1.9}$$

This Dissertation presents a measurement of the magnitude of V_{ub} and related quantities.

1.1 The violation of charge-parity symmetry

The mathematical operation of charge conjugation, C, conjugates particles' internal quantum numbers, effectively interchanging particles and antiparticles, e.g., $Cc_R = \overline{c}_R$. Parity reversal, P, inverts spatial coordinates of a system, one consequence of which is the reversal of the "handedness" of fermions, e.g., $Pc_R = c_L$. In the Standard Model, gravity, electromagnetism and strong interactions are invariant under each of these independently; weak interactions, which couple only left-handed fermions, are maximally asymmetric under C and P. The combined transformation CP was presumed to be a symmetry of weak interactions until 1964, when CP violation was first observed in K^0-$\overline{K}^0$ oscillations [7].

Since then, CP violation has been studied extensively. In addition to being a critical part of any complete description of particle interactions, it is of interest for its role in baryogenesis: the universe is known to consist almost entirely of matter; such a matter-antimatter imbalance is the result of CP-violating processes and/or such an imbalance present in the initial conditions of the universe. Furthermore, where T is the time reversal operator, the CPT theorem requires any Lorentz-invariant quantum field theory with a Hermitian Hamiltonian to be symmetric under CPT; CP violation implies T violation, i.e., a fundamental directionality of time.

The "traditional" Standard Model contains one[2] source of CP violation, the Yukawa couplings to the Higgs field, as described by $V_{\rm CKM}$. (The Standard Model can also be expanded to include a somewhat analogous CP-violating matrix describing neutrino oscillations [8].) As a 3×3 unitary matrix, $V_{\rm CKM}$ contains nine (real) parameters; five can be written as phases

[2]The preclusion of CP-violating interactions in the strong sector is not theoretical, but empirical. For example, were CP violation in the strong sector maximal, dimensional analysis suggests that the neutron would have an electric dipole moment, where e is the elementary charge, on the order of $e\hbar c/\Lambda_{\rm QCD} \sim 10^{-15} e\,\mathrm{m}$.

absorbed into the quark fields[3] and are thus nonphysical, leaving four effective parameters, commonly interpreted as three quark mixing angles and one CP-violating phase.

1.2 The unitarity of $V_{\rm CKM}$

With $\lambda \equiv V_{us} \approx 0.23$ [9] and unitarity constraints, $V_{\rm CKM}$ can be written with four real parameters,[4] to third order in λ, as [10]

$$V_{\rm CKM} = \begin{pmatrix} 1-\lambda^2/2 & \lambda & A\lambda^3(\rho - i\eta) \\ -\lambda & 1-\lambda^2/2 & A\lambda^2 \\ A\lambda^3(1-\rho-i\eta) & -A\lambda^2 & 1 \end{pmatrix}, \tag{1.10}$$

with a single CP-violating parameter η. It is known empirically that $A = \mathcal{O}(1)$. The unitarity of $V_{\rm CKM}$ also implies $\sum_k V_{ki} V_{kj}^* = \delta_{ij}$; taking $i = d$ and $j = b$ gives the relation

$$V_{ud}V_{ub}^* + V_{cd}V_{cb}^* + V_{td}V_{tb}^* = 0, \tag{1.11}$$

or, equivalently,

$$-\frac{V_{ud}V_{ub}^*}{V_{cd}V_{cb}^*} - \frac{V_{td}V_{tb}*}{V_{cd}V_{cb}^*} = 1. \tag{1.12}$$

With (real) $\overline{\rho}$ and $\overline{\eta}$ defined by $\overline{\rho} + i\overline{\eta} = -(V_{ud}V_{ub}^*)/(V_{cd}V_{cb}^*)$, to first order in λ, $\overline{\rho} \approx \rho$ and $\overline{\eta} \approx \eta$; this leads to the (most commonly studied) Unitarity Triangle, with vertices $(0,0)$, $(1,0)$ and $(\overline{\rho}, \overline{\eta})$.

This Unitarity Triangle is depicted in Figure 1.1; the lengths of the non-horizontal sides are $|(V_{ud}V_{ub}^*)/(V_{cd}V_{cb}^*)|$ (left) and $|(V_{td}V_{tb}^*)/(V_{cd}V_{cb}^*)|$ (right), and the angles, as defined in the Figure, are given by

$$\alpha = \arg\left(-\frac{V_{td}V_{tb}^*}{V_{ud}V_{ub}^*}\right), \; \beta = \arg\left(-\frac{V_{cd}V_{cb}^*}{V_{td}V_{tb}^*}\right) \text{ and } \gamma = \arg\left(-\frac{V_{ud}V_{ub}^*}{V_{cd}V_{cb}^*}\right). \tag{1.13}$$

[3] There are six quark fields; however, the global phase is constrained by unitarity.

[4] Specifically, $\lambda \equiv \frac{|V_{us}|}{\sqrt{|V_{ud}|^2+|V_{us}|^2}}$, $A \equiv \frac{1}{\lambda^2}\left|\frac{V_{cb}}{V_{us}}\right|$ and $\rho - i\eta \equiv \frac{V_{ub}}{A\lambda^3}$.

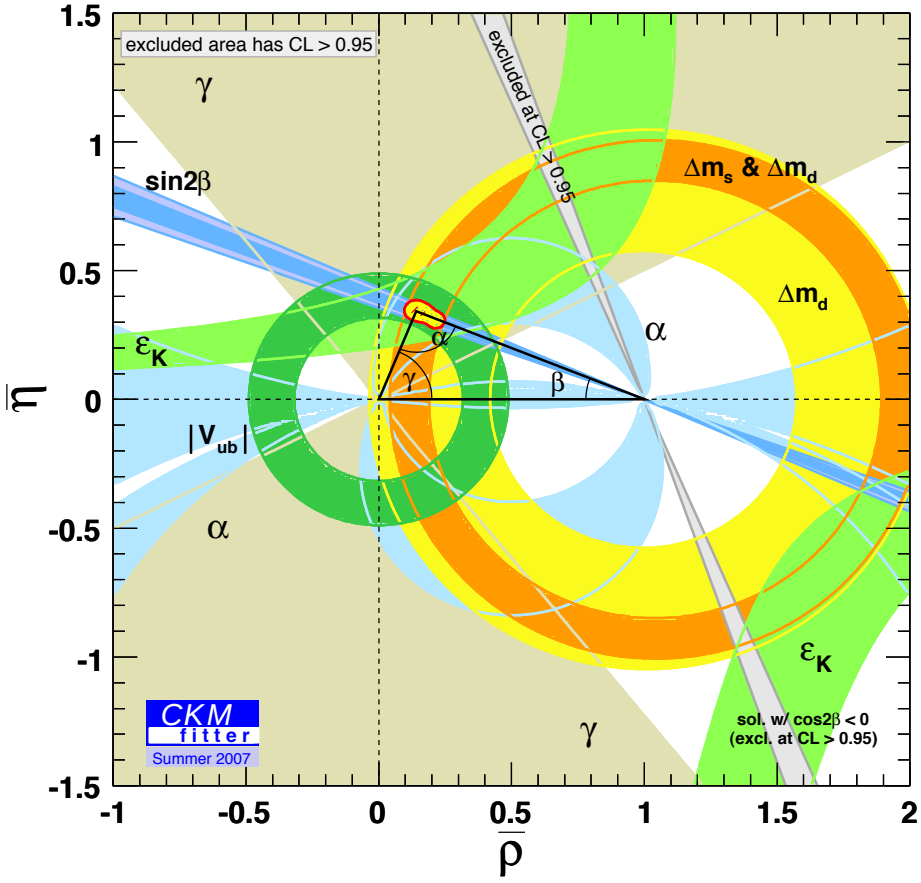

Figure 1.1: Current knowledge of the Unitarity Triangle. Shaded areas indicate 95% confidence regions for $(\overline{\rho}, \overline{\eta})$, as determined by various experimental results [11].

Thus the Triangle is overconstrained; measurements of its sides and angles—some of which can be measured through various processes, providing additional constraints—test the consistency of the Standard Model and are sensitive to new physics, e.g., additional sources of CP violation.

In particular, decays of B^0 mesons[5] to $c\bar{c}s$ CP eigenstates, e.g., $B^0 \to J/\psi K^0_S$, provide the cleanest channel through which CP asymmetry in the B meson system can be and has been, in the form of the parameter $\sin 2\beta$, studied [12]. The determination of $|V_{ub}|$, the least precisely known factor in the length of the side opposite β, provides a crucial complement to this measurement.

[5] "and corresponding charge conjugate(s)" is implied throughout this Dissertation.

Chapter 2

Phenomenological considerations

The magnitude of the Cabbibo-Kobayashi-Maskawa matrix element V_{ub} is most accessible, for both theoretical and experimental reasons, through the charmless semileptonic transition $b \to u\ell\nu$.[1] The quark level Feynman diagram is shown in Figure 2.1; due to hadronization, in practice this is observed as the decay $B \to X_u\ell\nu$, where X_u is one or more charmless particles. Measurements of $|V_{ub}|$ are either "exclusive," i.e., X_u is a final state meson that is explicitly reconstructed, or "inclusive" in which case the kinematics of an event are used to distinguish $b \to u\ell\nu$ decays from the (roughly 50 times) more copious $b \to c\ell\nu$ transition. Each method corroborates the other, our understanding of the Standard Model and our ability to make predictions from it, as the theoretical uncertainties arising from each method are orthogonal.

2.1 Inclusive charmless semileptonic decays

Due to the relative massiveness of final state charmed hadronic systems (the lightest of which is the D meson), the kinematic spectra of charmed and charmless semileptonic B decays differ significantly; inclusive $|V_{ub}|$ measurements typically rely on the extraction of $|V_{ub}|$ from the partial charmless decay rate in a charm-suppressed region of phase space. Typically considered, in a $B \to X\ell\nu$ decay, where X is a hadronic system, are the kinematic quantities: the energy E_ℓ of the lepton, the invariant mass m_X of the X system and/or q^2, the square of the momentum transfer: $q^2 \equiv (P_\ell + P_\nu)^2$, where P_i are the four-momenta of i.

At B factories such as *BABAR*, where $B\overline{B}$ meson pairs are produced and studied, such

[1] The lepton ℓ is defined to be either an electron or a muon, to allow the approximation of massless leptons; "$\mathcal{B}(B \to \pi\ell\nu)$" means $\mathcal{B}(B \to \pi e\nu)$ or $\mathcal{B}(B \to \pi\mu\nu)$ (not the sum), which, in this approximation, are equal.

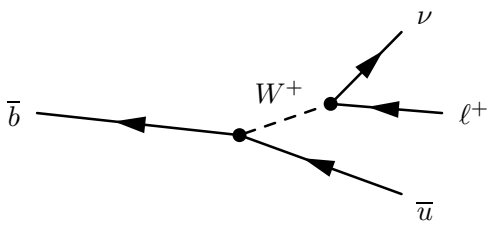

Figure 2.1: Quark level tree level Feynman diagram of charmless semileptonic decay of $\overline{b}$ (anti)quark (not to scale).

decays are observed via the lepton energy (E_ℓ) spectrum, specifically above the charm kinematic threshold [13]. In events where the neutrino from this semileptonic decay is the only unobserved particle, i.e., energy and momentum from the remainder of the $B\overline{B}$ event are fully recovered, the neutrino can be reconstructed and q^2 information added [14]; in analyses in which the recoil B meson is fully (hadronically) reconstructed, m_X spectra can considered as well, which is especially useful where $m_X < m_D$ [15].

Regardless of the measurement technique, the theoretical challenge is the same: the full charmless semileptonic B decay spectrum, i.e., the triple differential decay rate

$$\frac{d^3\Gamma(B \to X\ell\nu)}{dE_\ell dm_X dq^2} \tag{2.1}$$

(or appropriate integrals) for charmless X, must be sufficiently understood such that a measured (partial) decay rate can be translated into meaningful knowledge about $|V_{ub}|$. Heavy quark effective theory, which can be used to calculate this differential decay rate over much of the available phase space, is not directly applicable in the kinematic region where the $b \to c$ transition is forbidden. Here, nonperturbative physics is described in a "shape function," which, to leading order, is a universal property of B mesons and can thus be understood through the study of other physics processes such as $b \to c\ell\nu$ (as can heavy quark expansion parameters). Several prescriptions currently exist for extracting $|V_{ub}|$ from inclusive charmless B decays; theoretical uncerainties are typically $\sim 8\%$. Some current experimental results are shown in Figure 2.2.

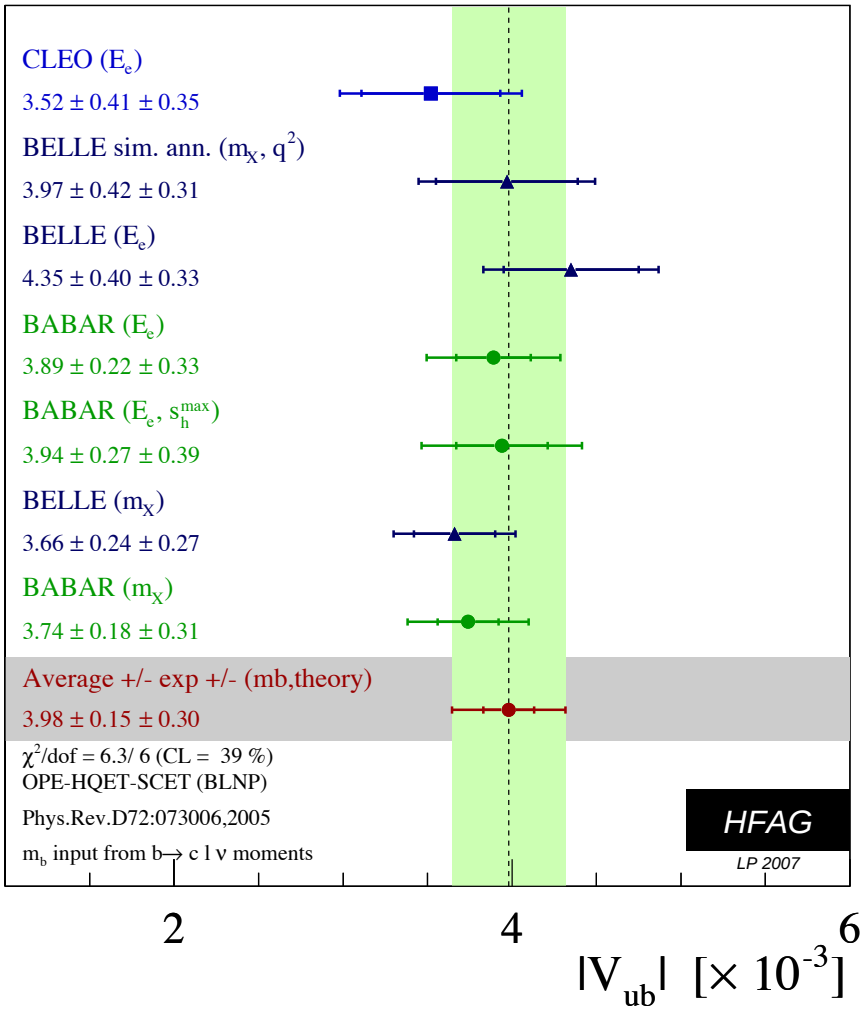

Figure 2.2: Current results and world average of $|V_{ub}|$ as determined through the measurement of inclusive chameless semileptonic decays [16]. Extraction of $|V_{ub}|$ proceeds by the method due to Lange, Neubert and Paz [17].

2.2 Exclusive charmless semileptonic decays

The determination of $|V_{ub}|$ through exclusive charmless semileptonic decays proceeds through the measurement of branching fractions $\mathcal{B}(B \to X_u \ell\nu)$ where X_u is a specific charmless meson, most commonly a pion. Such measurements can be "tagged," i.e., the charmless decay is found in the recoil of reconstructed B mesons, e.g., fully hadronically reconstructed B mesons ("$B_{\rm reco}$") [18]. Full event reconstruction offers exceptionally high signal purity, but a relatively small data sample.

In the opposite extreme, the decay $B \to X_u \ell\nu$ can be measured "untagged," i.e., without the explicit reconstruction of the recoil B meson [19]. In events such that all energy and momentum from the recoil B meson is recovered, the neutrino, and thus the kinematics of the $B \to X_u \ell\nu$ decay, can be reconstructed. Untagged measurements allow a larger sample at a cost of signal purity, which typically results in larger systematic uncertainies.

This Dissertation describes the measurement of exclusive charmless branching fractions $\mathcal{B}(B \to X_u \ell\nu)$, where X_u are the pseudoscalar mesons $\pi^{\pm}$, π^0, η and η', using an approach between the two extremes: charmless B decays are found using semileptonic tags ("SL tag"), i.e., in the recoil of B mesons decaying semileptonically as $B \to D^{(*)} \ell\nu$. The relatively high $B \to D^{(*)} \ell\nu$ branching fractions ($\sim$ 7-9% per lepton species [9]) provide a copious data set; however, event reconstruction is complicated by the presence of two neutrinos.

Current results for $\mathcal{B}(B \to \pi\ell\nu)$ are shown in Figure 2.3; fewer measurements of $\mathcal{B}(B^+ \to \eta^{(\prime)} \ell^+ \nu)$ exist. The decay $B^+ \to \eta \ell^+ \nu$ has not yet been observed with statistical significance.

For a(n exclusive) charmless semileptonic decay mode, the appropriate transition amplitude $\mathcal{M}$ relates experimentally measured branching fractions to $|V_{ub}|$. The components of $\mathcal{M}$ which are not exactly calculable are described by hadronic form factors $f_{\pm}^{\pi,\eta^{(\prime)}}$.

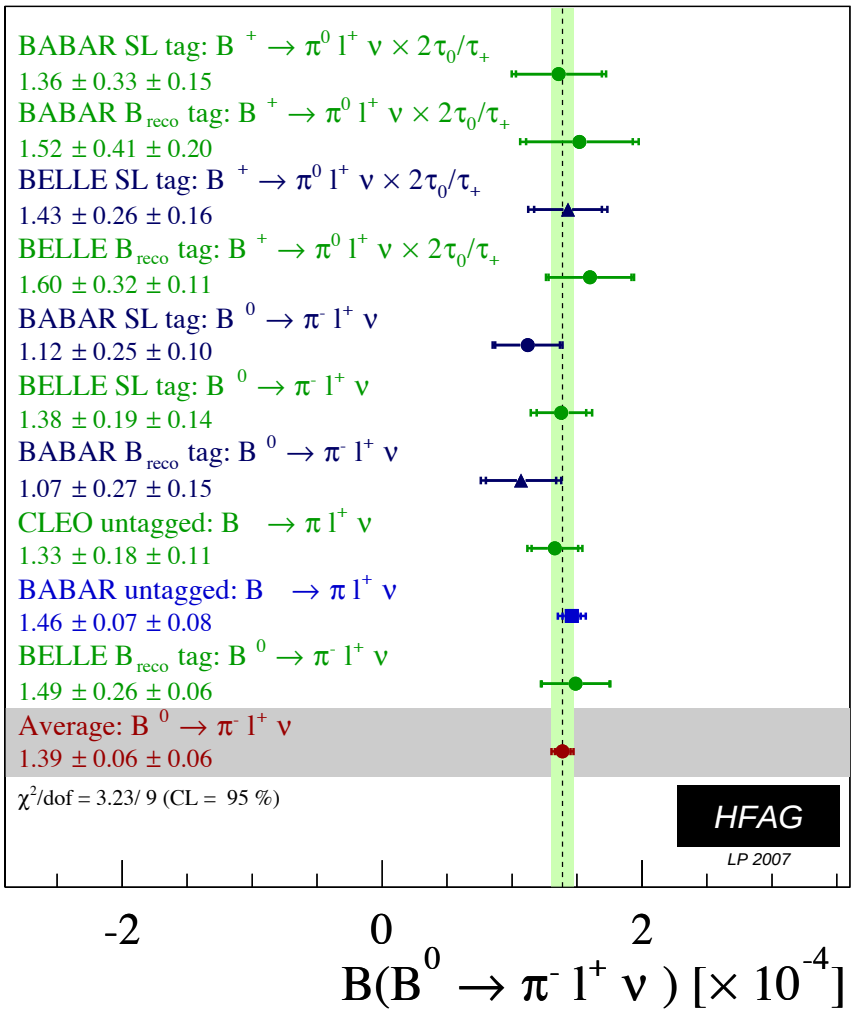

Figure 2.3: Current measurements and world average of $\mathcal{B}(B^0 \to \pi^- \ell^+ \nu)$ and $\mathcal{B}(B^+ \to \pi^0 \ell^+ \nu)$ expressed (using isospin symmetry) as $\mathcal{B}(B^0 \to \pi^- \ell^+ \nu)$ [16].

2.3 Hadronic form factors

As $m_B \ll m_W$, the amplitude $\mathcal{M}$ for a $B \to \pi \ell^+ \nu$ decay[2] is given by[3] [20]

$$\mathcal{M}(B \to \pi \ell^+ \nu) = \frac{G_{\mathrm{F}}}{\sqrt{2}} V_{ub}^* L_\mu H^\mu, \tag{2.2}$$

where G_{F} is the Fermi constant, and L (H) the leptonic (hadronic) current, i.e.,

$$L_\mu \equiv \overline{u}_\nu \gamma_\mu (1 - \gamma_5) v_\ell \text{ and} \tag{2.3}$$

$$H^\mu \equiv \langle \pi | \overline{u} \gamma^\mu (1 - \gamma_5) b | B \rangle \,, \tag{2.4}$$

where $\overline{u}_\nu$ and v_ℓ are Dirac spinors and b ($\overline{u}$) is the appropriate quark annihilation (creation) operator.

The leptonic current is known exactly; the hadronic current contains all relevant quantum chromodynamics (QCD) information and is consequently difficult to calculate. As B and π mesons are pseudoscalar, the hadronic current is purely axial and, as it must be Lorentz invariant (and there are only two independent vectors available), can be written

$$H^\mu = f_+^\pi(q^2)(P_B^\mu + P_\pi^\mu) + f_-^\pi(q^2) q^\mu, \tag{2.5}$$

where P_B and P_π are the appropriate four-momenta and $q \equiv P_B - P_\pi$ (so q^2 is defined in the usual way). In the limit $m_\ell \to 0$, $q^\mu L_\mu$ becomes negligible; in the electron and muon cases, effectively

$$H^\mu = f_+^\pi(q^2) \, (P_B^\mu + P_\pi^\mu) \,. \tag{2.6}$$

Analogous formulae can be written for $B^+ \to \eta \ell^+ \nu$ and $B^+ \to \eta' \ell^+ \nu$.

Understanding the form factors $f_+^{\pi,\eta^{(\prime)}}$ is critical to the extraction of $|V_{ub}|$ from measured branching fractions[4] as well as the realistic simulation of signal data.[5] A number of calculations of the pionic form factor f_+^π exist, some of which are described below. Extracted

[2] This is assumed to be, by isospin symmetry, the same for $B^0 \to \pi^- \ell^+ \nu$ and $B^+ \to \pi^0 \ell^+ \nu$.

[3] Some sources have an overall factor of $-i$.

[4] See Equation 10.9.

[5] See §5.2.1, §9.1.1.

via the current world average for $\mathcal{B}(B^+ \to \pi^- \ell\nu)$ and some more commonly used f_+^π calculations, $|V_{ub}|$ ranges between 3.17 and 3.82×10^{-3} [16].

2.3.1 Lattice quantum chromodynamics

The hadronic current can be calculated from first QCD principles through Monte Carlo evaluation of integrals in discretized spacetime. Such calculations are inherently less reliable in the low q^2 regime, where the de Broglie wavelength of the final state meson is small; with these form factor calculations, $|V_{ub}|$ is typically extracted from $B \to \pi\ell\nu$ decays with $q^2 \geq 16\ \text{GeV}^2/c^2$. Early "lattice QCD" calculations, due to computational restrictions, were made in the quenched approximation, i.e., ignoring quark loops.

In one such calculation, by the APE Collaboration [21], the form factor is parameterized[6] as

$$f_+^\pi(q^2) = \frac{c_B(1-\alpha_B)}{(1-q^2/m_{B^*}^2)(1-\alpha_B q^2/m_{B^*}^2)}, \tag{2.7}$$

(also written with $f_+^\pi(0) = c_B(1-\alpha_B)$) with m_{B^*} the mass of the B^* meson; fit parameters are found to be $c_B \approx 0.4$ and $\alpha_B \approx 0.4$ with uncertainties translating to a $\sim 25\%$ theoretical uncertainty on $|V_{ub}|$.

More recently, unquenched[7] lattice QCD calculations have been possible. One published by the FNAL collaboration [24] treats B meson dynamics[8] with an approach something of a tuned extrapolation between light and very massive meson extremes. They report $f_+^\pi(0) = 0.23 \pm 0.02$ and $\alpha_B = 0.63 \pm 0.05$, where the uncertainty is statistical. In addition, they cite an additional 11% theoretical uncertainty, which is dominated by uncertainties from discretization (9%), chiral extrapolation[9] (4%) and the parameterization of f_+^π (4%), on $|V_{ub}|$.

[6] Bećirević and Kaidalov [22] provide analytic parameterizations of form factors written in terms of the B^* pole and an additional effective pole, and taking into account physical constraints and scaling laws from heavy quark effective theories. However, these forms do not describe effects of hard gluon exchange as predicted by soft-collinear effective theory in the $q^2 \to 0$ regime [23].

[7] In the calculations discussed, unquenching considers three quark flavors: two very light ones and strange.

[8] Without explicit treatment (or a sufficiently fine lattice), the large B mass results in a large discretization uncertainty. The APE collaboration circumvented this by calculating form factors for an array of less massive (hypothetical) heavy mesons and extrapolating the result to the physical B mass.

[9] Calculation of a quark's loop effects grows increasingly computationally intensive as the

The HPQCD collaboration [25] published a similar unquenched lattice QCD calculation in which the dynamics of the B meson are modeled nonrelativistically. From this form factor calculation, a 14% theoretical uncertainty, the dominant contributions to which are associated with finite statistics and chiral extrapolation (10%) and matching lattice QCD field operators to continuum ones (9%), on $|V_{ub}|$ is expected.

2.3.2 Light-cone sum rules

The method of light-cone sum rules allows a complementary calculation of form factors for small q^2, the regime in which, due to the high momentum of the final state pion, correlation functions between the weak and B currents can be expanded around the light cone. Sum rules relate these correlation functions to form factors and other parameters, e.g., decay constants, which can be determined empirically or calculated by other means.

Ball and Zwicky [26] use this method and the parameterization

$$f_+^\pi(q^2) = \frac{r_1}{1 - q^2/m_{B^*}^2} + \frac{r_2}{1 - q^2/m_{\text{fit}}^2}; \tag{2.8}$$

assuming a b quark mass of $m_b = 4.8\,\text{GeV}/c^2$, they find $r_1 = 0.744$, $r_2 = -0.486$ and $m_{\text{fit}}^2 = 40.73\ (\text{GeV}/c^2)^2$. This form factor is presumed to be valid for $q^2 < 14\ \text{GeV}^2/c^2$, with 10-13% uncertainty at $q^2 = 0$.

2.3.3 Constituent quark model

The ISGW2 model [27] considers the form factor in terms of the underlying quark interaction in the nonrelativistic ($q^2 \to q_{\text{max}}^2$) limit—in this approximation, the form factor is calculable exactly—and adds perturbations for relativistic effects. The form factor is written, where r is the transition charge radius, with the ansatz

$$f_+^\pi(q^2) = f_+^\pi(q_{\text{max}}^2)\left(1 + \frac{r^2}{12}(q_{\text{max}}^2 - q^2)\right)^{-2}. \tag{2.9}$$

This model is not in agreement with current experimental results, and is not used to extract $|V_{ub}|$.

quark grows less massive; unquenching is typically done with $m_{u,d}$ set to unphysically heavy values, and physical results are extrapolated.

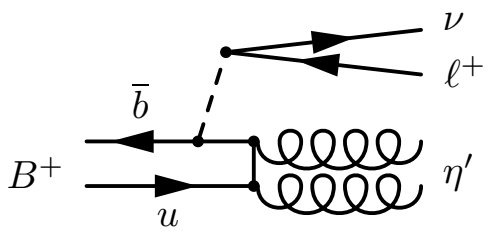

Figure 2.4: Feynman diagram for a flavor singlet contribution to $B^+ \to \eta' \ell^+ \nu$.

2.3.4 Form factors for $B^+ \to \eta^{(\prime)} \ell \nu$

Ball and Jones [29] have published calculations of $f_+^{\eta^{(\prime)}}$ using the method of light-cone sum rules; however, they cannot yet be used to reliably extract $|V_{ub}|$ from $\mathcal{B}(B \to \eta^{(\prime)} \ell \nu)$, as the relative strength of singlet contributions, as depicted in Figure 2.4, due to flavor $SU(3)$ octet-singlet mixing in the η-η' system, are not known. As reliable calculations of $f_+^{\eta^{(\prime)}}$ are developed, the branching fractions $\mathcal{B}(B^+ \to \eta^{(\prime)} \ell^+ \nu)$ will provide an additional means of determining $|V_{ub}|$ and/or test of form factor calculations.

More generally, some authors [28] suggest the measurement of the ratio $\mathcal{B}(B \to \eta' \ell \nu)/\mathcal{B}(B \to \eta \ell \nu)$ to constrain the size of singlet contributions to $B \to \eta^{(\prime)}$ form factors. A better understanding of these form factors can help explain η-η' dynamics and, e.g., unexpectedly large $B \to \eta' K$ branching fractions (vis-à-vis $\mathcal{B}(B \to \eta K)$) that have been observed.

Chapter 3

Experimental apparatus

Data described in this Dissertation were collected using the *BABAR* detector [30] during the period 22 October 1999 through 17 August 2006, divided temporally into five Runs. The *BABAR* detector records e^+e^- collisions created with the PEP-II B Factory located at the Stanford Linear Accelerator Center (SLAC) facility in Menlo Park, California; these are depicted schematically in Figure 3.1.

3.1 PEP-II

The PEP-II B Factory is an e^+e^- storage ring fed by a 3.2 km[1] linear particle accelerator using radio frequency cavity resonators. PEP-II consists of a high-energy ring, containing a beam of 9.0 GeV electrons (depicted in red in Figure 3.1) and a low-energy ring, a beam of 3.1 GeV positrons (shown in blue). Electrons and positrons collide in the interaction region at center-of-mass energy around 10.58 GeV.

This center-of-mass energy is chosen to correspond to the mass of the $\Upsilon(4S)$ resonance, which almost always[2] decays to a $B\overline{B}$ pair, but is not sufficienctly massive to generate additional hadrons in this decay. The asymmetry of the collisions enables the study of the time evolution of the $B\overline{B}$ system; the $\Upsilon(4S)$ system is generated with a Lorentz boost of $\beta\gamma = 0.56$ (with respect to the laboratory frame of reference); a B meson's decay time can be inferred from the position of the vertex of its daughter tracks.

[1] In this Chapter, quantities are as measured in the laboratory frame of reference, unless otherwise noted.

[2] The branching fraction $\mathcal{B}(\Upsilon(4S) \to B\overline{B})$ is greater than 96% (to 95% confidence) [9].

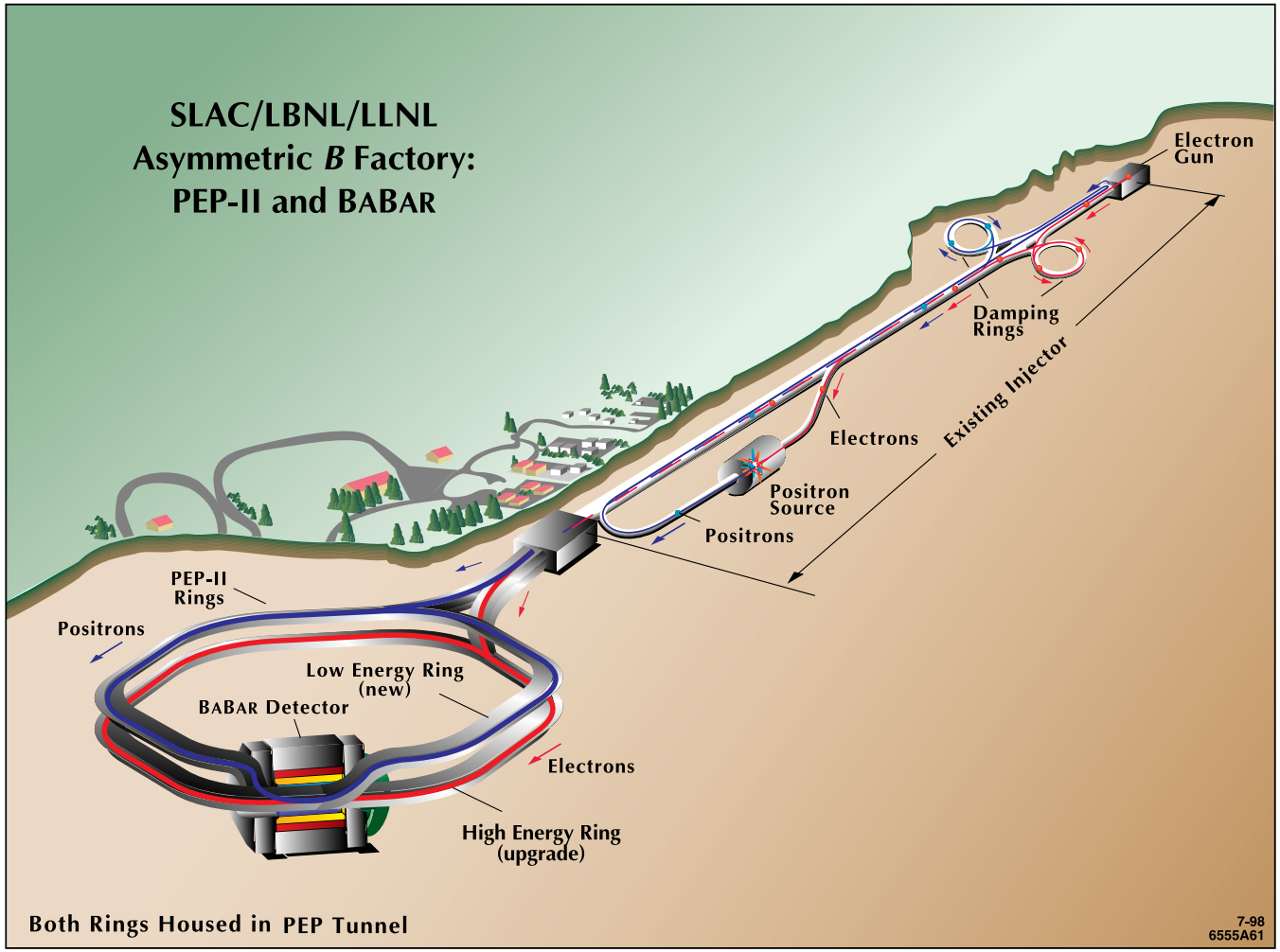

Figure 3.1: Layout of the region of the Stanford Linear Accelerator Center including the *BABAR* detector, the PEP-II B factory and the SLAC linear accelerator ("Existing Injector").

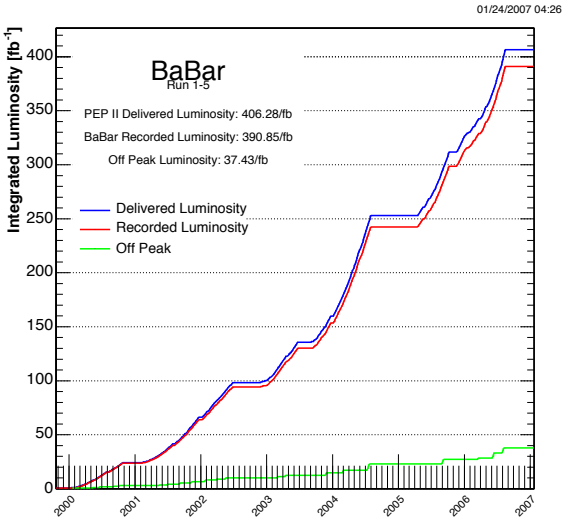

Figure 3.2: Integrated luminosity of e^+e^- collisions with center-of-mass energy at the $\Upsilon(4S)$ resonance as a function of time, delivered by PEP-II (top) and recorded by *BABAR* (middle). The bottom curve shows the integrated luminosity of recorded e^+e^- collisions off the $\Upsilon(4S)$ resonance.

At the $\Upsilon(4S)$ center-of-mass energy, the $b\overline{b}$ production cross section is $\sigma(e^+e^- \to b\overline{b}) = 1.05\,\text{nb}$. PEP-II was originally designed for a luminosity of $3 \times 10^{33}\,\text{cm}^{-2}\text{s}^{-1}$; since then, it has been back-engineered to achieve luminosities several times greater. At $9 \times 10^{33}\,\text{cm}^{-2}s^{-1}$, a more typical luminosity for the Run 5 period, $B\overline{B}$ pairs are created at a rate of roughly 10 Hz. The amounts of data delivered by PEP-II and recorded by *BABAR* are shown in Figure 3.2.

Additional "off-peak" e^+e^- collisions with a center-of-mass energy of 10.54 GeV are recorded as a means to study non-$B\overline{B}$ physics (e.g., $e^+e^- \to q\overline{q}$ (where $q \neq b$), $e^+e^- \to \tau^+\tau^-$), the amount of which is also depicted in the Figure 3.2.

3.2 The *BABAR* detector

The *BABAR* detector is a general purpose, cylindrical (roughly radially symmetric) particle detector with the interaction region along its axis; it is near hermetic, covering 91% of the solid angle in the center-of-mass frame.[3] Because PEP-II generates asymmetric e^+e^-

[3]The polar coverage (expressed in the dip angle) is $-50° < \lambda_{\text{lab}} < 70°$ in the laboratory frame of reference and $-65° < \lambda_{\text{CM}} < 65°$ in the center-of-mass frame of reference.

collisions, the *BABAR* detector is also front-back asymmetric.

Five roughly coaxial detector subsystems constitute the *BABAR* detector, in order of increasing distance from the interaction region: a silicon vertex tracker (SVT) and a drift chamber (DCH) for the reconstruction of charged tracks, a detector of internally reflected Čerenkov light (DIRC) for the identification of charged particles, an electromagnetic calorimeter (EMC) for the detection of photons and identification of electrons and an instrumented flux return (IFR) for the identification of muons and neutral hadrons (notably K_L^0 mesons); the first four operate in the 1.5 T magnetic field of a superconducting solenoid. The layout of these components is shown schematically in Figure 3.3.

3.2.1 Silicon vertex tracker

The SVT is the innermost *BABAR* detector subsystem, designed for the detection of charged particles and the precise measurement of their trajectories. It provides standalone tracking for low transverse momentum (50–120 MeV/c) particles, which cannot be reliably detected in the DCH.

It consists of double-sided silicon strip sensors arranged into five layers around the beampipe, as depicted in Figure 3.4; the layers consist of 6, 6, 6, 16 and 18 sensor modules. The modules in the inner three layers are straight; the modules in the outer two layers are somewhat arched to increase the crossing angle for tracks near the edges of the acceptance region.

Each module consists of several planar sensors, labeled by Roman numerals in Figure 3.4, for a total of 340 sensors in all; each sensor is a 300 μm thick double-sided silicon strip device, ranging in size, with the longitudinal dimension given first, between $43 \times 42\,\mathrm{mm}^2$ and $63 \times 53\,\mathrm{mm}^2$, for a total active silicon area of $0.96\,\mathrm{m}^2$. They are built on high-resistivity n-type substrates with p^+ strips running along one side and n^+ strips along the other, with (readout) pitch between 50 and 210 μm; about 40 V, more than the (silicon) depletion voltage, is applied across each. When a charged particle traverses the silicon, electron/hole pairs are created. These induced charges separate and accumulate at the strips and are read out electronically; p^+ and n^+ strips run orthogonally to each other, allowing a stereo spatial measurement of the trajectory.

Within its geometrical acceptance, the SVT is able to achieve a total tracking efficiency of

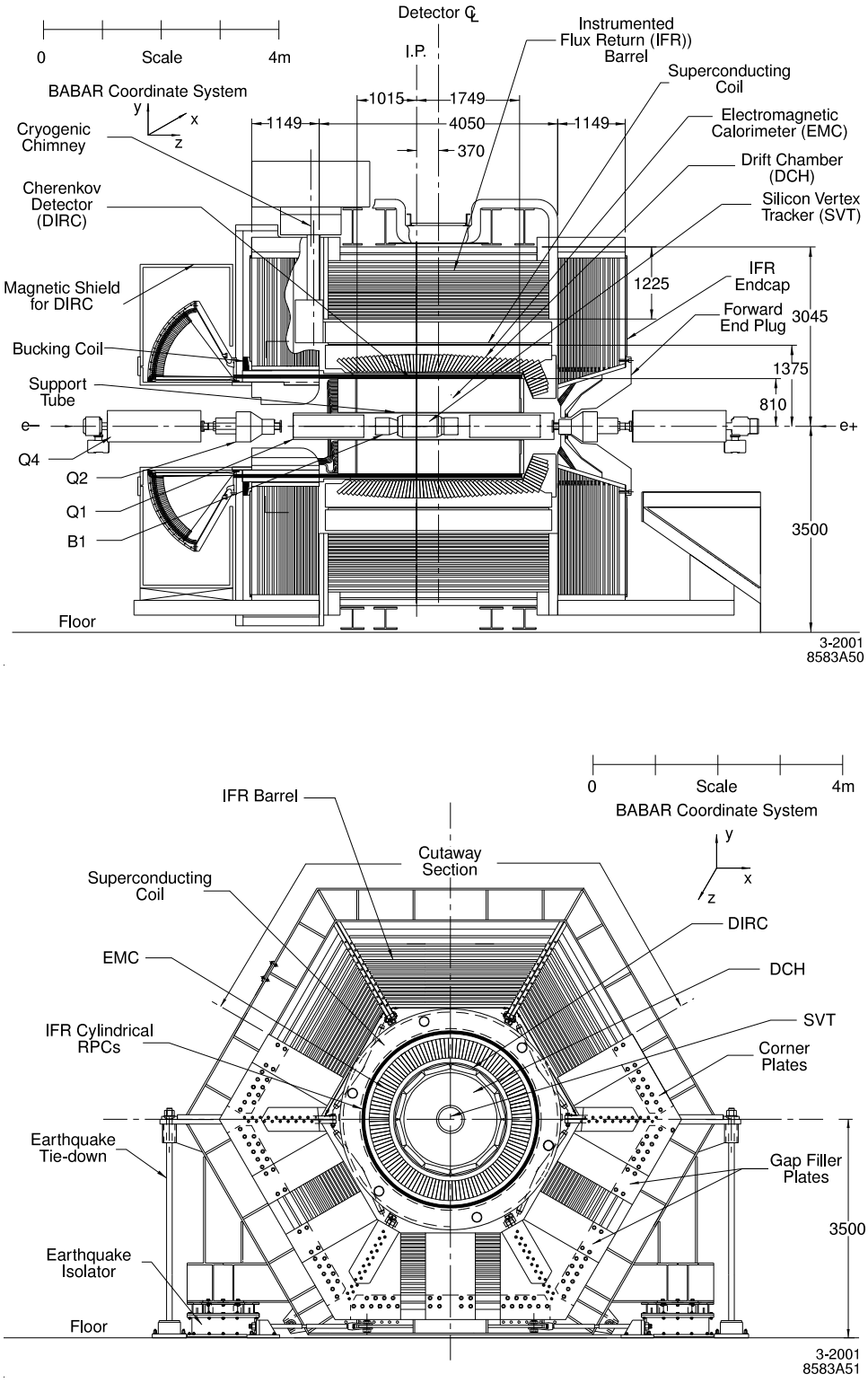

Figure 3.3: Layout of *BABAR* detector, longitudintal cross-section (top) and end view (bottom).

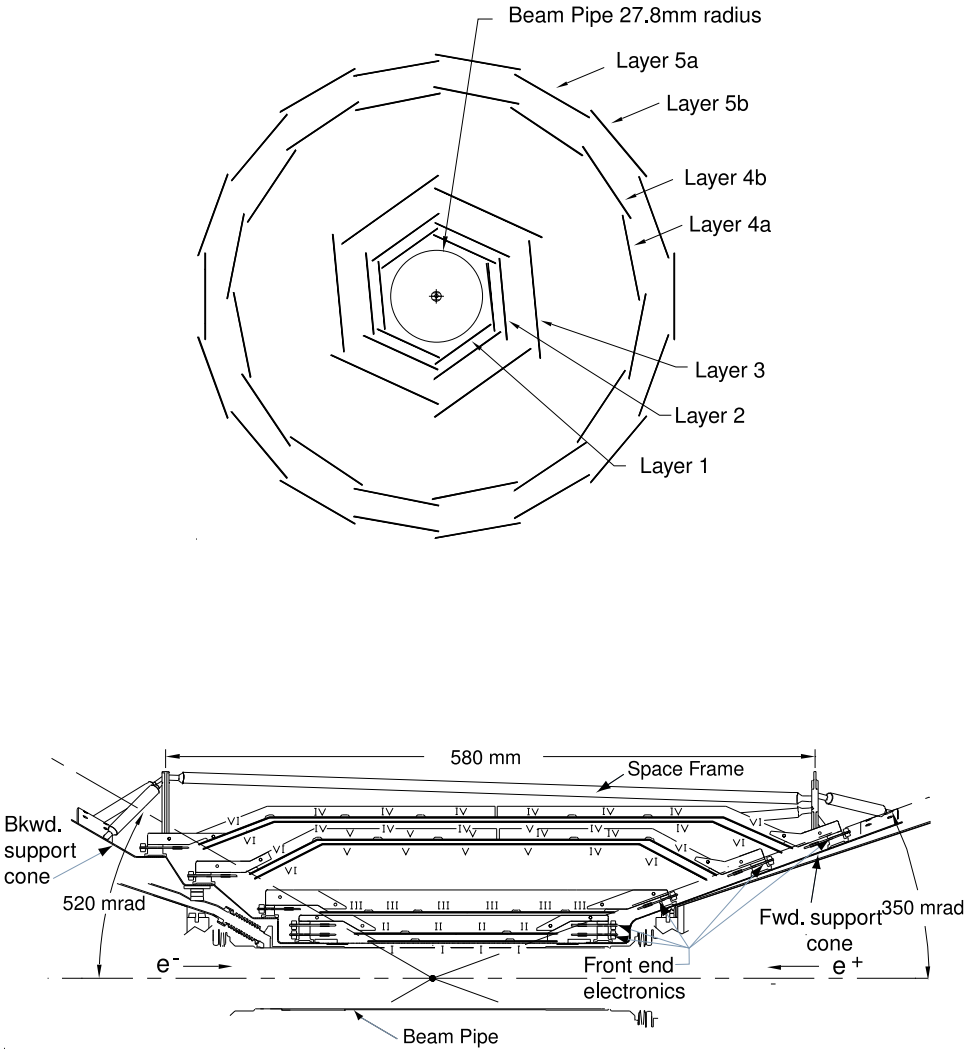

Figure 3.4: Arrangement of the SVT silicon strip sensor modules, transverse (top) and longitudinal (bottom) section. In the longitudinal section, the bottom half of the SVT is not shown.

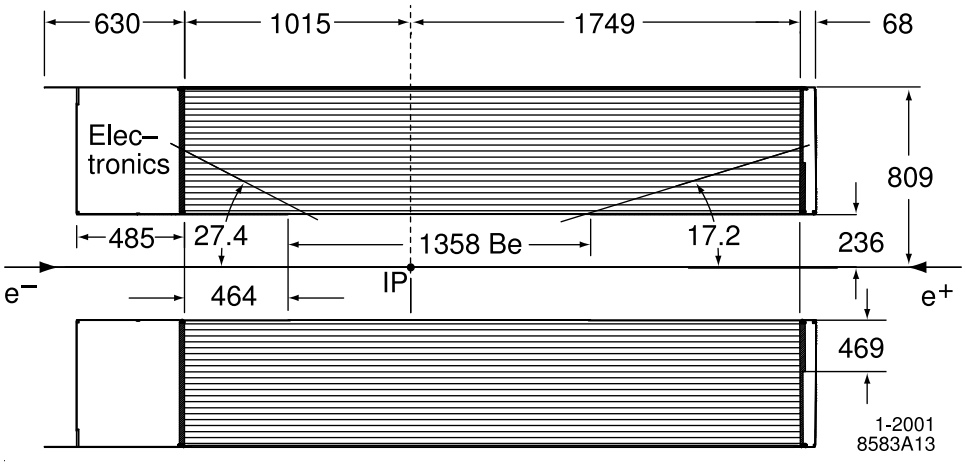

Figure 3.5: Layout of the DCH, longitudinal section. Dimensions are given in millimeters.

97%.[4] Spatial resolution, in each layer, can be as good as 10 μm in ϕ (azimuth) and 12 μm in z (longitude). Comparison of accumulated charge on the ten layer-sides provides energy loss[5] ($\mathrm{d}E/\mathrm{d}x$) measurements, which provide 2σ separation between kaons and pions with momenta up to 500 MeV/c, and between kaons and protons with momenta up to and beyond 1 GeV/c.

3.2.2 Drift chamber

The DCH, the primary tracking device of the *BABAR* detector, is a helium-based tracking chamber surrounding the SVT. Almost 3 m long along the beampipe, its transverse cross section is roughly an annulus with inner radius 236 mm and outer radius 809 mm, as depicted in Figure 3.5. The gas-filled volume is divided into 7104 drift cells running along the length of the DCH, arranged in a hexagonal lattice, which is logically subdivided into ten concentric superlayers of four layers each. Axial and (two types of) stereo superlayers alternate (with axial superlayers on either end); the stereo angle varies between 45 and 76 mrad.

Each drift cell is roughly 11.9 (radial) by 19.0 mm (azimuthal) in size and is centered around a 20 μm diameter gold-plated tungsten-rhenium sense wire, nominally kept at 1960 V, and is delineated by, typically, six gold-plated aluminium field-shaping wires, kept at ground, which are shared with adjacent cells. Series of guard wires run between the superlayers; two

[4]More information on the determination of detector (reconstruction) efficiencies, etc. can be found in §9.2.

[5]See Equation 3.2.2.

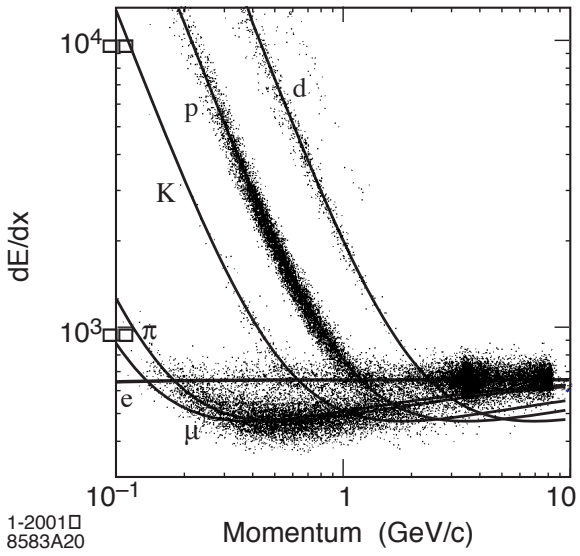

Figure 3.6: DCH measurements of $\mathrm{d}E/\mathrm{d}x$ versus track momenta. The lines represent Bethe-Bloch predictions for six particle species.

sets of clearing wires run along and collect charges generated by photon conversions in the chamber's inner (beryllium) and outer (composite) walls. The entire volume is filled with an 80 : 20 mixture of helium and isobutane (C_4H_{10}); the choice of gas and materials is intended to minimize multiple scattering within the device.

The tracking efficiency of the DCH by itself can approach 98% for tracks in the fiducial region with momentum greater than 200 MeV/c. It measures transverse momentum p_t via track curvature and has been measured to do so with resolution

$$\sigma_{p_\mathrm{t}}/p_\mathrm{t} = (0.13 \pm 0.01)\% \times p_\mathrm{t} + (0.45 \pm 0.03)\% \tag{3.1}$$

where p_t is given in GeV/c.

A charged particle passing through a DCH cell ionizes gas molecules (atoms); the resulting free electrons are accelerated toward a sense wire from which they are read out, in the process ionizing additional gas, creating additional free electrons and so forth. At typical operating parameters, the resulting avalanche gain is roughly 5×10^4. Additional spatial information is inferred from signal timing information; $\mathrm{d}E/\mathrm{d}x$ is inferred from the charge deposition in each cell.

The amount of energy lost ($\mathrm{d}E/\mathrm{d}x$) by a moderately relativistic charged particle traversing matter is given by the Bethe-Bloch equation [9]; because it depends on the velocity of a particle

rather than its momentum, $\mathrm{d}E/\mathrm{d}x$ can be combined with knowledge of a track's momentum (determined from its trajectory) to determine a particle's mass and thus its species. In Figure 3.6 are shown $\mathrm{d}E/\mathrm{d}x$ measurements taken in the DCH compared with Bethe-Bloch predictions for six particle species. The DCH alone provides $\mathrm{d}E/\mathrm{d}x$ measurements with a typical resolution of 7.5%, allowing, e.g., excellent pion/kaon separation up to around 700 MeV/c.

The two operationally independent tracking systems—the SVT and the DCH—allow a high tracking efficiency over a large momentum range. Both systems contribute to the identification of lower momentum charged particles. Information from both is also combined to infer the radial (d_0) and longitudinal (z_0) distance between a track's point of closest approach to the detector axis and the origin of the coordinate system (IP),[6] its azimuth ϕ_0 and its dip angle λ (relative to the transverse plane), which are determined with resolutions

$$\begin{aligned} \sigma_{d_0} &= 23\,\mu\mathrm{m}, \\ \sigma_{z_0} &= 29\,\mu\mathrm{m}, \\ \sigma_{\phi_0} &= 0.43\,\mathrm{mrad\ and} \\ \sigma_{\tan\lambda} &= 0.53 \times 10^{-3}. \end{aligned} \tag{3.2}$$

As a practical example, this results in a mass resolution of 11.4 MeV/c^2 when reconstructing J/ψ mesons from the $\mu^+\mu^-$ final state.

3.2.3 Detector of internally reflected Čerenkov light

The DIRC provides additional charged particle identification, separating pions and kaons with momenta up to 4.2 GeV/c via the phenomenon of Čerenkov radiation: when a charged particle traverses a medium faster than the speed of light in that medium, it emits radiation at the Čerenkov angle $\theta_{\check{\mathrm{C}}}$ to its trajectory:

$$\cos\theta_{\check{\mathrm{C}}} = \frac{1}{n\beta}, \tag{3.3}$$

with β the velocity of the particle (in units of c), which is measured and used to infer the particle's species.

The DIRC is laid out as a dodecagonal barrel and is depicted in Figure 3.7; the active

[6] This is the nominal interaction point.

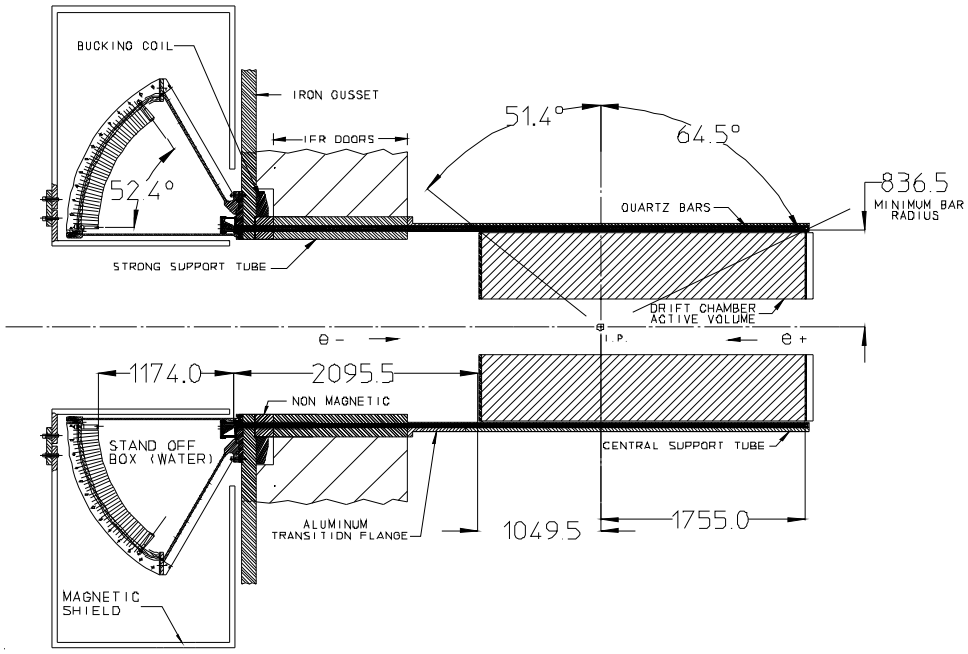

Figure 3.7: Layout of the DIRC, longitudinal section. Dimensions are given in millimeters.

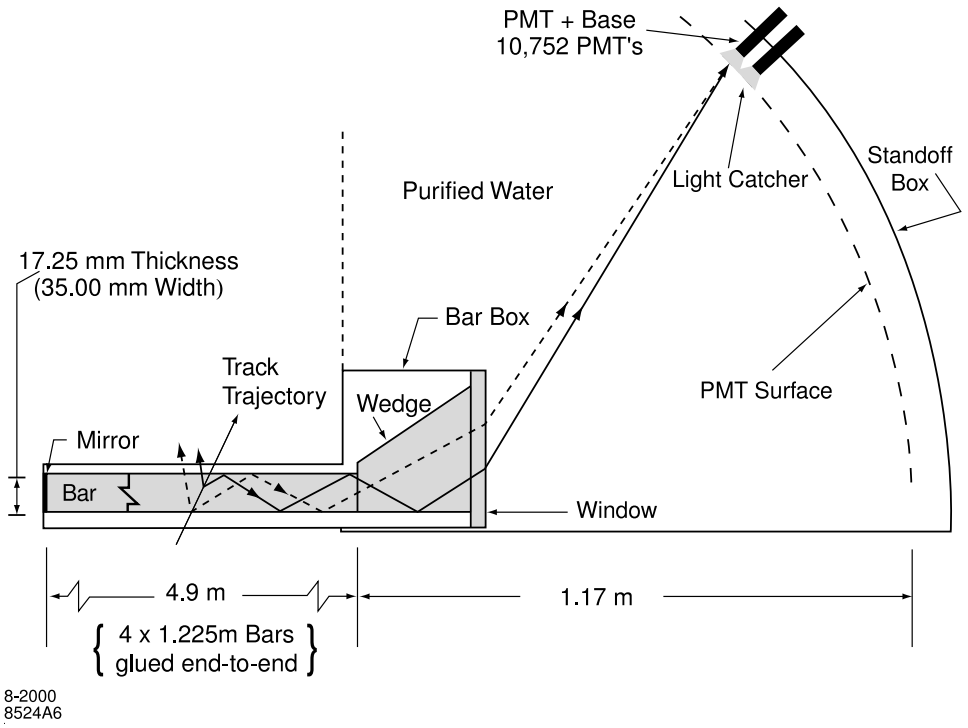

Figure 3.8: Schematic of DIRC silica bar and instrumentation.

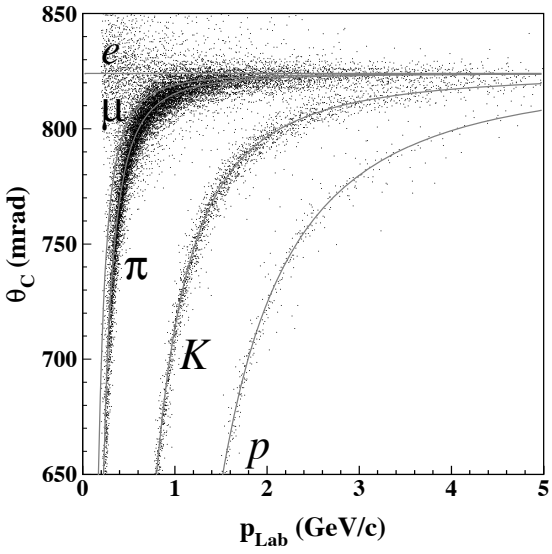

Figure 3.9: DIRC measurements of $\theta_{\check{\mathrm{C}}}$ versus track momenta. The lines represent predictions (See Equation 3.3.) for five particle species.

detection device for each side is a bar box containing twelve (optically isolated) 17 mm thick, 35 mm wide and 4.9 m long bars of fused silica ($n = 1.473$) running longitudinally. Čerenkov photons, effectively captured by total internal reflection preserving the Čerenkov angle, propagate in both directions along the bar; those that reach the forward end are reflected by mirror to the instrumented backward end—time differences between signals are used to infer the longitudinal location of their sources, which are matched to tracks reconstructed in the SVT and the DCH.

A schematic of the backward end instrumentation for a DIRC silica bar is shown in Figure 3.8. Photons emerge and expand into a medium of purified, deionized water ($n = 1.346$), totaling around 6000 L; at the silica/water boundary, there is a fused silica wedge reflecting photons with high exit angles (relative to the bar axis), decreasing the required amount of detection surface. The photons are collected by a dense array of photomultiplier tubes—10,752 in total, divided into twelve sectors—located 1.17 m from the ends of the silica bars.

The overall average resolution on $\theta_{\check{\mathrm{C}}}$ in the DIRC has been measured in dimuon events to be roughly 2.5 mrad, which translates, as is illustrated in Figure 3.9, into, e.g., 4.2σ separation between pions and kaons with momenta 3 GeV/c. DIRC measurements of $\theta_{\check{\mathrm{C}}}$ are also used to assist in the identification of muons with momenta below roughly 750 MeV/c.

3.2.4 Electromagnetic calorimeter

The EMC measures electromagnetic showers thereby detecting photons and identifying SVT and DCH tracks as electrons. The detection medium is 6580 crystals: a barrel containing 48 rings, each of 120 crystals running around the detector azimuth, and a forward endcap of eight rings, each with bewteen 80 and 120 crystals, as depicted in Figure 3.10.

The crystals are made of thallium-doped (0.1%) cæsium iodide salt, machined and polished into rectangular frusta with length between 29.6 and 32.4 cm and, typically, front face $4.7 \times 4.7\,\mathrm{cm}^2$ and back face $6.1 \times 6.0\,\mathrm{cm}^2$; one is depicted in Figure 3.11. Incident photons and electrons induce photon conversion ($\gamma \to e^+e^-$) and electron bremsstrahlung radiation ($e^\pm \to e^\pm\gamma$) which cascade, creating a shower of low energy particles which are absorbed by the crystal, which acts as a total-absorption scintillating medium. Energy deposition is read out by silicon photodiodes placed at the back end of the crystal.

The energy resolution of the EMC has been found to be

$$\frac{\sigma_E}{E} = \frac{(2.32 \pm 0.30)\%}{\sqrt[4]{E}} \oplus (1.85 \pm 0.12)\%, \tag{3.4}$$

where E is the incident energy in units of GeV. As a practical matter, this results in a $6.9\,\mathrm{MeV}/c^2$ mass resolution when reconstructing $\pi^0 \to \gamma\gamma$. Additionally, the ratio of a track's EMC shower energy to its momentum (E/p) can be used to distinguish electrons from hadronic particles. For example, from tracks with momenta between 0.5 and $2\,\mathrm{GeV}/c$, electrons can be identified with 94.8% efficiency with 0.3% misidentification of pions.

3.2.5 Instrumented flux return

The flux return of the solenoid magnet has been instrumented for the identification of muons and the detection of neutral hadrons that may not interact with other detector components. The IFR consists of a hexagonal barrel around the EMC and (flat) forward and backward endcap doors.

The IFR was originally outfitted with resistive plate chambers (RPCs); 19 (18) layers of planar RPCs were interleaved between sheets of iron, which increase in thickness outward from 2 to 10 cm, in the barrel walls (endcaps). Two additional layers of cylindrical RPCs surround the EMC,[7] for a total active detector area of about $2000\,\mathrm{m}^2$. At the core of each RPC are two

[7]Each layer of a barrel wall (an endcap) is segmented into three (twelve) RPCs; there are

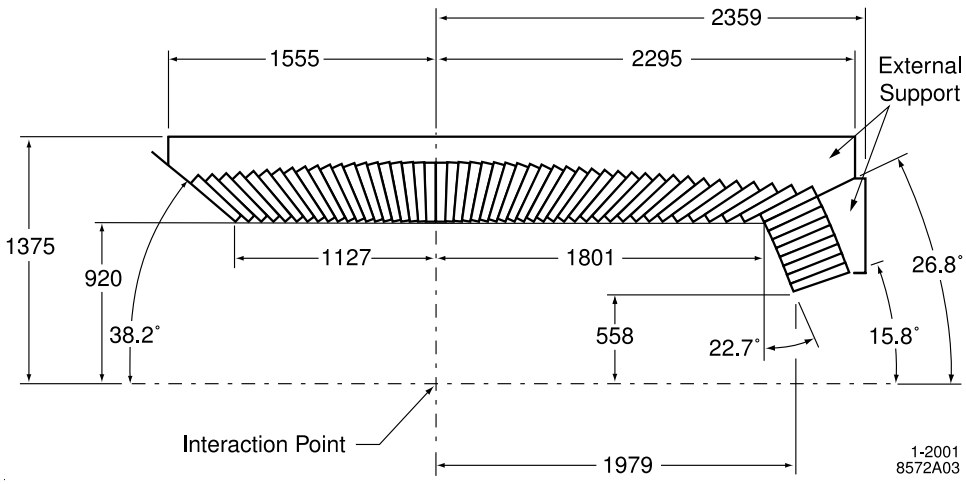

Figure 3.10: Layout of the crystals of the EMC, longitudinal section. Dimensions are given in millimeters. The bottom half of the EMC is not shown.

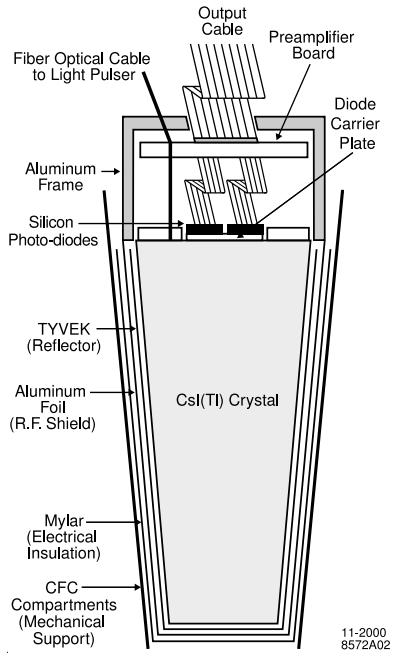

Figure 3.11: Schematic of EMC crystal and instrumentation. (This drawing is not to scale.)

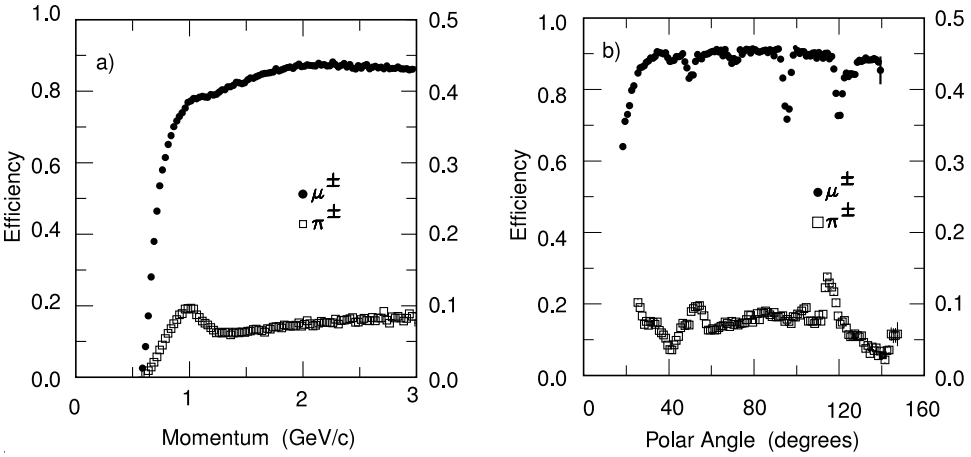

Figure 3.12: IFR muon identification efficiency (left scale) and pion misidentification (as muon) probability (right scale) as a function of track momentum (left) and angle from the beam axis (right), using loose selection criteria.

2 mm sheets of Bakelite coated (on the outside) with graphite, held 2 mm apart by spacers. The space between the sheets is filled with a mixture of 56.7% argon, 38.8% freon and 4.5% isobutane; the graphite surfaces are held at 8 kV. As in the DCH, a high energy particle entering the gas volume induces an avalanche; here the avalanche grows into a controlled electric discharge which is read out capacitively via aluminum strips on a Mylar substrate, running orthogonally on either side of the RPC.

In this configuration, information from the IFR and EMC are combined to identify SVT and DCH tracks as muons; with loose (tight) selection criteria, tracks with momentum between 1.5 and 3 GeV/c can be identified as muons with efficiency close to 90% (about 80%) and 6% (3%) pion misidentification (including in-flight $\pi \to \mu\nu$ decay), as shown in Figure 3.12. IFR clusters not associated with charged tracks can be identified as K_L^0 mesons and are reconstructed with an angular resolution of roughly 60 mrad[8] and no energy information. Overall K_L^0 detection efficiency grows linearly between 20% and 40% over the 1 to 4 GeV/c momentum range.

For Run 5 (beginning spring 2005), RPCs in the top and bottom sextants of the IFR were removed and replaced with twelve layers of limited streamer tubes (LSTs) and six layers of thirty-two "cylindrical" RPCs in total: 8 (azimuth) ×2 (longitude) ×2 (radial).

[8]This resolution is improved by a factor of two if the K_L^0 meson also interacts in the EMC.

brass.[9] Each LST is a PVC structure housing eight side-by-side $15 \times 17\,\mathrm{mm}^2$ cells running roughly 3.5 m longitudinally. Each cell has a $100\,\mu$m gold-plated beryllium copper wire running down its center, and is filled with a 3.5% argon, 8% isobutane and 88.5% carbon dioxide gas mixture. The wires are held at 5.5 kV and the cells are coated in graphite, which is grounded. The operational principle is analogous to that of the RPCs: streamers induced by high energy particles passing through the gas are read out on the wires and on orthogonal readout strips.

3.3 The *BABAR* trigger

The task of data acquisition presents a challenge in high luminosity experiments: at the design luminosity of PEP-II, background rates[10] are typically around 20 kHz, compared to the (design) $b\bar{b}$ production rate of 3.2 Hz. To this end, *BABAR* has developed a trigger system to reject backgrounds with sufficient efficiency that the remaining events—under 120 Hz—can be written to disk. The trigger is implemented as a two-tiered system: a Level 1 (L1), which is hardware-based, and Level 3 (L3), based in software.

The L1 trigger is implemented via dedicated hardware boards housed in several VME crates and consists of three subtriggers, each issuing multiple acceptance decisions based on DCH, EMC and IFR information respectively:

- The DCH trigger (DCT) identifies tracks using only cell occupancy (and timing) information. The track segment finder (TSF) looks for cell hit patterns in each DCH superlayer which, via look-up table, are translated into track segments, which are passed to
  - the binary link tracker (BLT), which determines that a track (with some minimum transverse momentum around 120 MeV/c or greater) has been found when there are track segments in eight of the ten DCH superlayers, and the segments in adjacent superlayers are sufficiently azimuthally close, and the

[9] RPCs in the innermost (non-cylindrical) layer are physically inaccessible for removal, but were deactivated.

[10] Background rates are defined via events with at least one track found in the DCH with transverse momentum greater than 120 MeV/c or at least one cluster found in the EMC with energy greater than 100 MeV.

  - p_{t} discriminator (PTD) which determines, by extrapolating from high-quality track segments in the four axial DCH superlayers, whether a collection of segments is consistent with containing a track with transverse momentum greater than some configurable threshold value (usually around 800 MeV/c).

- The EMC trigger (EMT) logically divides the EMC into 280 towers, each of between 19 and 24 crystals. Measured energy summed over various combinations of adjacent towers is compared with threshold values, ranging from 100 to 1000 MeV.

- The IFR trigger infers the presence of a muon from the presence of coincident hits in at least four of eight selected IFR layers, for triggering on $e^+e^- \to \mu^+\mu^-$ events and cosmic rays. This is used primarily for diagnostic purposes.

Trigger primitives are fed to a global trigger for time-alignment and some additional processing, e.g., matching BLT tracks with EMT clusters or finding back-to-back objects. This information is combined into specific triggers, e.g., a two-track trigger, events passing the logical or of which are passed through to the L3 trigger. The L1 trigger is issued in a fixed latency window (11–12 μs after e^+e^- collision) and is measured to achieve a timing resolution of 52 ns for hadronic events. Its parameters are tuned for a typical acceptance rate of 1 kHz.

The software-based L3 runs on a computing farm and refines and augments L1 trigger decisions. Track segments from the TSF are combined with full DCH information to reconstruct tracks with estimates of trajectory as well as distance from the IP; the L3 DCH trigger selects events with at least one "tight" ($p_{\mathrm{t}} > 600$ MeV/c) or two "loose" ($p_{\mathrm{t}} > 250$ MeV/c) tracks coming from the IP. The orthogonal L3 EMC trigger filters out background noise and forms neutral clusters with energy greater than 100 MeV, calculating energy moments and time averages; events with "event mass"[11] greater than 1.5 GeV and either at least two clusters with high (event center-of-mass frame) energy E_{CM} (> 350 MeV) or at least four clusters are selected. Specific physics filters are implemented, e.g., Bhabha scattering, cosmic rays and $e^+e^- \to \gamma\gamma$ events can be selected, prescaled or rejected. The L3 runtime takes an average of 8.5 ms per event (per computer), accepting physics (calibration, diagnostic) events at a rate of roughly 73 (49) Hz.

[11] The event mass is defined as the invariant mass of all neutral clusters, assuming each cluster represents a massless particle.

The overall trigger efficiency is quite high; it is found to exceed 99.9% for $B\overline{B}$ events. It is better than 95% for $e^+e^- \to q\overline{q}$ ($q \neq b$) events and better than 90% for other physics events of design interest, e.g., $e^+e^- \to \tau^+\tau^-$.

Since the beginning of data taking at *BABAR*, the luminosity of PEP-II has surpassed its design luminosity by a factor of several; to ensure stable data acquisition, the DCT was upgraded to further reject beam-induced backgrounds at L1: PTD modules were replaced with z_0-p_t discriminators (ZPD) which improve upon PTD performance by rejecting tracks estimated not to come from the IP. With input from the TSFs with improved track segment azimuth information,[12] "seed" track segments in the two outermost axial DCH superlayers are matched with compatible track segments in other superlayers to construct tracks with curvature, dip angle, azimuthal and DCH hit information. A fitting algorithm, based largely on look-up tables due to performance requirements, refines the curvature and dip angle estimates and determines z_0, the longitudinal position of a track's point of closest approach to the beamline; the ZPD can accept tracks based on curvature, z_0, the uncertainty on the z_0 estimate or the map of associated track segments. These functions are implemented via field-programmable gate arrays; there are eight ZPD boards, each responsible for 45° azimuthal coverage of seed segments.

The development, manufacture, installation, commissioning and maintenance of the ZPDs is due largely to the efforts of Harvard University *BABAR* collaborators and the staff at Harvard University Laboratory for Particle Physics and Cosmology (née Harvard University High Energy Physics Laboratory). The upgrade was completed in summer 2004; the upgraded DCT, known as "DCZ," has since performed robustly to its design goals.

[12]The TSFs were also upgraded, to provide this information.

Chapter 4

Analysis method

The analysis described in this Dissertation reconstructs exclusive semileptonic decays $B \to X\ell\nu$ ("signal side"), where X is one of the pseudoscalar charmless mesons $\pi^{\pm}$, π^0, η or η', in the recoil of semileptonic decays $B \to D^{(*)}\ell\nu$ ("tag side"); $D^{(*)}$ mesons are fully hadronically reconstructed. Events which, outside this $D\ell$-$X\ell$, contain neither additional tracks nor a significant amount of neutral energy are considered. For the purposes of extracting $|V_{ub}|$, partial branching fractions for $B^0 \to \pi^-\ell^+\nu$, $B^+ \to \pi^0\ell^+\nu$ and $B^+ \to \eta\ell^+\nu$ are measured separately in three bins of q^2: < 8, 8–16 and ≥ 16 GeV$^2/c^2$. Due to the lower efficiency in reconstructing the η' meson, the $B^+ \to \eta'\ell^+\nu$ branching fraction is measured only in a $q^2 < 16$ GeV$^2/c^2$ bin and over the full q^2 range.

Due to the presence of two neutrinos, three quantities are used to determine the compatibility of an event's kinematics with the hypothesized final state. The quantity $\cos(BY)$ is defined to be the angle[1] between the momenta of a Y system and its parent B in a decay $B \to Y\nu$; as the neutrino is massless,

$$\cos(BY) = \frac{2E_B^* E_Y^* - m_B^2 - m_Y^2}{2p_B^* p_Y^*} \tag{4.1}$$

where E_B^*, m_B and p_B^* (E_Y^*, m_Y and p_Y^*) are the energy, mass and absolute momentum of the B meson (Y system) respectively.[2] If the Y system is compatible with the $B \to Y\nu$ hypothesis, BY is a physical angle and, thus, up to resolution, $|\cos(BY)| \leq 1$. This quantity is considered for both B mesons: $\cos(BY_D)$ (where $Y_D \equiv D^{(*)}\ell$) and $\cos(BY_X)$ (where $Y_X \equiv X\ell$).

[1] In this Chapter, quantities are as measured in the center-of-mass frame of reference.

[2] These, for the B meson, are known from the beam energy.

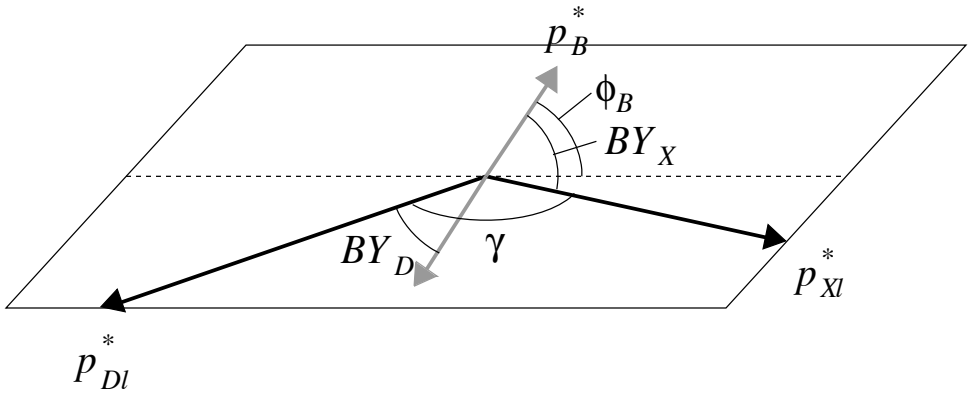

Figure 4.1: A schematic diagram of hypothesized event kinematics. The plane depicted contains $\vec{p}_{D\ell}$ and $\vec{p}_{X\ell}$. One of the two possible sets of B directions is shown (The other is obtained by reflection in the $D\ell$-$X\ell$ plane.); the angle ϕ_B is between the direction of either B meson and the $D\ell$-$X\ell$ plane.

With this $\cos(BY)$ constraint, for each side of the event, possible B momenta are described by a cone with slant height p^*_B and axis $\vec{p}^*_Y$, the momentum vector of the Y system. The requirement that tag and signal B mesons emerge back-to-back further constrains event kinematics, determining the direction of either B meson up to two-fold ambiguity.[3] The angle between the $D\ell$-$X\ell$ plane and either $\vec{p}^*_B$ possibility is denoted ϕ_B;

$$\cos^2\phi_B = \frac{\cos^2(BY_D) + 2\cos(BY_D)\cos(BY_X)\cos\gamma + \cos^2(BY_X)}{1-\cos^2\gamma} \tag{4.2}$$

where γ is the angle between the $D\ell$ and $X\ell$ momenta. A schematic of event kinematics describing the relationship between the angles BY_X, BY_D, γ and ϕ_B is presented in Figure 4.1. Events consistent with the $D\ell$-$X\ell$ decay hypotheses thus have, up to resolution, $\cos^2\phi_B \leq 1$.

Events containing viable $D\ell$-$X\ell$ decay candidates are selected from the full *BABAR* data set as described in §6; the quantity $\cos^2\phi_B$ is used as the discriminating variable to extract signal yield, as described in §8.

[3]Two nondegenerate circles on the surface of a sphere (in this case of radius p^*_B) have at most two points of intersection.

4.1 Derivation of $\cos(BY)$

Where a B meson decays $B \to Y\nu$, and m_i, P_i, E_i and $\vec{p}_i^*$ are the appropriate invariant mass, four-momentum, energy and three-momentum, the massless neutrino constraint gives

$$\begin{aligned} 0 = P_\nu^2 &= (P_B - P_Y)^2 \\ &= P_B^2 + P_Y^2 - 2P_B \cdot P_Y \\ &= m_B^2 + m_Y^2 - 2(E_B E_Y - \vec{p}_B^* \cdot \vec{p}_Y^*), \end{aligned} \tag{4.3}$$

and thus

$$2\vec{p_B} \cdot \vec{p_Y} = 2E_B E_Y - m_B^2 - m_Y^2, \tag{4.4}$$

$$\cos(BY) = \frac{2E_B E_Y - m_B^2 - m_Y^2}{2|\vec{p}_B^*||\vec{p}_Y^*|}, \tag{4.5}$$

where $\cos(BY)$ is the angle between $\vec{p}_B^*$ and $\vec{p}_Y^*$, i.e., Equation 4.1.

4.2 Derivation of $\cos^2\phi_B$

For full event kinematics, as depicted in Figure 4.1, the vectors $\vec{p}_{D\ell}^*$ and $\vec{p}_{X\ell}^*$ are defined as the momenta of all measured (i.e., non-neutrino) tag-side and signal-side particles respectively. The momentum vector $\vec{p}_B^*$ is chosen to correspond to the signal-side (i.e., decaying to $X\ell$) B meson; $\hat{p}_{D\ell}^*$, $\hat{p}_{X\ell}^*$ and $\hat{p}_B^*$ are corresponding unit vectors. The unit vector $\hat{n}$ given by

$$\hat{n} \equiv \frac{\hat{p}_{D\ell}^* \times \hat{p}_{X\ell}^*}{\sin\gamma}, \tag{4.6}$$

where γ is the angle between $\vec{p}_{D\ell}^*$ and $\vec{p}_{X\ell}$, is perpendicular to the $D\ell$-$X\ell$ plane. As $\hat{p}_B^* \times \hat{n}$ gives the sine of the complement of ϕ_B,

$$\begin{aligned} |\cos\phi_B| &= \left| \hat{p}_B^* \times \frac{\hat{p}_{D\ell}^* \times \hat{p}_{X\ell}^*}{\sin\gamma} \right| \\ &= \left| \frac{\hat{p}_{D\ell}^*(\hat{p}_B^* \cdot \hat{p}_{X\ell}^*) - \hat{p}_{X\ell}^*(\hat{p}_B^* \cdot \hat{p}_{D\ell}^*)}{\sin\gamma} \right| \\ &= \left| \frac{\hat{p}_{D\ell}^* \cos(BY_X) + \hat{p}_{X\ell}^* \cos(BY_D)}{\sin\gamma} \right|, \end{aligned} \tag{4.7}$$

since $\hat{p}^*_B \cdot \hat{p}^*_{X\ell} = \cos(BY_X)$ and $\hat{p}^*_B \cdot \hat{p}^*_{D\ell} = -\cos(BY_D)$. Because $\hat{p}^*_{D\ell} \cdot \hat{p}^*_{X\ell} = \cos\gamma$,

$$\begin{aligned}\cos^2\phi_B &= \frac{\cos^2(BY_X) + 2(\hat{p}^*_{D\ell} \cdot \hat{p}^*_{X\ell})\cos(BY_X)\cos(BY_D) + \cos^2(BY_D)}{\sin^2\gamma} \\ &= \frac{\cos^2(BY_X) + 2\cos(BY_X)\cos(BY_D)\cos\gamma + \cos^2(BY_D)}{\sin^2\gamma},\end{aligned} \tag{4.8}$$

i.e., Equation 4.2.

Chapter 5

Data set

The measurements described in this Dissertation are made using 383.2 million $B\overline{B}$ pairs[1] and 36.6 fb^{-1} of off-peak data recorded with the *BABAR* detector. Off-peak data events are weighted to match the luminosity and pair-production cross section of the on-peak data.

5.1 Event reconstruction

In the translation of detector response into information about an underlying physics event, criteria for assigning particle hypotheses vary for, e.g., desired acceptance rate (versus purity). Thus, in reconstructing an event, there are various criteria by which a given reconstruction hypothesis can be defined. Those used for the measurements described in this Dissertation are defined here.

5.1.1 Charged tracks

The raw list of tracks reconstructed in the SVT and/or DCH is `ChargedTracks`. The more refined `GoodTracksVeryLoose` is the subset of such tracks with momentum[2] less than 10 GeV/c; additonally, the point of closest approach of the extrapolated track to the beamline is required to be no further than 10 cm from the IP in the longitudinal direction and 1.5 cm in the transverse plane.

[1] See §9.5.

[2] In this Chapter, unless otherwise noted, quantities are as measured in the laboratory frame of reference.

5.1.2 Neutral clusters

All single-bump neutral clusters found in the EMC that are not matched with any track are contained in the `CalorNeutral` list. The more refined `GammaForPi0` adds more stringent photon requirements on clusters—at least 30 MeV of raw energy and lateral moment less than 0.8—for use in reconstructing $\pi^0 \to \gamma\gamma$ decays. The `GoodPhotonDefault` list, more stringent still, imposes the additional requirement that neutral clusters have more than 100 MeV of energy, and is useful when reconstructing photons in contexts that would otherwise be subject to high detector backgrounds.

Additionally, the `CalorClusterNeutral` list, a superset of `CalorNeutral`, contains all (not necessarily single-bump) neutral clusters found in the EMC not matched with any track, and is used in reconstructing "merged" π^0 candidates, i.e., π^0 mesons detected without distinct γ daughters.

5.1.3 Particle identification

The primary electron list used is `PidLHElectrons` which employs a likelihood-based selector on tracks taken from `ChargedTracks`. Initial requirements are imposed to reject muons:

- a track must be associated with a neutral cluster with energy deposited in at least four EMC crystals,
- $0.5 < E_{\mathrm{EMC}}/p < 1.5$, where E_{EMC} is the energy deposited in the EMC and p the absolute momentum of the track,[3] and
- $\mathrm{d}E/\mathrm{d}x$, as measured in the DCH, must lie within some fixed range.[4]

A track's E_{EMC}/p, (associated) neutral cluster lateral moment, neutral cluster position (relative to the track), Čerenkov angle (when sufficient Čerenkov photons have been detected in the DIRC) and $\mathrm{d}E/\mathrm{d}x$ (and corresponding resolution, a function of its momentum, dip angle and number of associated DCH hits) are used to compute likelihoods (L_i) for electron, pion,

[3]The upper limit on E_{EMC}/p is intended to reject antiprotons, which can annihilate in the EMC.

[4]See Figure 3.6; the Bethe-Bloch prediction for electron $\mathrm{d}E/\mathrm{d}x$ is essentially flat.

kaon and proton hypotheses.[5] Electrons are selected via the fractional electron likelihood

$$\frac{a_e L_e}{a_e L_e + a_\pi L_\pi + a_K L_K + a_p L_p} > 95\%, \tag{5.1}$$

where a_i are expected relative abundances. The `ElectronsLoose` list provides looser electron identification and is used in the reconstruction of $J/\psi \to e^+e^-$ decays: the same $\mathrm{d}E/\mathrm{d}x$ requirement is imposed; to be identified as an electron, a track must also be matched with a neutral cluster with energy deposited in at least three EMC crystals and $0.65 < E_{\mathrm{EMC}}/p < 5$.

The primary muon list used is `MuonNNTight`; a track's trajectory and corresponding IFR and EMC information[6] are fed into an artificial neural network which has been trained for muon-pion discrimination using muons from $e^+e^- \to \mu^+\mu^-\gamma$ and $e^+e^- \to e^+e^-\mu^+\mu^-$ events and pions from $e^+e^- \to \tau^+\tau^-$ events, where one τ decays leptonically (e.g., $\tau^- \to e^-\overline{\nu}_e\nu_\tau$) and the other to pions (e.g., $\tau^+ \to \pi^+\pi^-\pi^+\overline{\nu}_\tau$). The `MuonNNTight` configuration of the neural network is designed to be 70% efficient for muons and misidentifies pions at a rate on the order of a few percent. A more inclusive muon list, `MinimumIonizing`, used in the reconstruction of $J/\psi \to \mu^+\mu^-$ decays, selects muons using EMC information ($E_{\mathrm{EMC}}/p < 0.5$) only.

Charged kaons are taken from `KLHNotPion`; tracks are selected with a likelihood method analogous to that of `PidLHElectrons`, in this case with Čerenkov angle information from the DIRC and $\mathrm{d}E/\mathrm{d}x$ information from the SVT and DCH. Tracks with a greater than 20% likelihood of being a kaon (or proton) rather than a pion are selected.

5.1.4 Composite particles

The primary list used in reconstructing π^0 candidates is `pi0DefaultMass`, which contains pairs of photons taken from `GammaForPi0` with invariant mass between 115 and 150 MeV/c^2 and energy greater than 200 MeV. The `pi0AllVeryLoose` list is more inclusive, taking photon pairs in an invariant mass window of 90 to 165 MeV/c^2 (with no energy requirement); it also contains merged π^0 candidates: neutral clusters from the `CalorClusterNeutral` list with cluster shape consistent with originating from a π^0 meson.

[5] The forms of these likelihood functions are derived from control samples for each particle type, and are binned in tracks' absolute momentum and dip angle.

[6] Additionally, global time information is used to account for the evolution of the performance of the *BABAR* detector.

"Soft" (i.e., low momentum) π^0 candidates are taken from a separate `pi0SoftDefaultMass` list, effectively the same[7] as `pi0DefaultMass`, but with a 450 MeV/c upper limit on the absolute candidate momentum in the event center-of-mass frame of reference.

Candidate K^0_S mesons are written to the `KsDefault` list, which contains pairs of pion candidates (from `ChargedTracks`) of opposite charge with raw invariant mass between 472.67 and 522.67 MeV/c^2. A refined estimate of the invariant mass is made, with both track trajectories recalculated with the assumption that they passed through the pair's point of closest approach, and required to be between 440 and 550 MeV/c^2.

5.2 Simulated data

A set, several times as abundant as the recorded data, of Monte Carlo simulated data is also used, in which physics processes and particle decays are modeled using the `EvtGen` package [31] and detector response via a *BABAR* simulation based on the `GEANT4` toolkit [32].

Generic $B^0\overline{B}^0$ and B^+B^- events are generated separately, as are signal modes $B \to \pi^\pm \ell\nu$, $B \to \pi^0 \ell\nu$, $B \to \eta \ell\nu$ and $B \to \eta' \ell\nu$; for each signal mode, the others are considered as potential background sources. Events with other charmless semileptonic B decays—$B \to \rho^0 \ell\nu$, $B \to \rho^\pm \ell\nu$, $B \to \omega \ell\nu$ and nonresonant[8] $b \to u \ell\nu$ decays—are considered potential background sources and modeled separately as well. In the charmless semileptonic decay samples, one B meson decays as described; the decay of the other B is generic. Events with charmless semileptonic decays are removed from the generic $B\overline{B}$ simulated samples.

The sizes of all data sets are given in Table 5.1.

5.2.1 Physics simulation

Simulated data events are weighted to match, run-by-run, measured $B\overline{B}$ production.[9] Similarly, off-peak data is scaled to match the pair-production rate in data taken at the $\Upsilon(4S)$ resonance.

[7] Technically, this list uses photons from a separate `GoodPhotonLoose` list, which is functionally equivalent to `GammaForPi0`.

[8] Here, "nonresonant" refers to all other charmless $B \to X \ell\nu$ decays.

[9] For the purposes of data simulation, B^+B^- and $B^0\overline{B}^0$ pairs are assumed to be produced in equal abundance.

Table 5.1: Size of data, simulated data samples used.

	Run 1	Run 2	Run 3	Run 4	Run 5
data					
on-peak (10^6 $N_{B\overline{B}}$)	22.43	67.47	35.61	110.48	147.17
on-peak (fb^{-1})	20.43	61.15	32.31	100.75	133.76
off-peak (fb^{-1})	2.62	6.92	2.47	10.12	14.50
simulated data (10^6 $N_{B\overline{B}}$)					
$B \to \pi^{\pm}\ell\nu$	0.105	0.314	0.165	0.506	0.662
$B \to \pi^{0}\ell\nu$	0.105	0.314	0.165	0.506	0.664
$B \to \eta\ell\nu$	0.105	0.314	0.165	0.506	0.664
$B \to \eta'\ell\nu$	0.105	0.314	0.165	0.506	0.664
$B \to \rho^{0}\ell\nu$	0.105	0.314	0.165	0.506	0.664
$B \to \rho^{\pm}\ell\nu$	0.105	0.314	0.165	0.506	0.664
$B \to \omega\ell\nu$	0.105	0.314	0.165	0.506	0.664
nonresonant $b \to u\ell\nu$	0.844	2.514	1.322	4.047	5.326
generic $B^0\overline{B}^0$	69.318	103.640	50.556	167.565	214.466
generic B^+B^-	70.430	103.124	47.102	167.524	224.530

Table 5.2: Assumed $b \to u\ell\nu$ branching fractions [16, 33, 34].

$B^0 \to$	$\mathcal{B}$ (10^{-4})	$B^{\pm} \to$	$\mathcal{B}$ (10^{-4})
$\pi\ell\nu$	1.39 ± 0.09	$\pi^0\ell\nu$	0.75 ± 0.05
		$\eta\ell\nu$	0.84 ± 0.34
		$\eta'\ell\nu$	0.84 ± 0.84
$\rho^{\pm}\ell\nu$	2.38 ± 0.38	$\rho^0\ell\nu$	1.29 ± 0.20
		$\omega\ell\nu$	1.30 ± 0.54
total $X_u\ell\nu$	22.1 ± 3.3	total $X_u\ell\nu$	23.7 ± 3.5

Table 5.3: Assumed $b \to c\ell\nu$ branching fractions [9, 16, 35, 36, 37].

$B^0 \to$	$\mathcal{B}$ (%)	$B^+ \to$	$\mathcal{B}$ (%)
$D^-\ell\nu$	2.13 ± 0.14	$D^0\ell\nu$	2.30 ± 0.16
$D^{*-}\ell\nu$	5.53 ± 0.25	$D^{*0}\ell\nu$	5.95 ± 0.24
$D_1(2420)^-\ell\nu$	0.50 ± 0.08	$D_1(2420)^0\ell\nu$	0.54 ± 0.06
$D_2(2460)^{*-}\ell\nu$	0.39 ± 0.07	$D_2(2460)^{*0}\ell\nu$	0.42 ± 0.08
$D_0^{*-}\ell\nu$	0.43 ± 0.09	$D_0^{*0}\ell\nu$	0.45 ± 0.09
$D_1^{\prime-}\ell\nu$	0.80 ± 0.20	$D_1^{\prime 0}\ell\nu$	0.85 ± 0.20
nonresonant $D^{*-}\pi^0\ell\nu$	0.03 ± 0.04	nonresonant $D^{*+}\pi^-\ell\nu$	0.06 ± 0.04
nonresonant $D^{*0}\pi^-\ell\nu$	0.06 ± 0.04	nonresonant $D^{*0}\pi^0\ell\nu$	0.03 ± 0.02
nonresonant $D^-\pi^0\ell\nu$	0.09 ± 0.06	nonresonant $D^+\pi^-\ell\nu$	0.19 ± 0.12
nonresonant $D^0\pi^-\ell\nu$	0.19 ± 0.12	nonresonant $D^0\pi^0\ell\nu$	0.10 ± 0.06
total $X_c\ell\nu$	10.15 ± 0.16	total $X_c\ell\nu$	10.89 ± 0.16

Exclusive charmless semileptonic B decays were generated with a flat q^2 spectrum and are subsequently weighted[10] to reflect $b \to u\ell\nu$ form factors as calculated by Ball & Zwicky[11] and the charmless semileptonic branching fractions given in Table 5.2. Nonresonant charmless semileptonic B decays are weighted such that the full charmless decay spectrum (including exclusive decays) reflects the (exponential) shape function parameterization[12] described by De Fazio and Neubert [38] with parameters $m_b = 4.66\,\mathrm{GeV}/c^2$ and $a = 1.33$ determined empirically[13] [39]; hadronization is simulated with the `Jetset7.4` package [40].

While this analysis is not strongly sensitive to fluctuations in $b \to c\ell\nu$ branching fractions or form factors,[14] events with charmed semileptonic B decays are weighted to reflect the branching fractions listed in Table 5.3. Events with $B \to D\ell\nu$ and $B \to D^*\ell\nu$ transitions are weighted to reflect a form factor parameterization due to Caprini, Lellouch & Neubert [41].

The decays of η and η' mesons in simulated data are reweighted to reflect the branching

[10] See §9.1.1.

[11] The form factors discussed in §2.3.2 are generalized to describe decays of B mesons to pseudoscalar mesons; the authors provide form factors for decays to vector mesons as well.

[12] See §2.1.

[13] These parameters were determined from $b \to c\ell\nu$ and $b \to s\gamma$ decays; however, cited $|V_{ub}|$ results from inclusive $b \to u\ell\nu$ measurements discussed in §2.1 and §12 use parameters determined from only $b \to c\ell\nu$ as the equivalence between the shape function as inferred from $b \to s\gamma$ and $b \to u\ell\nu$ decays has since come into question due to the apparent size of subleading (non-universal) contributions.

[14] See §7.2.

Table 5.4: Assumed η, η' decay branching fractions [9].

	$\mathcal{B}$ (%)
$\eta \to \gamma\gamma$	39.38 ± 0.25
$\eta \to \pi\pi\pi^0$	22.7 ± 0.4
$\eta \to \pi^0\pi^0\pi^0$	32.51 ± 0.26
$\eta' \to \eta\pi^+\pi^-$	44.5 ± 1.4

fractions listed in Table 5.4.

5.2.2 Detector simulation

Simulated data events require additional weighting such that the reconstruction of $\pi^0 \to \gamma\gamma$ and particle identification rates match those measured in data. The quantification of the accuracy of the simulation of the detector response is discussed in detail in §9.2.

Chapter 6

Event, candidate selection

Due to the sheer volume of *BABAR* data,[1] the selection of events and candidates for the measurements described in this Dissertation is done over several successive stages, in sequential order: skim, preselection and main selection. Requirements imposed on events at the skim and preselection stages are looser than (and thus redundant with) requirements imposed at the main selection stage, but facilitate data processing by minimizing the need to process repeatedly the full and otherwise unwieldily large data set.

The selection criteria are described in the order in which they are applied. With the exception of the skim, selection is performed separately for each signal mode.

6.1 Skim

The coarsest event filter used is the `BToDlnu` skim. Skims at *BABAR* are collaboration-wide and general purpose, i.e., this skim might be used in any *BABAR* measurement requiring events containing a $B \to D\ell\nu$ final state. The `BToDlnu` skim loosely reconstructs $D^0 \to K^-\pi^+$, $K^-\pi^+\pi^+\pi^-$, $K^-\pi^+\pi^0$ and $K^0_S\pi^+\pi^-$, and $D^+ \to K^-\pi^+\pi^+$ and $K^0_S\pi^+$ decays. Candidate $K^\pm$, K^0_S, $\pi^\pm$ and π^0 mesons are taken from `KLHNotPion`, `KsDefault`, `GoodTracksVeryLoose` and `piOAllVeryLoose` respectively. Candidate K^0_S mesons are also required, as determined by the point of closest approach of the constituent track trajectories, to be consistent with having traveled more than 2 mm before decaying. A geometric fit recalculating $D^{0,\pm}$ candidates' constituent track trajectories with a $D^{0,\pm}$ vertex constraint provides a refined estimate of the $D^{0,\pm}$ candidate invariant mass m_D, which is required to be within 60 (or, for $K^-\pi^+\pi^0$, 100)

[1] See Table 5.1.

MeV/c^2 of the appropriate nominal $D^{0,\pm}$ mass [9].

Candidate D^0 mesons are combined[2] with soft (absolute momentum[3] less than 450 MeV/c) pions from `GoodTracksVeryLoose` and `pi0SoftDefaultMass` to form $D^{*+} \to D^0\pi^+$ and $D^{*0} \to D^0\pi^0$ candidates, with the requirement that the mass difference between the D^* and $D^{0,\pm}$ candidates be between 135 and 175 keV/c^2. Analogously, $D^{*+} \to D^+\pi^0$ candidates are reconstructed with the requirement that the D^{*+}-D^+ mass difference be between 140 and 150 keV/c^2.

For each event, the `BToDlnu` skim constructs a list of $D\ell$ candidate pairs: a $D^{(*)}$ candidate and non-overlapping lepton;[4] the lepton is required to have absolute momentum p^*_ℓ greater than 800 MeV/c and charge opposite that of the K and/or $D^{(*)}$ (when nonzero). Events with no viable $D\ell$ candidates are rejected. This list of $D\ell$ candidates for each event is the source of $D\ell$ candidates through the remainder of event and candidate selection.

6.1.1 Extension to the skim

An extension to the skim, `BTauNuSemiLepUser`, combines candidate $D^0(\ell)$ candidates with photons from `GoodPhotonDefault` to reconstruct $D^{*0} \to D^0\gamma$ with D^{*0}-D^0 mass difference between 120 and 170 keV/c^2.

Events with track multiplicity greater than twenty or net charge greater than ten (in units of the elementary charge) are rejected. Also imposed are the requirements that the invariant mass of a $D\ell$ candidate be no greater than 5.2791 MeV/c^2, and the $D\ell$ vertex probability—that the hypothesized charged $D^{0,\pm}$ daughters are consistent with having originated from a common vertex, and the same for the $D^{(*)}$ and lepton candidates—must be greater than 0.9‰. For each $D\ell$ candidate, a second non-overlapping lepton, with absolute momentum greater than 750 MeV/c, is required to be found in the event.

[2]When $D^*\ell$ candidates are constructed, the $D^{0,\pm}\ell$ candidate is kept as well.

[3]Hereafter, quantities are as measured in the center-of-mass frame unless otherwise noted.

[4]Unless otherwise noted, "lepton" refers to a lepton candidate satisfying `PidLHElectrons` or `MuonNNTight` selection criteria.

6.2 Preselection

Preselection, an additional pass of event filtering, is applied separately for each signal mode. Events not containing at least one $D\ell$ candidate such that:

- the $D^{(*)}$ charge is compatible with that of the signal mode being reconstructed,
- in $D^{*+} \to D^0\pi^+$, $D^{*0} \to D\pi^0$ and $D^{*+} \to D^+\pi^0$ ($D^{*0} \to D\gamma$) decays, the D^*-D mass difference is within 3 (15) MeV/c^2 of its nominal value [9],
- the D vertex probability—the probability that charged daughters of the $D^{0,\pm}$ candidate originated from a common vertex—is no less than 1‰,
- the $D\ell$ vertex probability is no less than 1‰,
- $|\cos(BY_D)| \leq 5$,
- there is an additional lepton in the event with absolute momentum no less than 800 MeV/c,
- the total charge of the event is zero, and
- the number of remaining tracks (other than the $D\ell$ candidate and the second lepton) in the event is consistent with the reconstruction mode (i.e., 0 for $\pi^0\ell\nu$, 1 for $\pi^\pm\ell\nu$, 0 or 2 for $\eta\ell\nu$ and 2 or 4 for $\eta'\ell\nu$)

are rejected.

6.3 Main selection

Events with more than twenty $D\ell$ candidates, as constructed at the `BTauNuSemiLepUser` stage,[5] are rejected. A requirement that the ratio (R_2) of the second and zeroth Fox-Wolfram moments [42] of the event not be greater than 0.5 suppresses background from non-$B\overline{B}$ events.

The presence of two leptons in the final state would permit background from $J/\psi \to \ell^+\ell^-$ decays, which are suppressed by the rejection of events containing oppositely charged tracks such that:

[5] i.e., not subject to preselection cuts.

Table 6.1: Resolution (σ) of $D^{0,\pm}$ masses and D^*-D mass differences, measured in data, simulated data.

	data	simulated data
	σ_{m_D} (MeV/c^2)	
$D^0 \to K^-\pi^+$	6.9	6.7
$D^0 \to K^-\pi^+\pi^+\pi^-$	8.7	8.9
$D^0 \to K^-\pi^+\pi^0$	19.1	17.9
$D^0 \to K^0_S\pi^+\pi^-$	11.0	10.2
$D^+ \to K^-\pi^+\pi^+$	5.7	5.8
$D^+ \to K^0_S\pi^+$	7.7	7.0
	$\sigma_{m_{D^*}-m_D}$ (MeV/c^2)	
$D^{*+} \to D^0\pi^+$	1.0	0.9
$D^{*0} \to D^0\pi^0$	2.2	1.5
$D^{*+} \to D^+\pi^0$	0.9	0.9
$D^{*0} \to D^0\gamma$	5.7	4.1

Table 6.2: Definition of $D^{0,\pm}$ mass "sideband" regions. This would be uniform for sample and D decay mode, if not for limitations imposed by the D mass cut at the skim level.

	m_D sideband (σ_{m_D})	
	data	simulated data
$D^0 \to K^-\pi^+$	4 – 7	4 – 7
$D^0 \to K^-\pi^+\pi^+\pi^-$	3.5 – 6.5	3.5 – 6.5
$D^0 \to K^-\pi^+\pi^0$	3.5 – 5	3.5 – 5.5
$D^0 \to K^0_S\pi\pi$	3.5 – 5	3.5 – 5.5
$D^+ \to K^-\pi^+\pi^+$	4 – 7	4 – 7
$D^+ \to K^0_S\pi^+$	4 – 7	4 – 7

- at least one track is identified as an electron (using the `PidLHElectrons` selector) or muon (`MuonNNTight`),
- the other is identified with looser criteria as a lepton of the same species (i.e., electrons via `ElectronsLoose` or muons via `MinimumIonizing`),
- the tracks have a χ^2 vertex probability greater than 2.2%, and
- their invariant mass, if they are electrons (muons), is between 3.01 (3.08) and 3.11 (3.12) GeV/c^2.

6.3.1 Tag side selection

For each event, $D\ell$ candidates are rejected unless:

- the D vertex probability is at least 1‰,
- the $D\ell$ probability is at least 1‰,
- the $D\ell$ system has invariant mass no less than $3\,\mathrm{GeV}/c^2$,
- the associated lepton has momentum $p^*_\ell \geq 0.8\,\mathrm{GeV}/c$,
- the invariant mass of the $D^{0,\pm}$ candidate is within $n\sigma$ of the appropriate nominal value, where n is the outside edge of the appropriate sideband region (i.e., 5, 5.5, 6.5 or 7), which is described in Table 6.2,
- in the case of a reconstructed D^*, the D^*-D mass difference $m_{D^*} - m_D$ is within 3.7σ of the appropriate nominal value;
- $|\cos(BY_D)| \leq 5$,
- the event does not contain any K^0_S ($\rightarrow \pi^+\pi^-$) candidates (from the `KsDefault` list) not overlapping the $D\ell$ candidate, and
- there is exactly one additional lepton (the signal side lepton) in the event with absolute momentum p^*_ℓ no less than $800\,\mathrm{MeV}/c$. If the two leptons are oppositely charged electrons, the cosine of the angle between them is required to be no greater than 0.995; this requirement suppresses electrons originating from photon conversions.

The D mass and D^*-D mass difference requirements are stated in terms of the respective resolutions σ, as the σe, which are measured directly from data and simulated data, are known to be different. They are listed in Table 6.1. This D mass window includes the sideband regions; for later signal extraction, the D mass peak region will be defined to be within 2.3σ of the appropriate nominal D mass. The signal extraction technique[6] does not rely on accurate modeling of D mass or D^*-D mass difference spectra.

6.3.2 Signal side selection

For each $D\ell$-ℓ candidate, signal side hadronic system candidates X are reconstructed from

[6] See §8.

- charged tracks[7] from `ChargedTracks` which fulfill the requirements:
  - the track candidate's laboratory frame polar angle is between 0.41 and 2.54 rad,
  - it has transverse momentum greater than 60 MeV/c and, if it is found only in the SVT, less than 200 MeV/c, and
  - its point of closest approach to the beam line is within 5 cm in the longitudinal direction (in the laboratory frame) and 1.5 cm in the transverse plane of the IP,

  and are assumed to be pions,[8]
- neutral pion candidates from `pi0DefaultMass` and
- photon candidates from `CalorNeutral`

that do not overlap with the $D\ell$ candidate or the signal side lepton. Once the signal side of the event is reconstructed, there must be no remaining tracks (from `CharedTracks`) in the event. It is reconstructed as follows:

- For $B \to \pi^{\pm}\ell\nu$ candidates, the pion and signal side lepton are required to have opposite charge.
- For $B \to \pi^0\ell\nu$ candidates, the tag and signal side leptons are required to have opposite charge. Due to imperfect modeling of neutral backgrounds in simulated data, it is additionally imposed that $p^*_{\pi^0} + p^*_\ell \geq 2.6\,\mathrm{GeV}/c$, where $p^*_{\pi^0}$ and p^*_ℓ are the absolute

[7]The tracks list is cleaned of "loopers" and "ghost" tracks, situations in which a single physical track is reconstructed as multiple tracks in the list.

A sufficiently low transverse momentum (p_t) track will have a helical trajectory in *BABAR*'s magnetic field, which will be reconstructed as multiple tracks—loopers—half moving away from the beam line and half moving toward it (and having the wrong charge). Two like charge tracks are considered loopers if their trajectories have $p_\mathrm{t} < 250\,\mathrm{MeV}/c$ (Quantities in this Footnote are as measured in the laboratory frame of reference.), absolute difference in transverse momentum $|\Delta p_\mathrm{t}| < 120\,\mathrm{MeV}/c$, absolute difference in azimuthal angle $|\Delta\phi| < 0.1$ rad and absolute difference in polar angle $|\Delta\theta| < 0.1$. Tracks of opposite charge are considered loopers under the same conditions. When loopers are found, all are rejected except the one whose point of closest approach to the beam line is closest, in the longitudinal direction, to the IP.

Ghost tracks result from a physical track's DCH hits being divided and reconstructed as two (or more) logical tracks. When two tracks with like charge have trajectories such that $p_\mathrm{t} < 350\,\mathrm{MeV}/c$, $|\Delta p_\mathrm{t}| < 150\,\mathrm{MeV}/c$, $|\Delta\phi| < 0.1$ and $|\Delta\theta| < 0.1$, the one with fewer hits in the DCH is considered a ghost track and rejected.

[8]The only particle identification criterion applied is the effective requirement that they are not leptons.

momenta of the pion and (signal side) lepton candidates respectively, and the daughter photons of the pion candidate each satisfy the photon quality requirements:

  - the photon candidate deposited energy in at least two EMC crystals,
  - its polar angle in the laboratory frame is between 0.32 and 2.44 rad,
  - its laboratory frame energy is greater than 80 MeV,
  - the cluster's lateral moment is less than 0.9, and
  - the closest track to it has track cluster separation $\Delta\alpha$ no less than 0.11.[9]

  These requirements have no significant impact on overall sensitivity, but aid in suppressing detector backgrounds.

- The $B \to \eta\ell\nu$ decay is reconstructed via the decays $\eta \to \gamma\gamma$, $\pi^+\pi^-\pi^0$ and $\pi^0\pi^0\pi^0$. Candidate $\eta \to \gamma\gamma$ photon pairs are required to have invariant mass between 500 and 570 MeV/c^2; each photon is required to have laboratory frame energy E_γ no less than 55 MeV. Candidate η mesons reconstructed in the pionic modes are required to have invariant mass between 530 and 560 MeV/c^2. For $\eta \to \pi^+\pi^-\pi^0$ decays, the π^0 laboratory frame absolute momentum p_{π^0} is required to be no less than 280 MeV/c, and the estimated distance of closest approach (DOCA) of the π^+ and π^- tracks must be no greater than 3.4 mm.[10] For $\eta \to \pi^0\pi^0\pi^0$ decays, each pion is required to have no less than 180 MeV/c of laboratory frame absolute momentum p_{π^0}. As with $B \to \pi^0\ell\nu$ candidates, tag and signal side leptons are required to have opposite charge.

- The $B \to \eta'\ell\nu$ decay is reconstructed via only the $\eta' \to \eta\pi^+\pi^-$ decay,[11] with η

[9] Where a track has (in the laboratory frame) angular position $(\theta_{\rm tr}, \phi_{\rm tr})$ at the EMC, and the photon candidate $(\theta_\gamma, \phi_\gamma)$, for that track-photon combination,

$$\Delta\alpha \equiv \cos^{-1}(\cos\theta_\gamma \cos\theta_{\rm tr} + \sin\theta_\gamma \sin\theta_{\rm tr} \cos(\phi_\gamma - \phi_{\rm tr})). \tag{6.1}$$

The "closest" track to that photon candidate is defined as the one with the smallest $\Delta\alpha$. This allows for matches that may have been missed by the standard `CalorNeutral` cluster-track matching algorithm.

[10] This "distance of closest approach" is a rough estimate made by extrapolating from the tracks' points of closest approach to the beamline, assuming negligible track curvature.

[11] The $\eta' \to \rho\gamma$ decay is not considered, as it has not proven possible to separate $\rho \to \pi^+\pi^-$ decays from other (e.g., random) $\pi^+\pi^-$ combinations with sufficient statistical robustness. For the same reason, the analysis techniques described in this Dissertation are not used to study the decays $B \to \rho^{\pm,0}\ell\nu$ or $B \to \omega\ell\nu$.

candidates selected as above; η' candidates are required to have invariant mass bewteen 920 and 970 MeV/c^2, and the DOCA of the additional pions (estimated as in the $\eta \to \pi^+\pi^-\pi^0$ case) is required to be no greater than 1.4 mm. Again, tag and signal side leptons are required to be of opposite charge.

For each $D\ell$-$X\ell$ candidate, it is further required that

- there is no more than 140 MeV for $\pi^\pm\ell\nu$ or 70 MeV for all other signal modes of extra neutral energy ($E^*_{\rm extra}$) in the event, and
- $|\cos(BY_X)| \leq 5$.

The remaining neutral energy is calculated using photon candidates (from `CalorNeutral`) meeting requirements identical to those applied to π^0 daughters in $B \to \pi^0\ell\nu$ candidates. Also removed are photon candidates consistent with having originated via bremsstrahlung, i.e., those whose

- (laboratory frame) polar angle is within 35 mrad of an electron's, and
- (laboratory frame) azimuth lies between that of that electron's direction at the origin and at the EMC, but not within 50 mrad of the former,

and photon candidates consistent with having originated from D^* cascades: because reconstruction efficiencies for $D^* \to D\pi^0$ and $D^* \to D\gamma$ decays are relatively low (and the relatively rare $D^{*\pm} \to D^\pm\gamma$ decay is not explicitly reconstructed), up to two photons that are consistent with having originated from such a decay, i.e., when

- the $D\ell$ candidate is $D^0\ell$ or $D^\pm\ell$,
- the mass difference between the $D\gamma(\gamma)$ system and the D itself is no greater than 150 MeV/c^2, and
- after recalculation with the photon(s), $-2.5 \leq \cos(BY_D) \leq 1.1$,

can be removed. In the case that multiple photon(pair)s satisfy the cascade criteria, the photon (pair) resulting in the smallest $|\cos(BY_D)|$ is removed. In the bremsstrahlung and cascade cases, the energy of any removed photons is assigned to the appropriate electron or D

Table 6.3: Average number of candidates passing selection requirements (before candidate selection) in each signal channel. Multiple $\eta' \to \eta\pi\pi$ candidates can have identical final states if different (grand)daughters are hypothesized to be daughters of the intermediate η meson.

	signal	other $u\ell\nu$	$B\overline{B}$	off-peak data	on-peak data
$\pi^{\pm}\ell\nu$	1.15	1.09	1.13	1.04	1.11
$\pi^{0}\ell\nu$	1.35	1.26	1.33	1.18	1.31
$\eta\ell\nu$	1.45	1.40	1.49	1.08	1.42
$\eta'\ell\nu$	1.58	1.41	1.47	n/a	1.56

candidate and is used in the $\cos(BY_X)$ computation above, the following $\cos(BY_D)$ computation and computations of $\cos^2\phi_B$ in the signal extraction.[12]

For events with multiple candidates fulfilling all above requirements, the "best" candidate is chosen by smallest $|\cos(BY_D)|$. If multiple candidates in the same signal mode have the same $|\cos(BY_D)|$ (i.e., a single $D\ell$ tag is matched with multiple $X\ell$ candidates), the $X\ell$ candidate is then chosen such that X has greatest absolute momentum. The average candidate multiplicity is given in Table 6.3. Once the best candidate is selected, it is required to have $\cos^2\phi_B$ within the range ($\cos^2\phi_B \leq 20$) over which the signal yield is extraced.[13] If the mass of the associated $D^{0,\pm}$ candidate lies in the D mass sideband window, the event receives, for the purposes of scaling sideband events to the abundance of combinatoric $D^{0,\pm}$ events in the D mass peak window, a weight equal to the ratio of the width of the D mass peak window to that of the D mass sideband window. If the D mass is in neither the D mass peak or sideband windows, it is discarded.

There are no selection criteria based on X-ℓ vertexing. Previous studies have found this to be of negligible benefit, as in many $B\overline{B}$ background events, the X and ℓ candidates originate from a common parent, e.g., $B^0 \to \rho^-\ell^+\nu$ with $\rho^- \to \pi^-\pi^0$ reconstructed as $B^0 \to \pi^-\ell^+\nu$.

As each signal mode is treated separately; in principle, a single event can have signal candidates in multiple modes.[14] Given the cut on extra tracks and remaining neutral energy, the effect of such multiplicity is negligible.

[12] See §8.

[13] See §8.

[14] See §10.1.

6.4 Optimization

These selection criteria have been optimized using the simulated (and off-peak) data for signal significance in an ad hoc $\cos^2\phi_B \leq 1.5$ window.[15] For a given signal mode, $S_{\rm pk}$ and $S_{\rm sb}$ are defined, respectively, as the number of expected events from the appropriate signal source in this window, such that the D mass is in the peak ("pk") and sideband ("sb") region, respectively;[16] $B_{\rm pk}$ and $B_{\rm sb}$ are defined analogously for the remainder of the simulated (and off-peak) data. The statistical significance is estimated as

$$S = \frac{S_{\rm pk} - S_{\rm sb}}{\sqrt{\sigma^2_{S_{\rm pk}} + \sigma^2_{B_{\rm pk}} + \sigma^2_{S_{\rm sb}} + \sigma^2_{B_{\rm sb}}}} \tag{6.2}$$

where $\sigma_{S_{\rm pk}}$, $\sigma_{B_{\rm pk}}$, etc. are the expected statistical errors on $S_{\rm pk}$, $B_{\rm pk}$, etc., respectively.[17] Each requirement is varied, with the others kept constant, to maximize S.

Requirements common to all signal modes—i.e., those not on the charmless meson candidate itself or extra neutral energy—were optimized for the combined significance[18] of $\pi^\pm\ell\nu$ and $\pi^0\ell\nu$ modes. Figures 6.1–6.3 show the results of several such optimizations: the vertex probability and mass requirements for J/ψ candidate rejection, the width of the D mass peak window (Because the combined significance shows no optimum, the $\pi^\pm\ell\nu$ significance is optimized.), the width of the D^*-D mass difference window, minimum absolute lepton momenta (As the significance decreases with this value, it is left to the smallest tag side[19] lepton momentum allowed by the `BToDlnu` skim.) and the maximum cluster lateral moment and minimum required track-cluster separation for photon candidates. The selection criteria are relatively robust, as their efficacy is not heavily sensitive to small variations in their specific values.

[15] This approximates $\cos^2\phi_B \leq 1$ up to resolution.

[16] Optima are assumed to be independent of the definition of the D mass sideband region. The sideband regions are defined differently for data and simulated data; due to differences in σ_{m_D}, this is a reasonable statistical description of the sideband events.

[17] I.e., $\sigma_{S_{\rm pk}} = \sqrt{S_{\rm pk}}$ and $\sigma_{B_{\rm pk}} = \sqrt{B_{\rm pk}}$; $\sigma_{S_{\rm sb}}$ and $\sigma_{B_{\rm sb}}$ are the square roots of the appropriate weighted sum of squared sideband weights.

[18] assuming isospin relations; see §10.2.

[19] For simplicity, the signal side lepton is held to the same requirements.

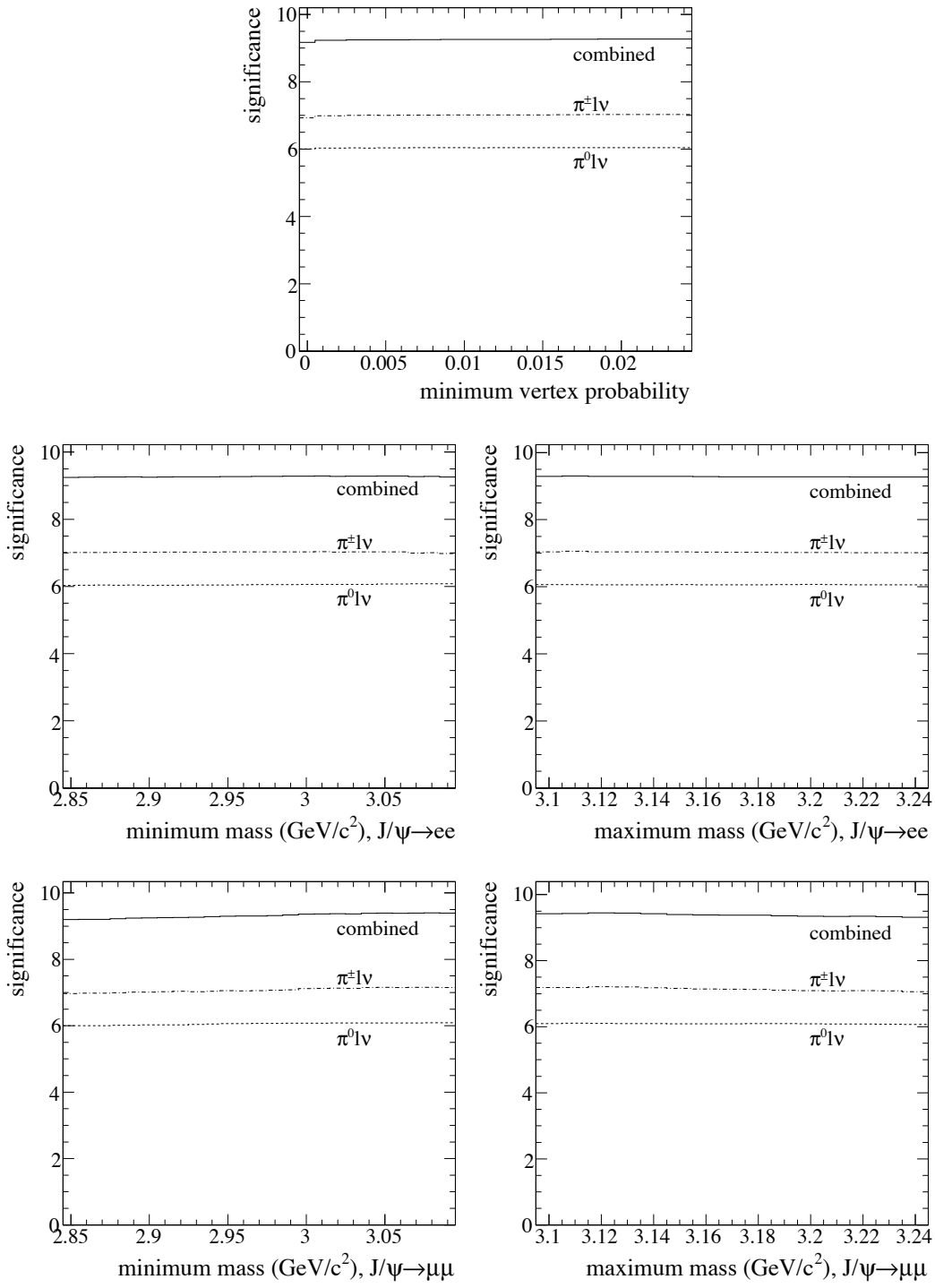

Figure 6.1: Statistical significance (of $\pi^{\pm}\ell\nu$ and $\pi^{0}\ell\nu$ signal modes) as a function of various J/ψ meson (event) rejection criteria. These criteria are common to all signal modes.

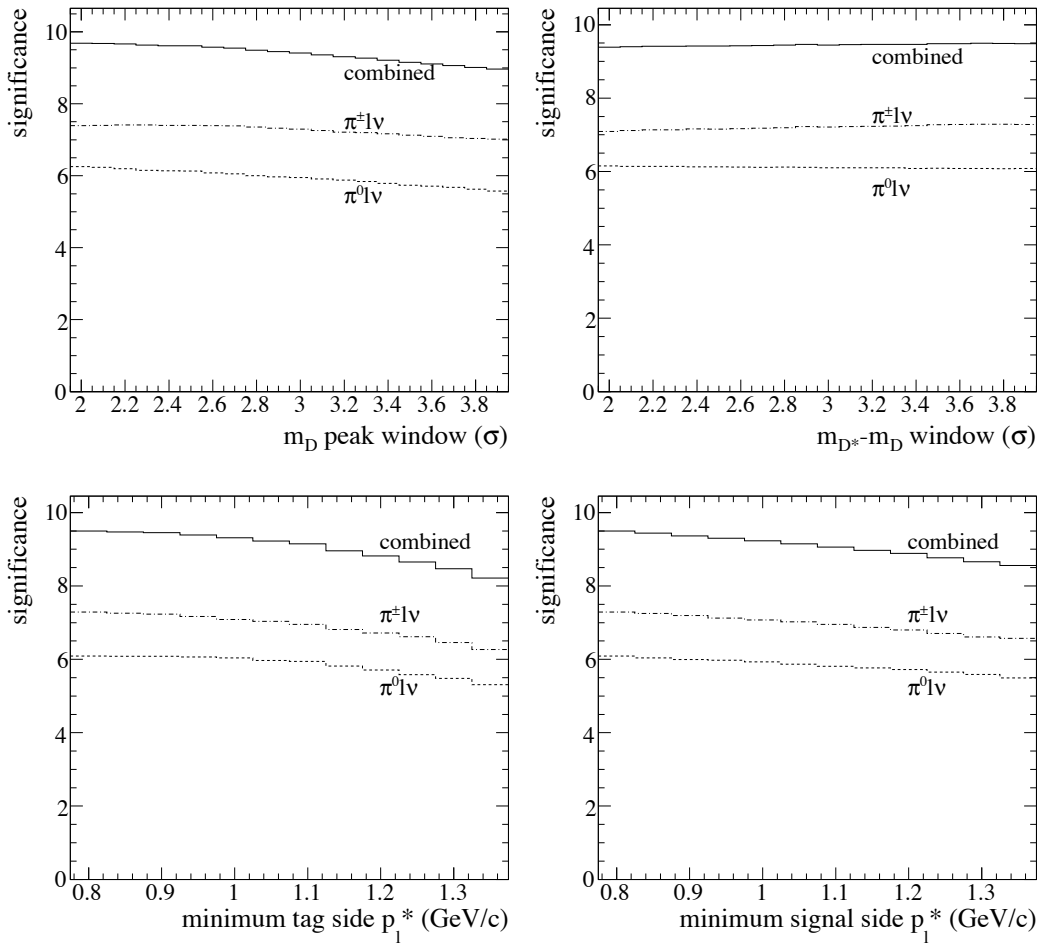

Figure 6.2: Statistical significance (of $\pi^{\pm}\ell\nu$ and $\pi^0\ell\nu$ signal modes) as a function of various $D\ell$ candidate selection requirements. These requirements are common to all signal modes.

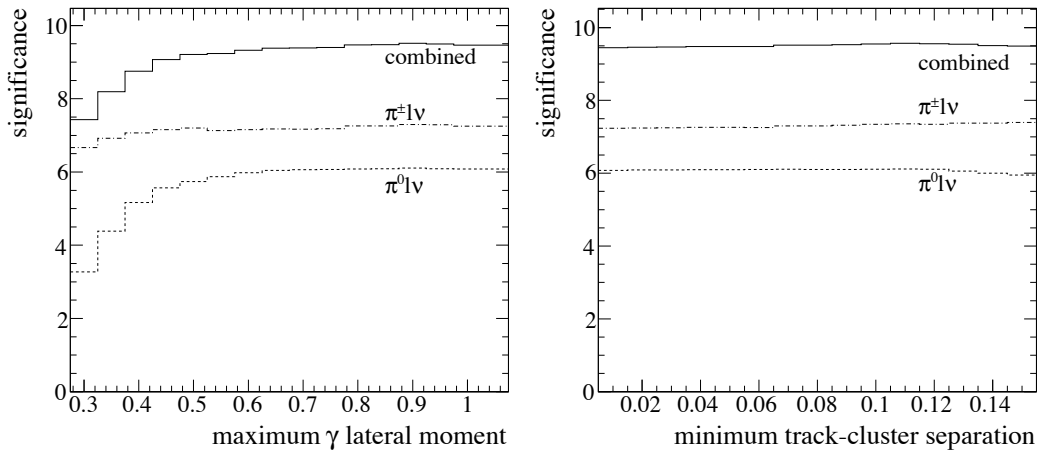

Figure 6.3: Statistical significance (of $\pi^{\pm}\ell\nu$ and $\pi^0\ell\nu$ signal modes) as a function of photon quality requirements. These requirements are common to all signal modes.

Other requirements common to all signal modes that were optimized but are not shown are: particle identification requirements on J/ψ candidates' daughters, whether to reconstruct $D^{*0} \to D^*\gamma$ on the tag side, whether to apply explicit particle identification requirements to signal side charged tracks (other than the lepton), whether to recover photons consistent with having originated from bremsstrahlung, whether to recover photons (and how many) consistent from having originated from D^* cascades and, in these last two cases, whether the energies of recovered photons should be considered in computing $\cos(BY_X)$, $\cos(BY_D)$ and $\cos\phi_B$.

For η candidates, it is optimal to require a minimum photon energy in the decay $\eta \to \gamma\gamma$, a maximum distance of closest approach between charged pion tracks in the decay $\eta \to \pi^+\pi^-\pi^0$ and minimum absolute π^0 momenta in both pionic η decays, as seen in Figure 6.4. The optimization results for the η mass windows are shown in Figure 6.5.

The results of optimizing the η' candidate mass window and charged pion distance requirement are shown in Figure 6.6.

Figure 6.7 shows the optimization of allowed maximum extra neutral energy for the $\pi^{\pm}\ell\nu$ and $\pi^0\ell\nu$ signal modes. Extra neutral energy tends to come from the tag side of the event; using the $\pi^0\ell\nu$ neutral energy requirement for the $\eta\ell\nu$ and $\eta'\ell\nu$ signal modes as well simplifies efficiency studies;[20] independent optimization of the allowed maximum neutral energy for the $\eta^{(\prime)}$ signal modes suggest values in good agreement.

[20] See §7.2.

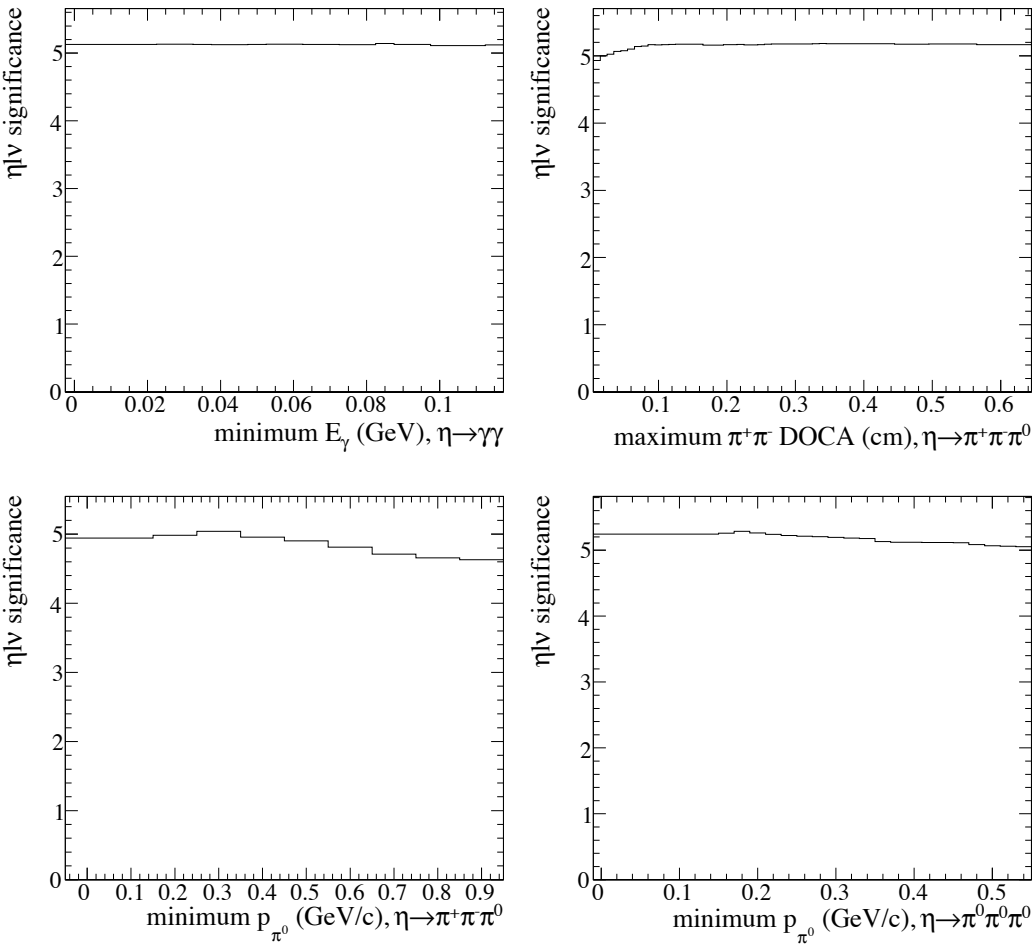

Figure 6.4: Statistical significance of $\eta\ell\nu$ as a function of η daughter requirements.

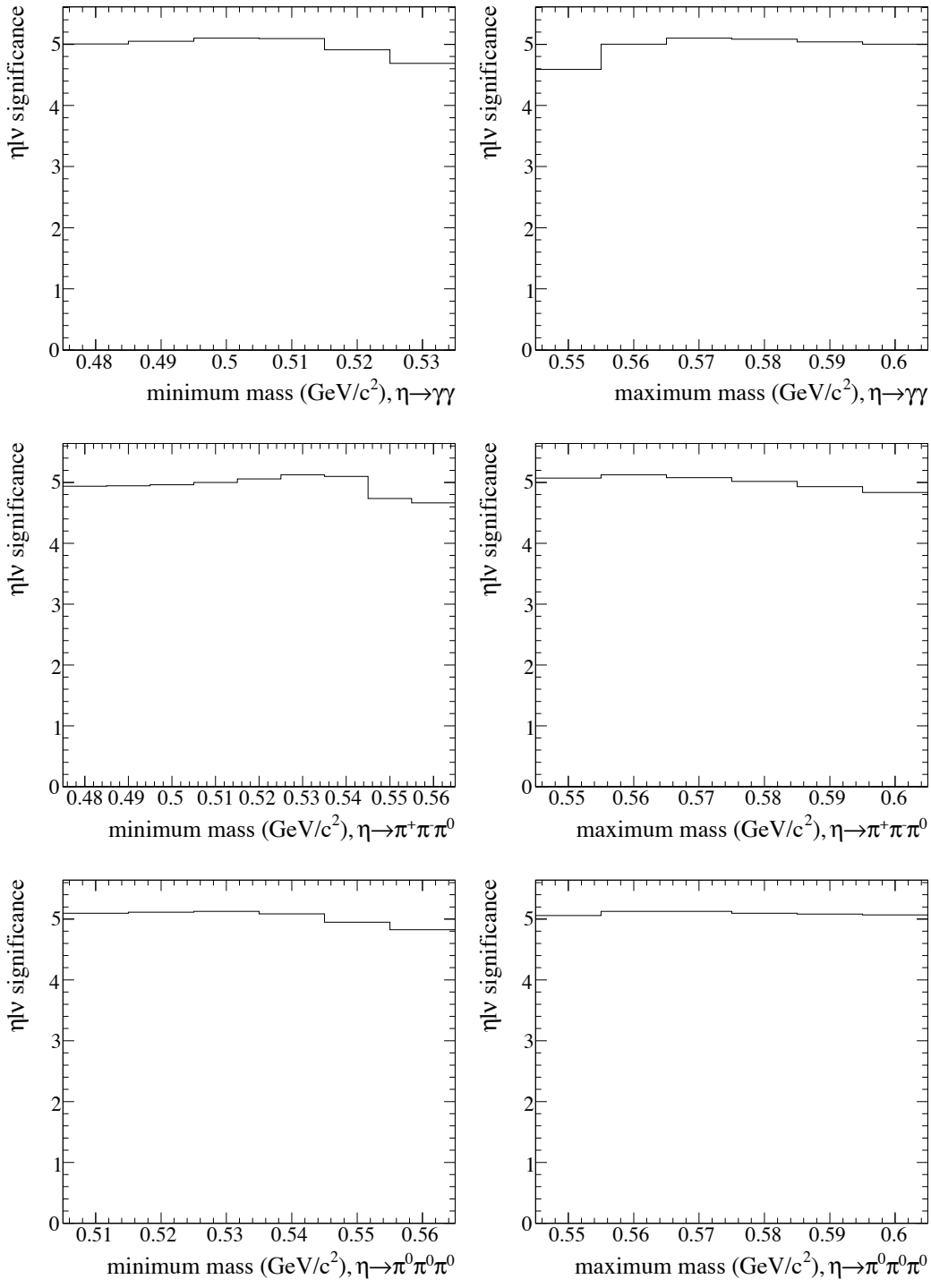

Figure 6.5: Statistical significance of $\eta\ell\nu$ as a function of η candidate mass requirements.

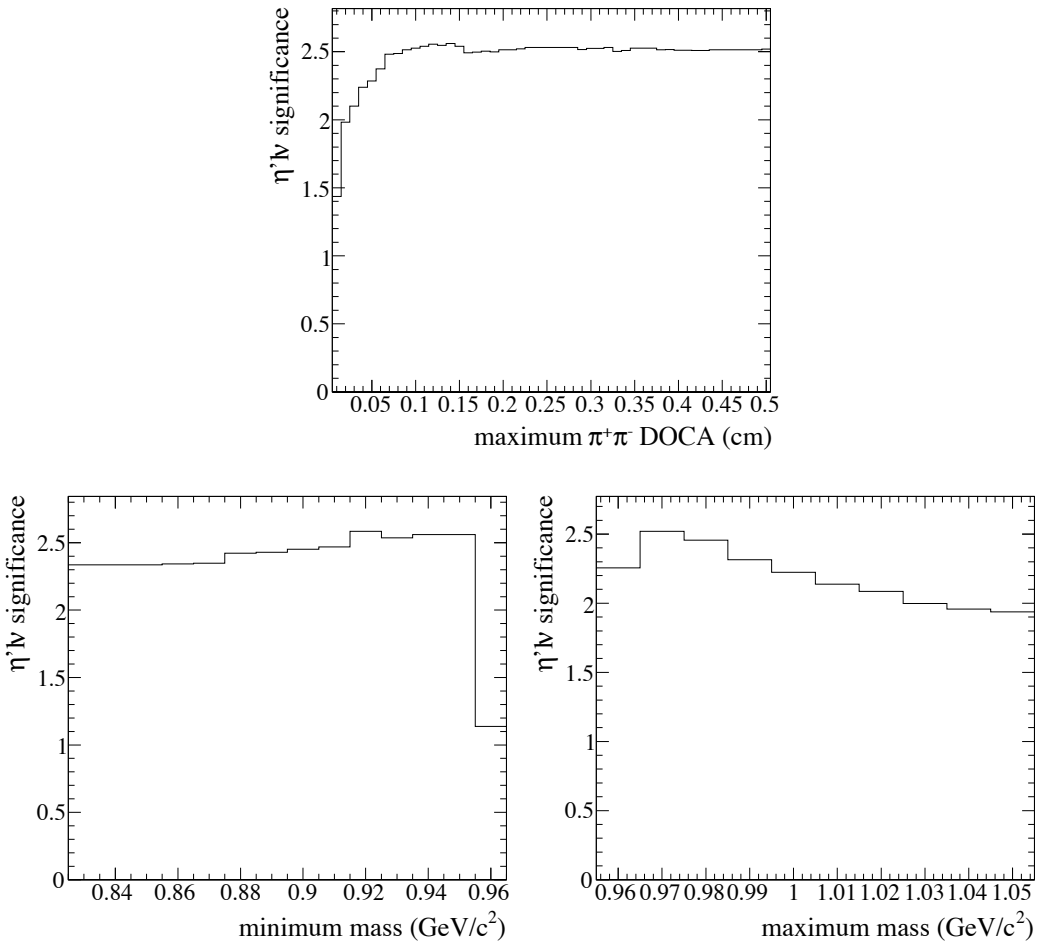

Figure 6.6: Statistical significance of $\eta'\ell\nu$ as a function of η' candidate requirements.

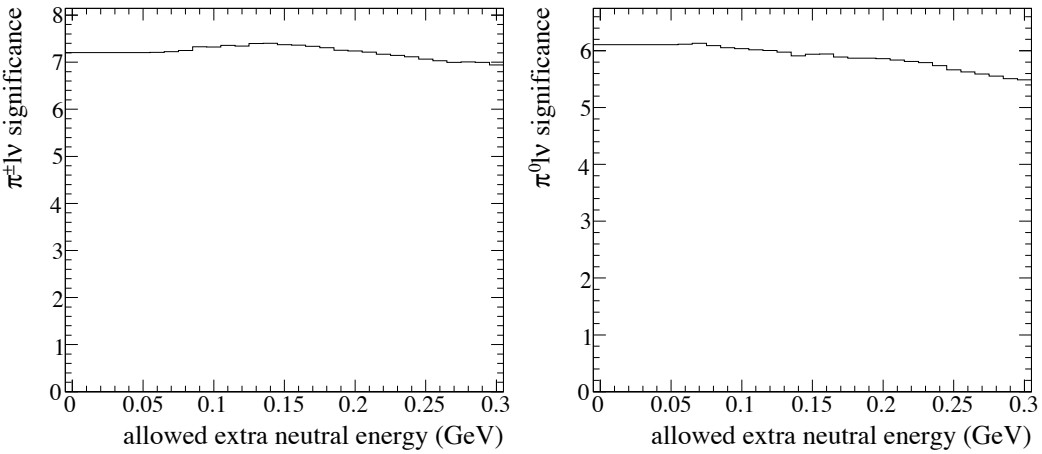

Figure 6.7: Statistical significance for $\pi^{\pm}\ell\nu$ and $\pi^{0}\ell\nu$ signal modes, as a function of allowed extra neutral energy.

6.5 Validation

Figures 6.8–6.17 show candidate-level comparisons of on-peak data to simulated data plus off-peak data for the selection variables described. All skim and preselection requirements described in §6.1–6.2 has been applied to data shown in these Figures; for each plot, other selection requirements described in §6.3–6.3.2 preceding those imposed on the variable plotted are also applied.

In some cases the normalizations of data and simulated data show discrepancies, due in part to inaccurate simulation of (neutral) backgrounds, many of which are suppressed by the requirement on extra neutral energy. The sizes of background contributions to the overall data sample are taken as free parameters in the yield extraction in §8.

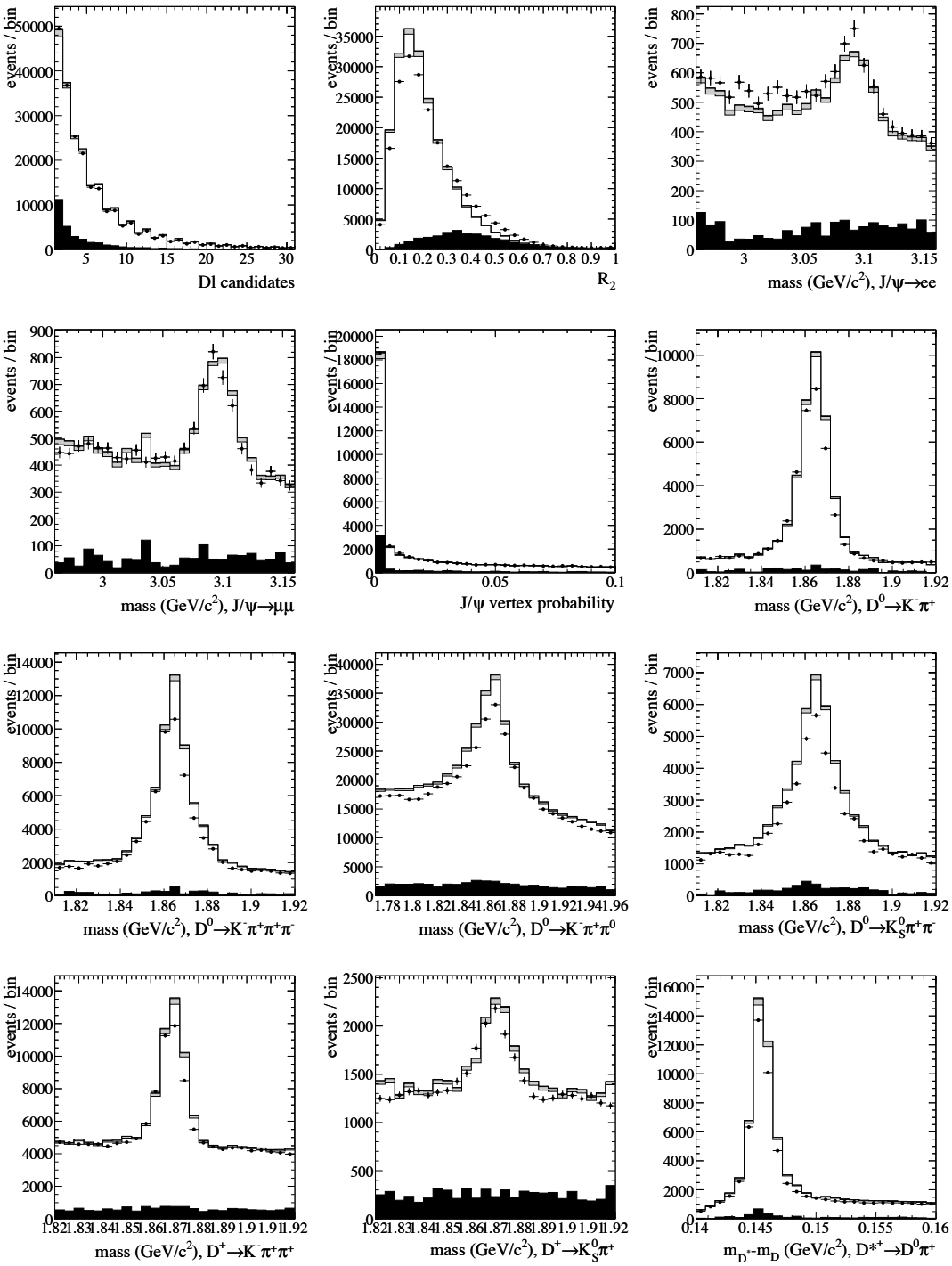

Figure 6.8: Comparison of on-peak data and simulated data (plus off-peak data) for the $\pi^{\pm}\ell\nu$ channel. Points are on-peak data; histograms (stacked) are: simulated signal ((dark) grey), other simulated charmless semileptonic decays (light grey), simulated generic $B\overline{B}$ decays (white) and off-peak data (black).

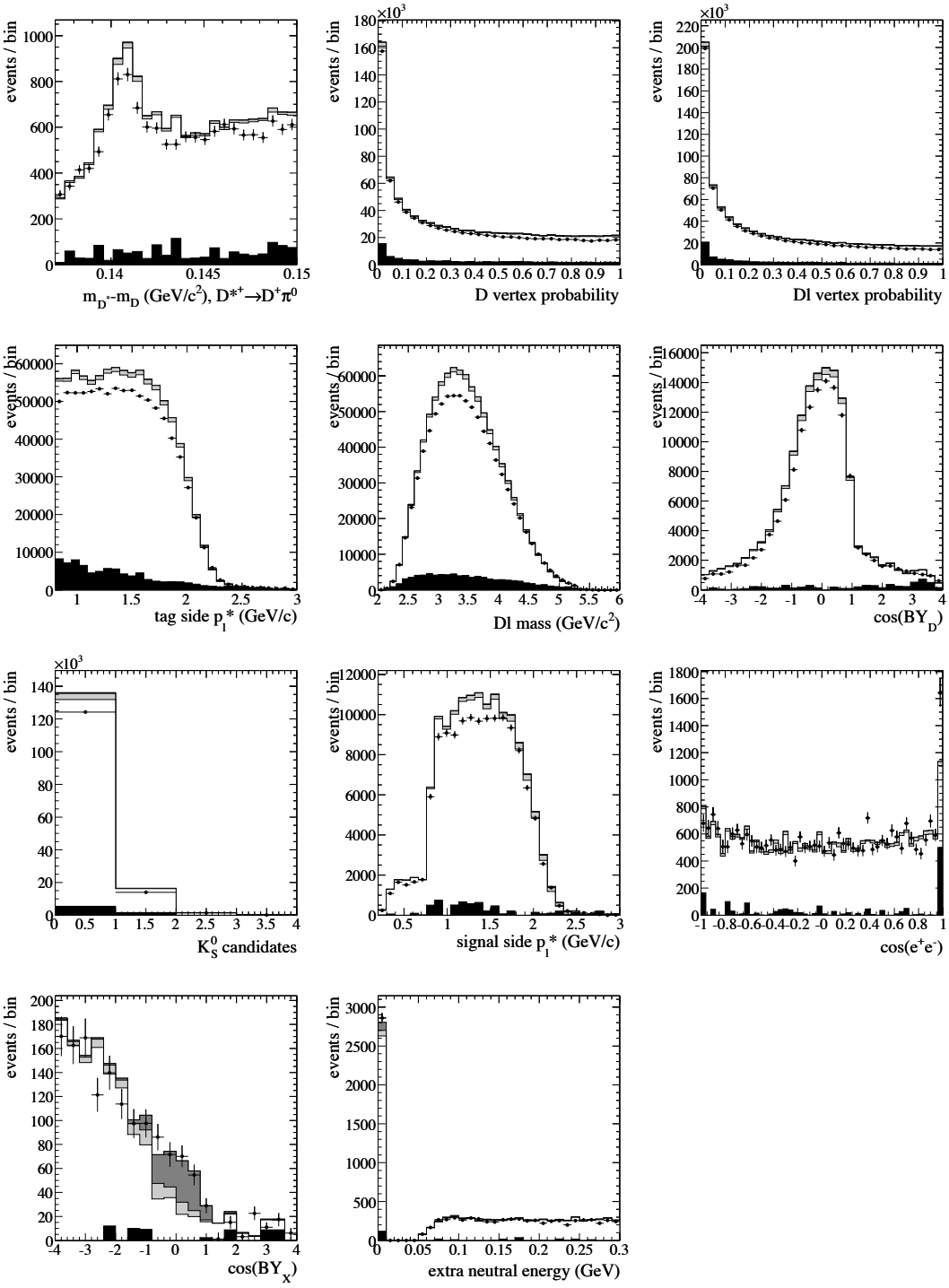

Figure 6.9: Continuation of Figure 6.8.

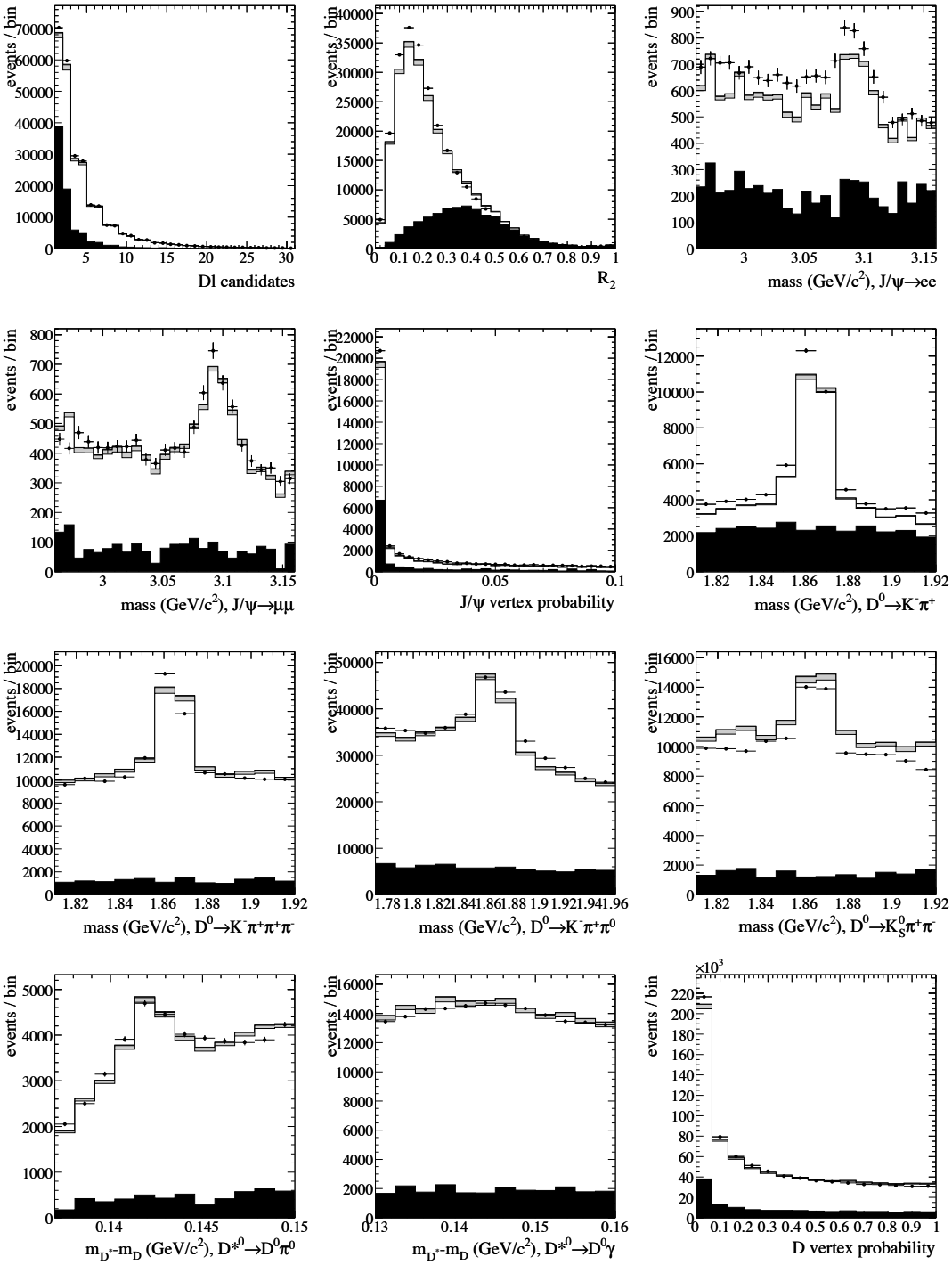

Figure 6.10: Analogous to Figure 6.8, for $\pi^0 \ell \nu$ channel.

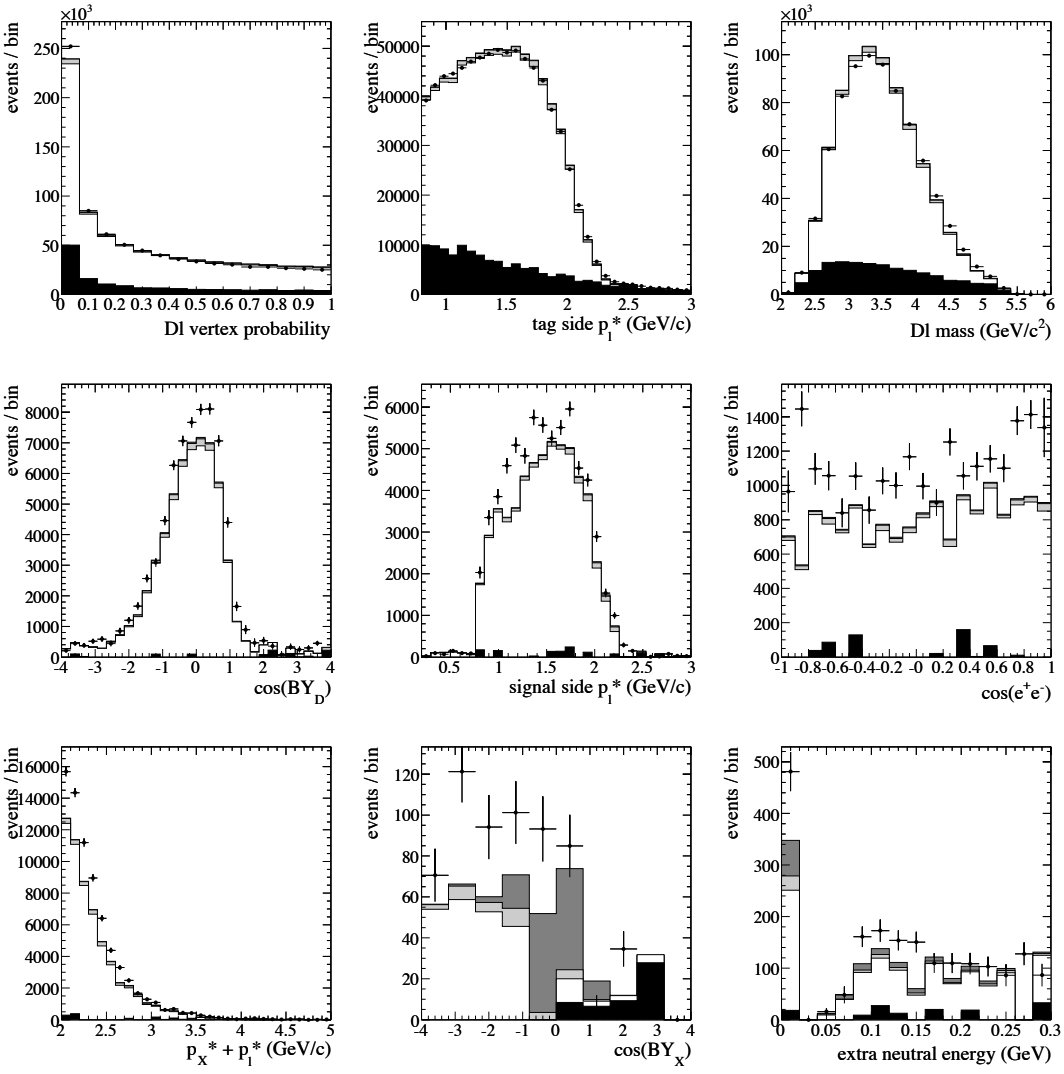

Figure 6.11: Continuation of Figure 6.10.

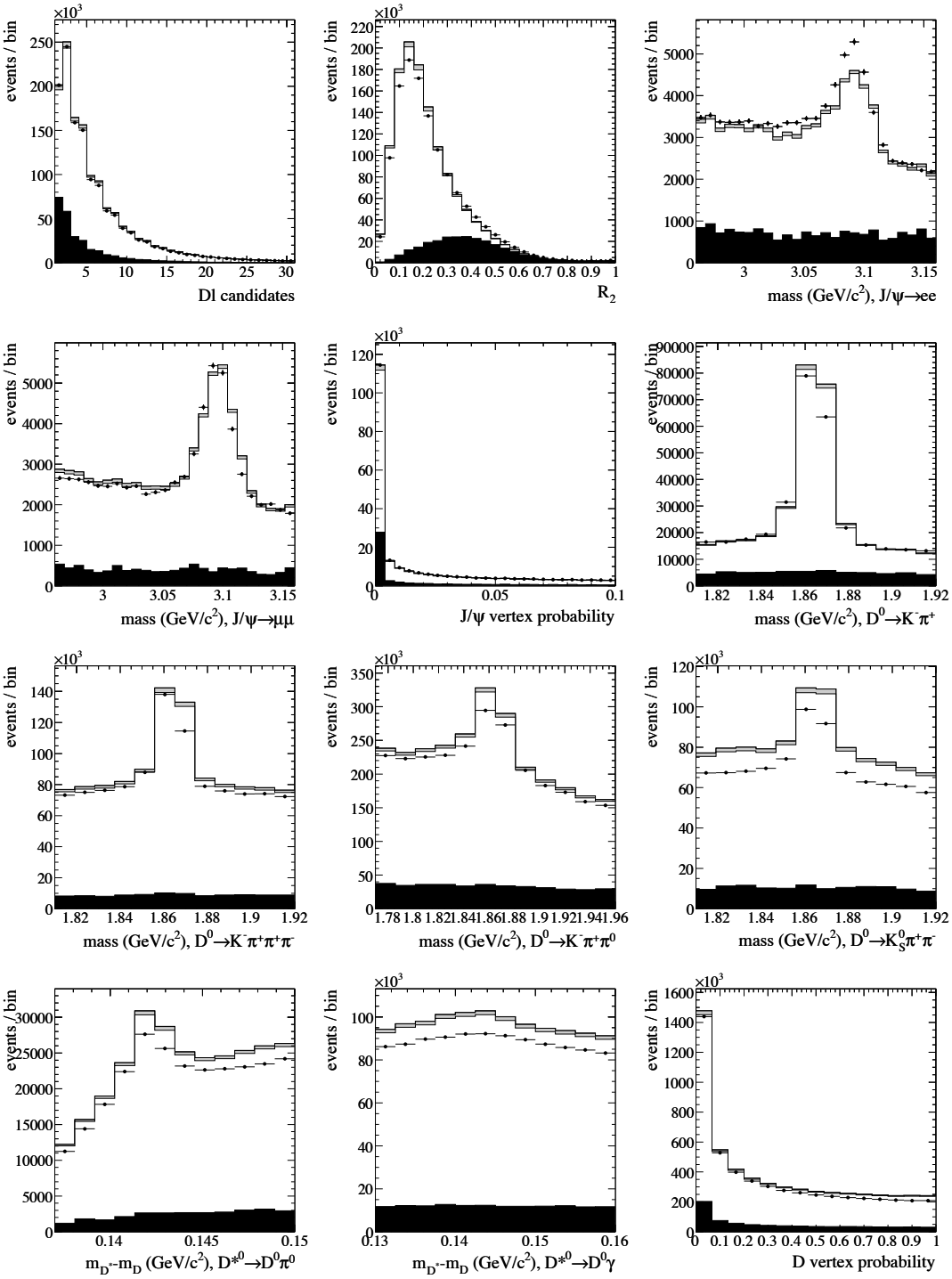

Figure 6.12: Analogous to Figure 6.8, for $\eta\ell\nu$ channel.

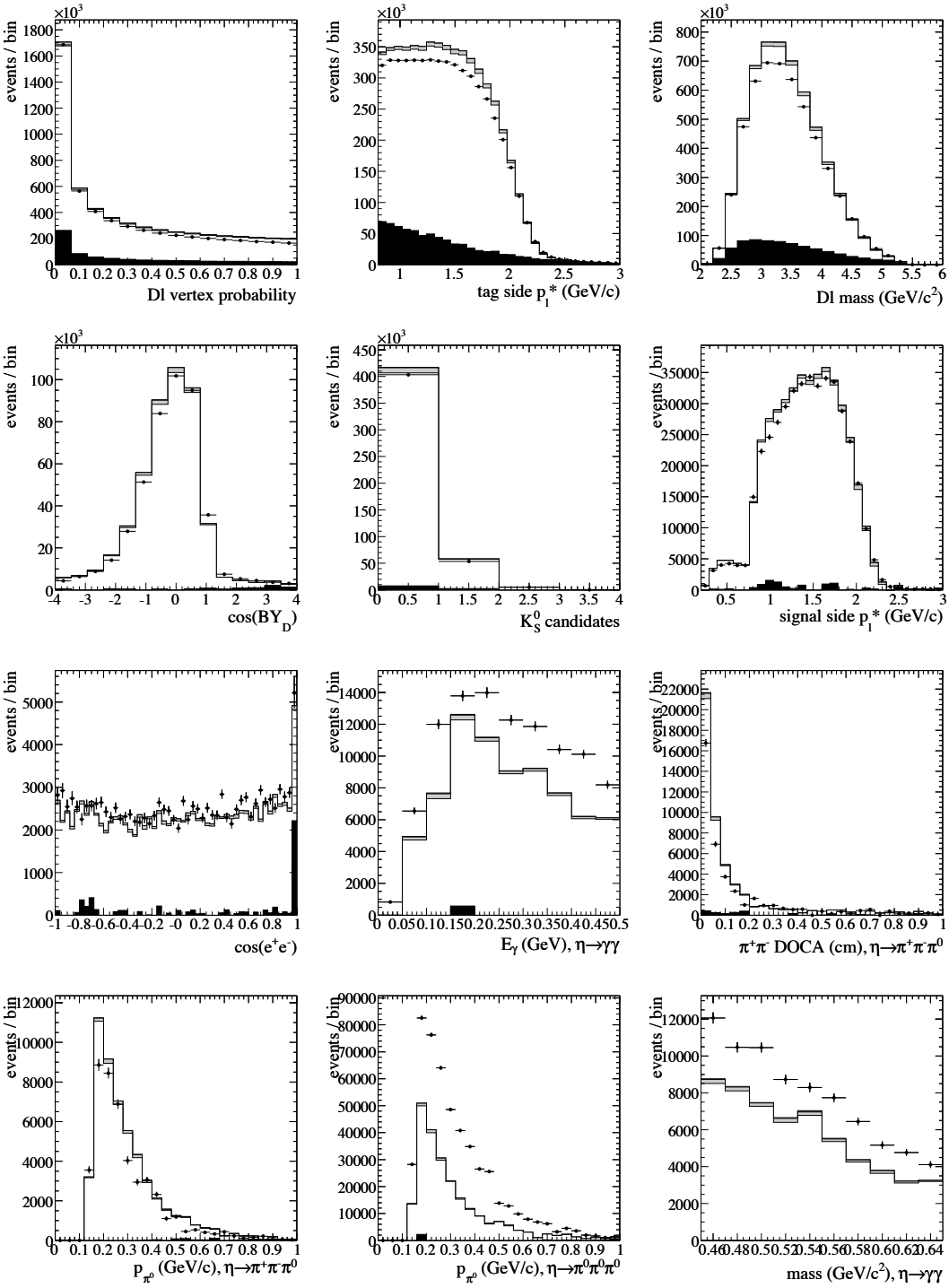

Figure 6.13: Continuation of Figure 6.12.

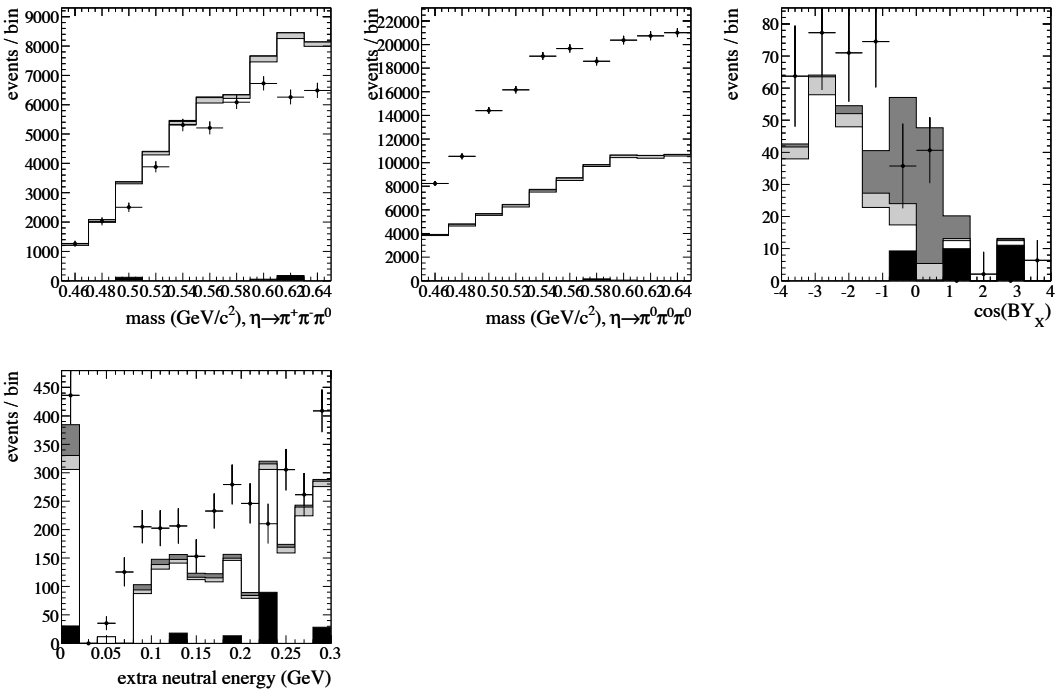

Figure 6.14: Continuation of Figure 6.13.

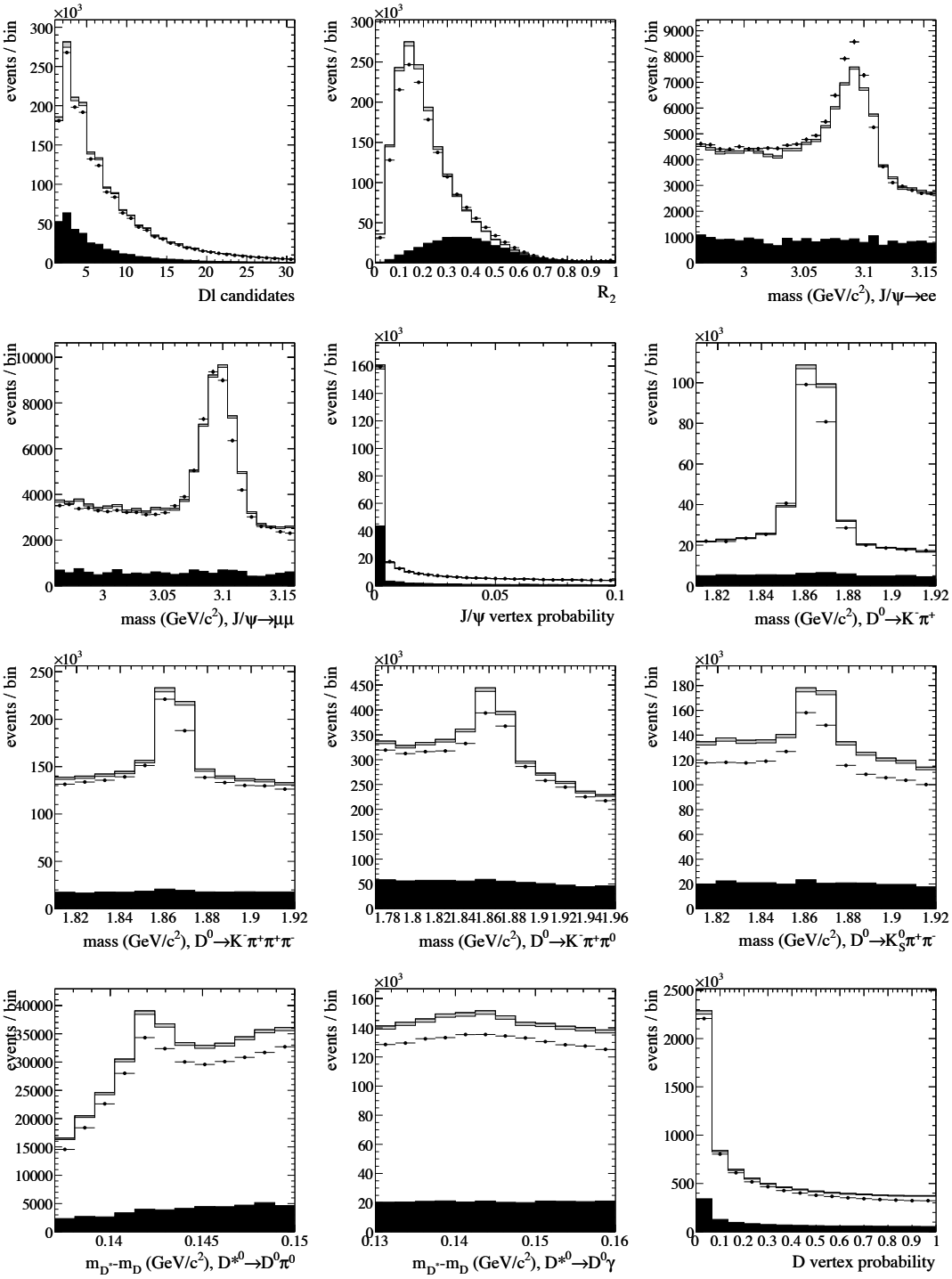

Figure 6.15: Analogous to Figure 6.8, for $\eta'\ell\nu$ channel.

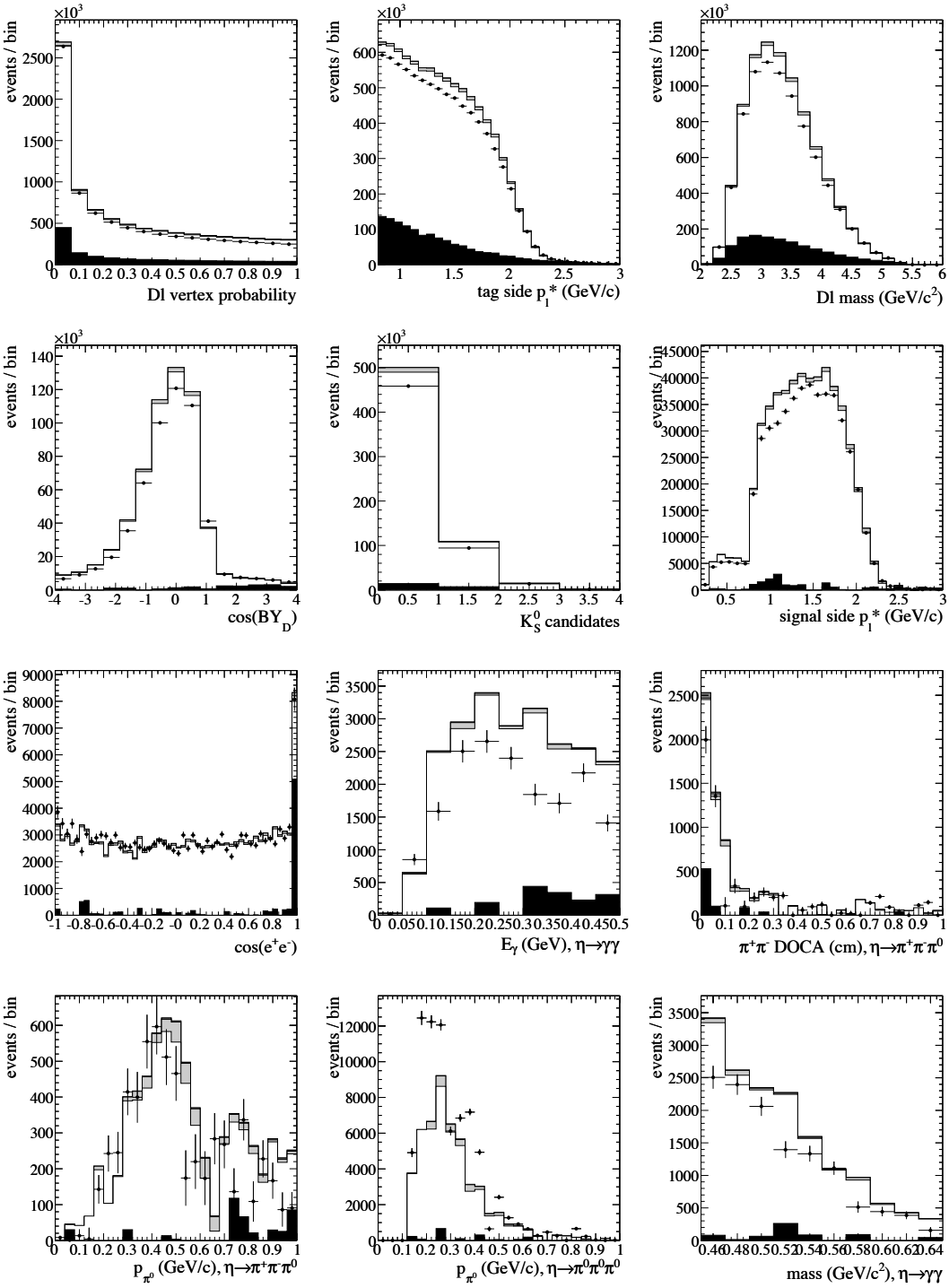

Figure 6.16: Continuation of Figure 6.15.

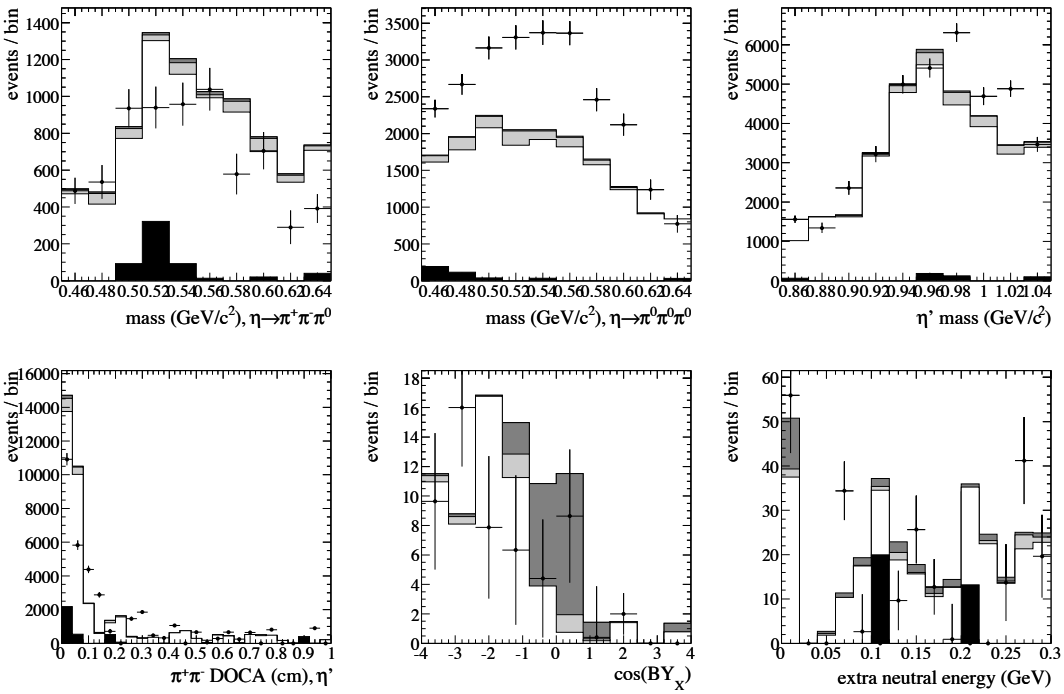

Figure 6.17: Continuation of Figure 6.16.

Chapter 7

Selection efficiency

The overall efficiency of the selection criteria discussed in §6 is described in Tables 7.1–7.4.

7.1 Squared momentum transfer

As partial branching fractions are measured in bins of the (signal side) squared momentum transfer q^2,[1] it is essential to understand signal reconstruction efficiencies as a function thereof. Where P_x are the four-momenta of x, it is defined

$$q^2 \equiv (P_\ell + P_\nu)^2, \tag{7.1}$$

but in practice, determined from the momentum of the final state charmless meson X:

$$q^2 \equiv (P_\ell + P_\nu)^2 = (\tilde{P}_B - P_X)^2, \tag{7.2}$$

where the B meson is approximated to be at rest.[2] The effect of this approximation is small; agreement between measured and true q^2 for each signal mode is shown in Figures 7.1–7.2. In principle, through knowledge of $\cos^2\phi_B$, the B direction is known up to twofold ambiguity; however, it does not improve the q^2 resolution significantly at the cost of correlating q^2 and $\cos^2\phi_B$.

To describe the efficiency of the selection criteria, as well as event migration between q^2

[1] See §8.

[2] Specifically, $\tilde{P}_B \equiv \left(\frac{m_{\Upsilon(4S)}}{2}, \vec{0}\right)$.

Table 7.1: Number of events surviving steps of selection described in §6 for the $\pi^{\pm}\ell\nu$ selection. All other samples are scaled to the size of the on-peak data. In only the "best candidate" (and subsequent) rows is D mass sideband subtraction is done.

	simulated data				data	
	$\pi^{\pm}\ell\nu$	other $X_u\ell\nu$	$B^0\overline{B}^0$	B^+B^-	off-peak	on-peak
preselected	410.8	5437.9	109511.8	84306.5	31182.2	223102.0
≤ 20 $D\ell$ candidates	410.3	5337.9	104573.0	78791.2	30239.9	212073.0
$R_2 \leq 0.5$	391.2	5229.9	103557.8	78055.9	23073.5	198010.0
$D\ell$ candidate	330.9	4293.1	85871.3	60929.3	15980.5	156779.0
$\lvert\cos(BY_D)\rvert \leq 5$	329.6	4251.4	84641.5	59923.3	15463.4	154185.0
no K_S^0	324.7	4078.5	77781.0	55618.8	13903.5	142844.0
$\cos(e^+e^-) \leq 0.995$	317.8	3953.1	72664.0	52698.3	10420.6	131436.0
no extra tracks	298.6	3121.3	58056.5	34300.9	7856.4	97180.0
$E^*_{\rm extra} \leq 140\,{\rm MeV}$	184.7	264.0	6164.2	1525.3	553.8	9307.0
$\lvert\cos(BY_X)\rvert \leq 5$	173.9	166.8	1865.2	512.3	253.4	3303.0
best candidate	145.3	92.2	1363.1	50.1	32.2	1719.5
$\cos^2\phi_B \leq 20$	141.2	74.3	757.4	21.8	37.9	990.8

Table 7.2: Analogous to Table 7.1, for $\pi^0\ell\nu$ channel.

	simulated data				data	
	$\pi^0\ell\nu$	other $X_u\ell\nu$	$B^0\overline{B}^0$	B^+B^-	off-peak	on-peak
preselected	479.8	5889.6	55301.5	113108.7	78715.1	258664.0
≤ 20 $D\ell$ candidates	479.3	5831.7	54172.9	110116.1	78214.9	253314.0
$R_2 \leq 0.5$	455.1	5700.6	53660.3	109081.8	59722.9	236171.0
$D\ell$ candidate	396.1	4818.3	41515.4	92207.1	40297.4	184377.0
$\lvert\cos(BY_D)\rvert \leq 5$	395.4	4791.9	40817.0	91423.4	39404.0	181889.0
no K_S^0	393.3	4661.1	38130.1	86690.7	38096.9	173116.0
$\cos(e^+e^-) \leq 0.995$	392.1	4643.7	37813.5	86243.0	27576.5	160044.0
no extra tracks	294.3	3741.1	29942.0	74035.2	14831.8	122944.0
π^0 candidate	199.2	1061.6	3096.8	11168.4	3262.4	18947.0
$E^*_{\text{extra}} \leq 70\,\text{MeV}$	132.3	145.3	281.0	764.0	381.4	1878.0
$\lvert\cos(BY_X)\rvert \leq 5$	131.7	130.2	212.2	540.4	327.2	1482.0
best candidate	103.3	34.4	34.1	242.1	-49.2	522.1
$\cos^2\phi_B \leq 20$	100.7	29.0	25.8	161.9	0.3	426.3

Table 7.3: Analogous to Table 7.2, for $\eta\ell\nu$ channel.

	simulated data				data	
	$\eta\ell\nu$	other $X_u\ell\nu$	$B^0\overline{B}^0$	B^+B^-	off-peak	on-peak
preselected	700.8	28367.6	387738.6	678017.8	272881.4	1321757.0
≤ 20 $n_{D\ell}$ candidates	694.9	27844.0	370681.5	644884.7	264875.3	1263731.0
$R_2 \leq 0.5$	665.9	27260.2	367176.0	638871.7	202627.7	1179112.0
$D\ell$ candidate	573.7	23315.5	293563.4	540364.2	151751.9	956804.0
$\lvert\cos(BY_D)\rvert \leq 5$	569.5	23089.8	286983.1	533051.9	147149.7	938754.0
no K_S^0	554.4	21608.8	252557.8	482328.9	131969.1	844599.0
$\cos(e^+e^-) \leq 0.995$	552.4	21490.4	249761.2	478326.4	96721.1	795940.0
no extra tracks	297.4	4727.5	51285.4	101705.0	18837.4	163880.0
η candidate	197.6	1847.0	16049.0	40389.1	8305.3	66399.0
$E^*_{\rm extra} \leq 70\,{\rm MeV}$	97.9	111.4	731.0	1390.8	452.4	3238.0
$\lvert\cos(BY_X)\rvert \leq 5$	95.5	77.2	285.8	554.0	363.9	1438.0
best candidate	75.0	22.7	34.4	177.5	15.3	322.1
$\cos^2\phi_B \leq 20$	73.2	17.7	24.2	115.7	4.0	202.3

Table 7.4: Analogous to Table 7.3, for $\eta'\ell\nu$ channel.

	simulated data				data	
	$\eta'\ell\nu$	other $X_u\ell\nu$	$B^0\overline{B}^0$	B^+B^-	off-peak	on-peak
preselected	593.2	32642.1	617880.3	867309.7	367419.8	1786437.0
≤ 20 $D\ell$ candidates	579.4	31542.4	569559.4	800142.5	345277.3	1651484.0
$R_2 \leq 0.5$	562.1	30917.1	564189.3	792694.2	263996.8	1540993.0
$D\ell$ candidate	483.7	26472.8	451040.6	660422.7	206760.7	1249970.0
$\lvert\cos(BY_D)\rvert \leq 5$	478.5	26125.5	438291.3	647804.7	198253.5	1217421.0
no K_S^0	445.1	23220.0	356340.5	549207.4	162008.5	1015488.0
$\cos(e^+e^-) \leq 0.995$	441.9	23059.7	351619.1	543272.3	117354.3	952162.0
no extra tracks	92.2	1260.8	20997.1	26118.9	4140.8	43680.0
η' candidate	36.1	104.1	1891.0	2227.7	325.5	3887.0
$E^*_{\text{extra}} \leq 70\,\text{MeV}$	19.5	6.1	77.4	101.9	0.0	207.0
$\lvert\cos(BY_X)\rvert \leq 5$	19.2	3.8	43.3	61.6	0.0	118.0
best candidate	14.4	1.3	9.5	27.7	0.0	47.2
$\cos^2\phi_B \leq 20$	14.3	2.0	6.9	19.3	0.0	26.1

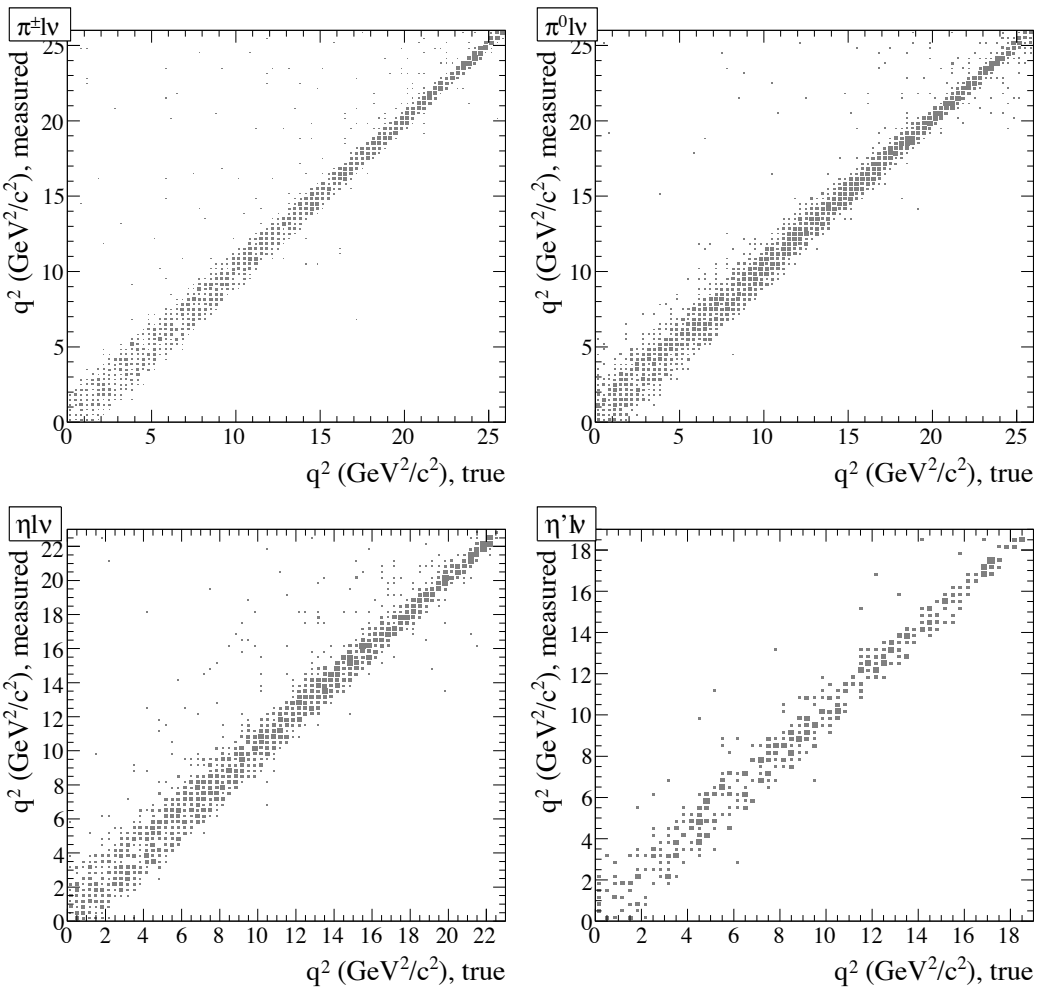

Figure 7.1: Reconstructed q^2 versus true q^2 for simulated signal events.

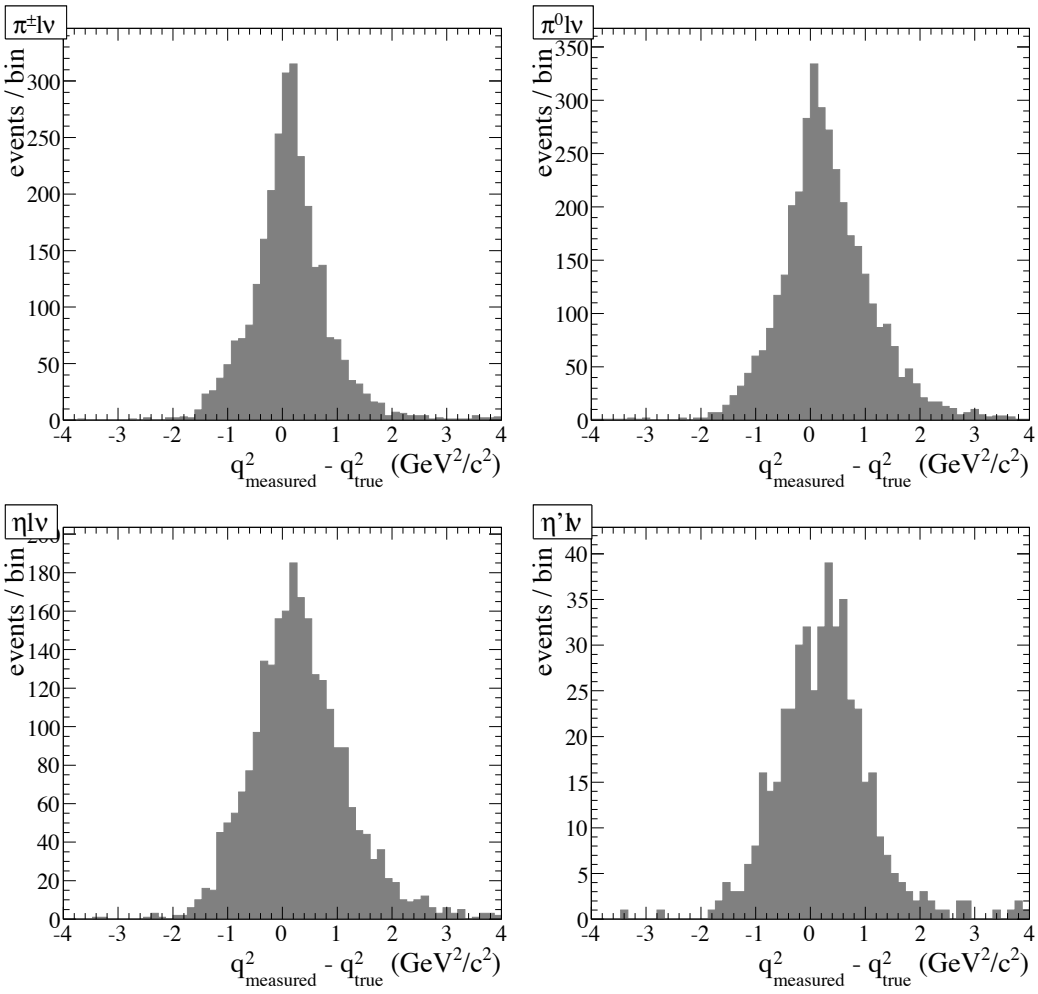

Figure 7.2: Resolution of q^2 reconstruction for simulated signal events.

bins, where N_i^{measured} is the number of events found with q^2 measured in the ith bin and N_j^{true} the number of events (total) with true q^2 in the jth bin, an efficiency and resolution matrix ε_{ij} is defined such that

$$N_i^{\text{measured}} = \varepsilon_{ij} N_j^{\text{true}}. \tag{7.3}$$

These matrices are determined from simulated signal data to be, for $B \to \pi^{\pm}\ell\nu$

$$\varepsilon_{ij} = \begin{pmatrix} 1.304 \pm 0.057 & 0.054 \pm 0.011 & 0.003 \pm 0.003 \\ 0.084 \pm 0.015 & 1.284 \pm 0.055 & 0.000 \pm 0.007 \\ 0.015 \pm 0.007 & 0.056 \pm 0.013 & 1.408 \pm 0.056 \end{pmatrix} \text{‰}, \tag{7.4}$$

for $B \to \pi^0\ell\nu$

$$\varepsilon_{ij} = \begin{pmatrix} 1.787 \pm 0.069 & 0.044 \pm 0.011 & 0.000 \pm 0.000 \\ 0.162 \pm 0.021 & 1.733 \pm 0.066 & 0.033 \pm 0.010 \\ 0.000 \pm 0.002 & 0.083 \pm 0.015 & 1.413 \pm 0.058 \end{pmatrix} \text{‰}, \tag{7.5}$$

for $B \to \eta\ell\nu$

$$\varepsilon_{ij} = \begin{pmatrix} 1.122 \pm 0.050 & 0.035 \pm 0.009 & 0.000 \pm 0.000 \\ 0.105 \pm 0.016 & 1.050 \pm 0.048 & 0.036 \pm 0.012 \\ 0.005 \pm 0.003 & 0.084 \pm 0.014 & 0.880 \pm 0.054 \end{pmatrix} \text{‰} \tag{7.6}$$

and for $B \to \eta'\ell\nu$,

$$\varepsilon_{ij} = \begin{pmatrix} 0.224 \pm 0.015 & 0.001 \pm 0.001 \\ 0.003 \pm 0.003 & 0.157 \pm 0.032 \end{pmatrix} \text{‰}, \tag{7.7}$$

where the bins are defined as $q^2 < 8$, $8 \leq q^2 < 16$ and $q^2 \geq 16$ GeV$^2/c^2$ ($q^2 < 16$ and $q^2 \geq 16$ GeV$^2/c^2$) for $\pi^{\pm}\ell\nu$, $\pi^0\ell\nu$ and $\eta\ell\nu$ ($\eta'\ell\nu$). Overall efficiencies are 1.40 ± 0.03‰, 1.76 ± 0.04‰, 1.14 ± 0.03‰ and 0.22 ± 0.02‰ for $\pi^{\pm}\ell\nu$, $\pi^0\ell\nu$, $\eta\ell\nu$ and $\eta'\ell\nu$ signal modes respectively.

7.2 Double tags

The $D\ell$ tagging efficiency is known to be different in data and simulated data. The $D\ell$ tagging efficiency in data is studied via "double tag" events—events with two $D\ell$ tags, i.e., events reconstructed as $B\overline{B}$ pairs with both B mesons decaying semileptonically to $D\ell\nu$—and

Table 7.5: Number of good tag events found in simulated $B\overline{B}$ data ($N_{\rm MC}$) and on-peak data ($N_{\rm data}$), separately for $B^0\overline{B}^0$ and B^+B^- double tags; $N_{\rm data}$ is derived from the unbinned maximum likelihood fits shown in Figure 7.3.

	$B^0\overline{B}^0$	B^+B^-
$N_{\rm MC}$	2182.4	7945.5
$N_{\rm data}$	2075 ± 64	7917 ± 89

compared to that found in simulation. Where $N_{\rm data}$ ($N_{\rm MC}$) is the number of double tag events found in data (simulated data), with the assumption that the tagging efficiency for each B decay is independent of the other, a data-simulation correction factor

$$r_\varepsilon = \sqrt{\frac{N_{\rm data}}{N_{\rm MC}}} \tag{7.8}$$

is derived for the (single) tag efficiency.

The double tag study is done using events with two non-overlapping and charge-compatible $D\ell$ tags satisfying requirements through §6.3.1. The same track and photon quality requirements as in the primary analysis are imposed, as well as the nonexistence of additional tracks found in the event (cp. §6.3.2). Twice as much extra neutral energy in double tag events as in $X\ell\nu$ events,[3] i.e., 140 MeV for B^+B^- double tags and 280 MeV for $B^0\overline{B}^0$ double tags, is allowed.

For events with multiple double tag pairs passing all selection criteria, the pair with the smallest $|\cos(BY)|$ product is chosen as the "best" candidate. Peak and sideband D mass regions are defined as in §6.3.1 and are applied independently, i.e., if one D candidate has a mass within the sideband region (but the other's is in the peak window), the event receives the appropriate (negative) sideband weight; when both D candidates have masses within the sideband region, the sideband weights are multiplied.

A double tag event in simulated data is considered to be a "good" tag if, for both of its tags, the reconstructed $D^{0,\pm}$ candidate matches a true $D^{0,\pm}$ meson, the lepton candidate matches a true lepton, and the true D meson and lepton originate from the same B meson,[4]

[3]This takes the ansatz that the extra neutral energy comes from the tag side.

[4]In actuality, it is not important that the tag be correctly reconstructed per se, only that it is "correct enough" that it would be tagged in the recoil of a $B \to X\ell\nu$ decay. This definition of "good" tag, to first order, excludes tags in which particles originating from a B meson are matched with particles coming from the other, which, due to the lower multiplicity of the

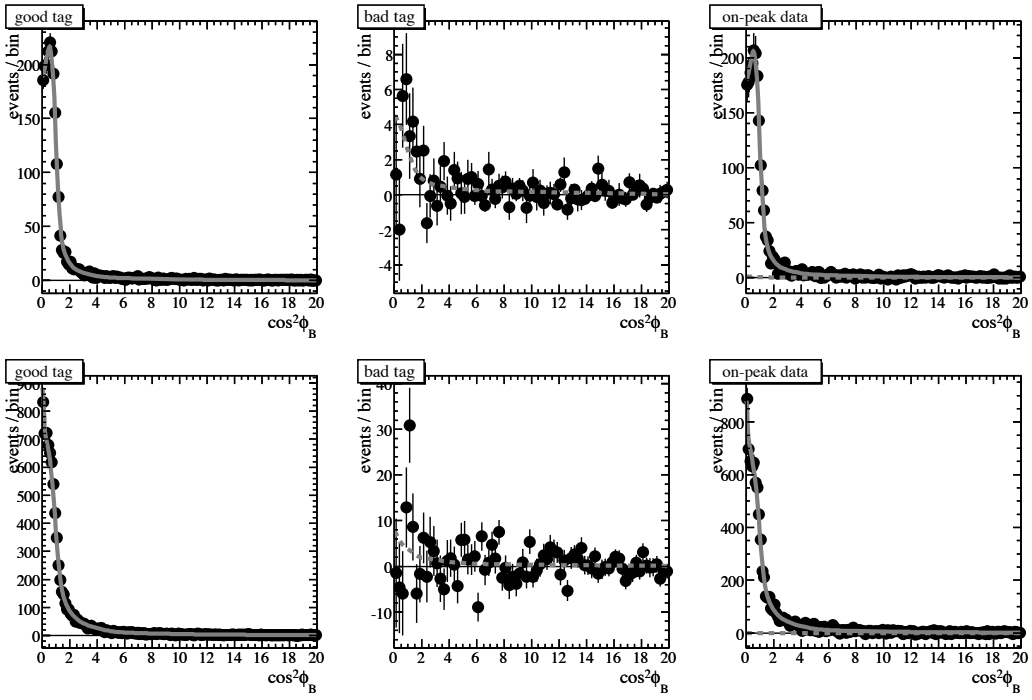

Figure 7.3: Distributions of $\cos^2\phi_B$ found in $B^0\overline{B}^0$ (top) and B^+B^- (bottom) double tag events for good (left) and bad (center) tags; curves show derived probability density functions. On-peak data (right) is shown with the probability density function from a yield fit to these two components overlaid, along with the bad tag contribution (dashed).

which gives $N_{\rm MC}$. All other double tags are considered to be "bad"; the (good tag) yield, i.e., $N_{\rm data}$, of the data is determined by unbinned maximum likelihood fit[5] on $\cos^2\phi_B$ to these two components,[6] shown in Figure 7.3 and Table 7.5.

This leads to the corrections

$$r_\varepsilon = 0.973 \pm 0.015 \tag{7.9}$$

for $B^0\overline{B}^0$, and

$$r_\varepsilon = 0.998 \pm 0.006 \tag{7.10}$$

for B^+B^-, where the listed uncertainties are statistical. This corrects for differences in tagging efficiency, including tag side branching fractions, reconstruction, resolution, etc. Systematic uncertainties associated with this double tag study are discussed in §9.3.

charmless signal modes, are a small component of the single tag efficiency. The opposite extreme would be to consider all double tags "good" and derive r_ε simply from the ratio of double tags in data versus simulated data; because the double tag samples are quite pure (as can be seen in Figure 7.3), this alternate method yields a correction factor with negligible difference.

[5]Input probability density functions are derived from simulated data with parameter-free kernels [43].

[6]Both are constrained to be nonnegative; when errors are asymmetric, the larger is taken (symmetrically).

Chapter 8

Yield extraction

Signal yields are determined via a fit on $x \equiv \cos^2 \phi_B$ in the range $0 \leq x < 20$, separately for each signal mode and q^2 bin.

Four mutually exclusive subsets of the data passing the selection criteria are considered.

- "Signal" (sig) events are simulated events generated with a B meson decaying in the appropriate signal mode. The $D^{0,\pm}$ meson in each event is required to have been correctly reconstructed, with a mass measured to be within the D mass peak window.
- "Background" (bg) events are all other $B\overline{B}$ events, including crossfeed from other charmless semileptonic decays, wherein, as in the signal case, the tag side D meson has been correctly reconstructed, with a mass measured to be in the D mass peak window.
- "Combinatoric" (cmb) events are (on-peak) data events with a $D^{0,\pm}$ candidate measured to have a mass in the D mass sideband region.
- "Peak" (pk) events are (on-peak) data events such that the $D^{0,\pm}$ candidate is measured to have a mass in the D mass peak region.

Probability density functions $\mathcal{P}_k$ for the first three samples are modeled, up to normalization, with analytic functions with free paramters P_i.

- The signal probability density function (PDF) is given as a threshold function in the physical region ($0 \leq x \leq 1$) with finite resolution and an exponential tail:

$$\mathcal{P}_{\text{sig}}(x) \propto \frac{1 - \text{erf}(P_0 \log(P_1 x))}{2} + P_2 \exp(-P_3 x). \tag{8.1}$$

- The background PDF is parameterized as an exponential with a nonnegative constant term:

$$\mathcal{P}_{\rm bg}(x) \propto \exp(P_4 x) + P_5^2. \tag{8.2}$$

- The combinatoric PDF is parameterized as the absolute value of a quadratic,[1] with two parameters P_6 and P_7.

The $\mathcal{P}_k$ are normalized such that each integrates over the fit range to unity.

The peak sample is an admixture of events described by the other three; where the respective yields are N_k, its x distribution is

$$\frac{dN_{\rm pk}}{dx} = \sum_{\substack{k={\rm sig},\\ {\rm bg,cmb}}} N_k \mathcal{P}_k(x). \tag{8.3}$$

These four samples and four distributions are used in a simultaneous, unbinned fit maximizing the likelihood

$$\begin{aligned} L(N_{\rm sig}, N_{\rm bg}, N_{\rm cmb}, \vec{P}) = \frac{e^{-(N_{\rm sig}+N_{\rm bg}+N_{\rm cmb})}}{\tilde{N}_{\rm pk}!} \prod_{i=1}^{\tilde{N}_{\rm pk}} \left(\sum_{\substack{k={\rm sig},\\ {\rm bg,cmb}}} N_k \mathcal{P}_k(x_i) \right) \\ \times \prod_{i=1}^{\tilde{N}_{\rm sig}} w_i \mathcal{P}_{\rm sig}(x_i) \times \prod_{i=1}^{\tilde{N}_{\rm bg}} w_i \mathcal{P}_{\rm bg}(x_i) \times \frac{e^{-N_{\rm cmb}}}{\tilde{N}_{\rm cmb}!} \prod_{i=1}^{\tilde{N}_{\rm cmb}} w_i \mathcal{P}_{\rm cmb}(x_i) \end{aligned} \tag{8.4}$$

where $\tilde{N}_k$ is the size of the sample k, $\vec{P} \equiv (P_0, P_1, \ldots, P_7)$ is the PDF parameters and w_i is the weight associated with a given event, normalized such that the sum of w_i^2 over all N events is N^2. The combinatoric yield ($N_{\rm cmb}$) is constrained by $\tilde{N}_{\rm cmb}$, the number of measured combinatoric events.

8.1 Exception for $\eta'\ell\nu$, $q^2 \geq 16$ GeV$^2/c^2$

For the $\eta'\ell\nu$ signal mode, knowledge of the signal yield in the $q^2 \geq 16$ GeV$^2/c^2$ "bin" is required for the inference, using Equations 7.3 and 7.7, of the number of $\eta'\ell\nu$ signal events with true q^2 less than 16 GeV$^2/c^2$ from the number of events with measured q^2 less than 16 GeV$^2/c^2$. However, too few events in this bin pass all $\eta'\ell\nu$ selection criteria for the signal

[1] This is implemented via Chebyshev polynomials: $\mathcal{P}_{\rm cmb}(x) \propto 1 + P_6\tilde{x} + P_7(2\tilde{x}^2 - 1)$, where $\tilde{x}$ is x after a linear transformation of the fit range onto the range $-1 \leq \tilde{x} < 1$.

yield to be reliably extracted via fit; instead, the yield is taken simply to be the number of on-peak data events (after the subtraction of the expected combinatoric $D^{0,\pm}$ contribution, as inferred from the abundance of events in the D mass sideband region) found in the signal ($\cos^2\phi_B < 1.5$) region: 1, i.e., the lone event found is assumed to be signal, but with a 100% statistical uncertainty.

8.2 Validation

The fit method has been tested on several sets of simulated data, including admixtures of the sets described in §5.2 and other available *BABAR* data sets containing (known amounts of) signal events, and has been determined to extract yield correctly up to statistical accuracy.

Furthermore, the fit is determined to be unbiased, with accurate assessment of uncertainty, by the following procedure:

1. The fit is performed using, in place of the peak sample, a toy sample that is simply the sum of the signal, background and combinatoric samples. Base parameter values $\langle P_i \rangle$ are taken to be the results of this fit.

2. Expected values for the yields $\langle N_{\rm sig} \rangle$ and $\langle N_{\rm bg} \rangle$ are taken from simulated data using parameters given in §5.2.1. The expected yield for the combinatoric sample $\langle N_{\rm cmb} \rangle$ (or $\langle \tilde{N}_{\rm cmb} \rangle$, which is manifestly equal) is taken directly from the size of the sideband sample.

3. "Toy" signal and background samples are randomly generated using the $\langle P_i \rangle$. The sizes of these are taken to be the size of the original signal and background samples (and are irrelevant to this procedure).

4. A toy combinatoric sample is generated using the $\langle P_i \rangle$. The size of this sample is randomized as a Poisson variable around $\langle \tilde{N}_{\rm cmb} \rangle$.[2]

5. A toy peak sample is generated as the sum of new toy signal, background and combinatoric samples,[3] the relative contributions of which are randomized as Poisson variables around the $\langle N_k \rangle$.

[2]This Poisson variable is thrown to reflect the statistical uncertainty associated with the size of sideband sample before events are weighted for the width of the D mass peak window.

[3]They are generated analogously to those generated in #3–4, but are statistically independent.

Table 8.1: Fit results for signal yield (N_k) for each signal mode and q^2 bin. Uncertainties are entirely statistical.

	$q^2 < 8$	$8 \leq q^2 < 16$	$q^2 > 16$ GeV$^2/c^2$
$\pi\ell\nu$	61.8 ± 11.8	37.8 ± 10.7	50.4 ± 14.7
$\pi^0\ell\nu$	63.9 ± 12.9	43.0 ± 10.7	27.1 ± 10.0
$\eta\ell\nu$	25.7 ± 8.5	14.9 ± 9.0	14.7 ± 8.6

	$q^2 < 16$	all q^2
$\eta'\ell\nu$	-0.88 ± 3.9	0.64 ± 3.9

6. The fit is performed with the four toy samples generated in steps 3-5. Where this fit measures N_k and corresponding uncertainties σ_{N_k}, the pull of N_k for this fit is

$$\text{pull}(N_k) = \frac{N_k - \langle N_k \rangle}{\sigma_{N_k}}. \tag{8.5}$$

7. For each signal mode and q^2 bin, #3–6 are repeated two hundred times.

Figures 8.1–8.4 show distributions for the pulls of each yield in each signal mode and q^2 bin. Each shows good agreement, up to statistics, with a mean of zero and standard deviation of unity, as desired.

8.3 Fit result

Fit results for the signal yields (N_k) are listed in Table 8.1; PDFs and data are shown in Figures 8.5-8.15.

8.3.1 A note on $B^+ \to \eta'\ell^+\nu$

To minimize potential experimenter bias, the event and candidate selection criteria and yield extraction method were developed "blind," i.e., using only simulated data. Although $B^+ \to \eta'\ell^+\nu$ branching fractions are ultimately measured to be consistent with zero, in the hypothetical case in which $\mathcal{B}(B^+ \to \eta'\ell^+\nu)$ is equal to the accepted value of $\mathcal{B}(B^+ \to \eta\ell^+\nu)$,[4] $B^+ \to \eta'\ell^+\nu$ branching fractions would have been measured with (total, including systematic uncertainties) significances of 3.1σ for $q^2 < 16$ GeV$^2/c^2$ and 2.8σ over the full q^2 range.

[4] See Table 5.2.

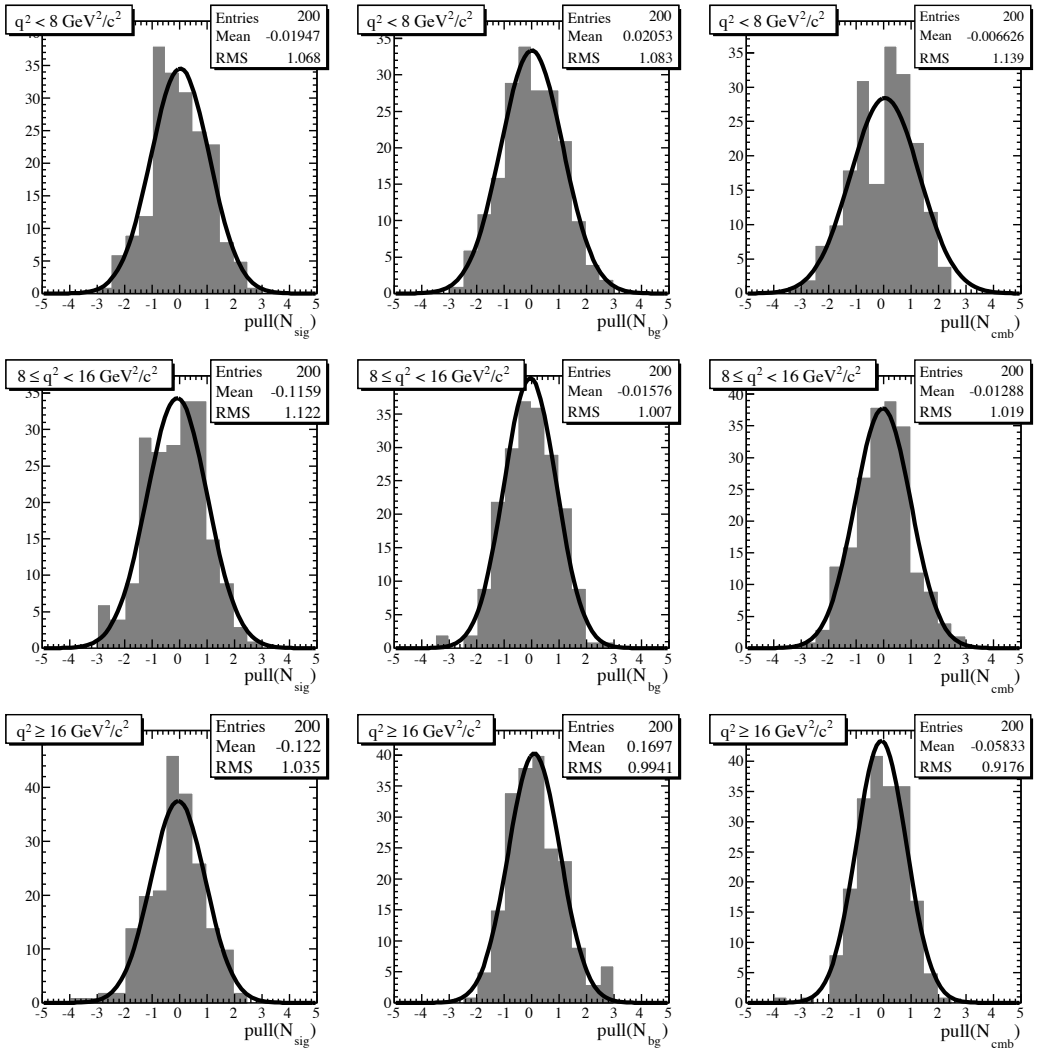

Figure 8.1: Pull distribution of signal (left), background (middle) and combinatoric (right) yields for two hundred test fits performed in the $\pi^{\pm}\ell\nu$ signal mode, in the low (top), intermediate (middle) and high (bottom) q^2 bins. Each is fit to a normal distribution.

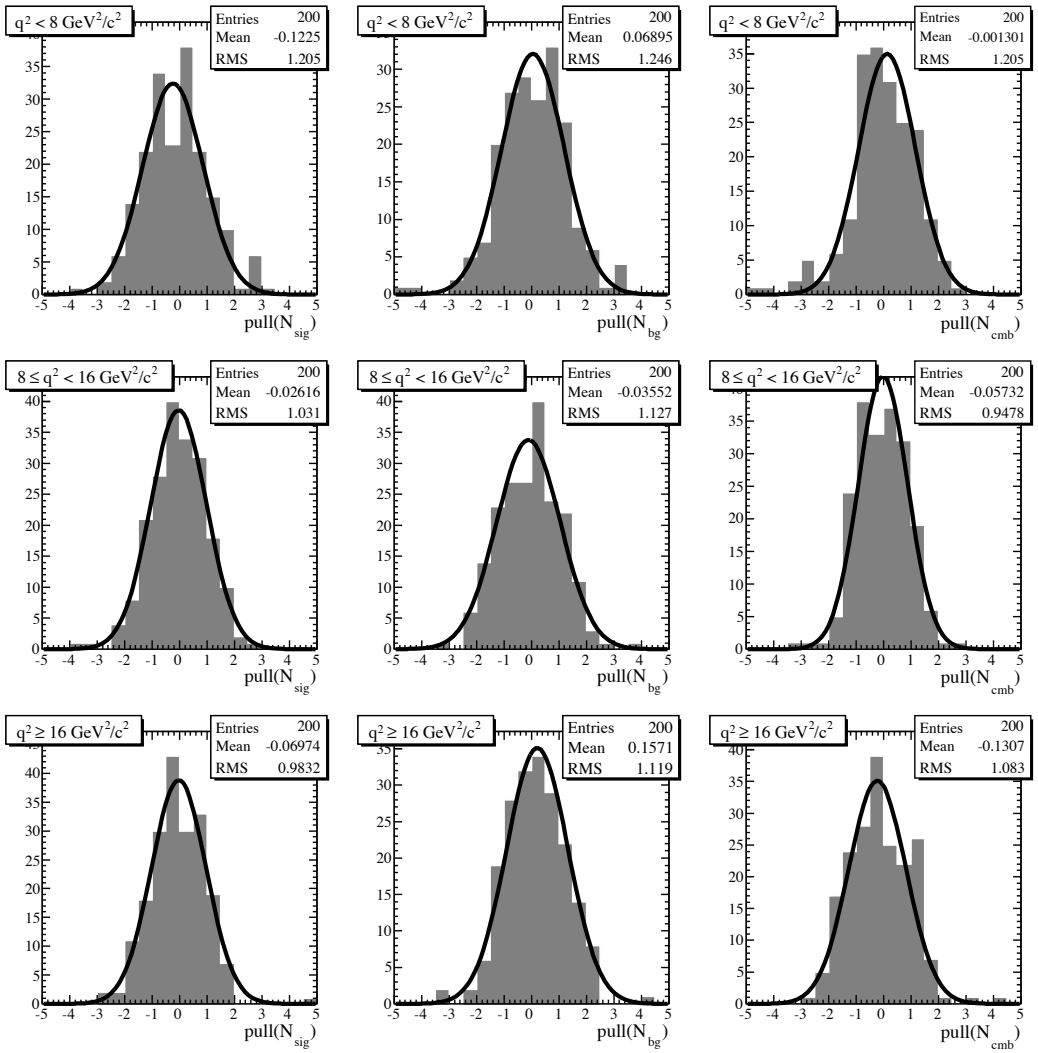

Figure 8.2: Analogous to Figure 8.1, for $\pi^0 \ell \nu$ signal mode.

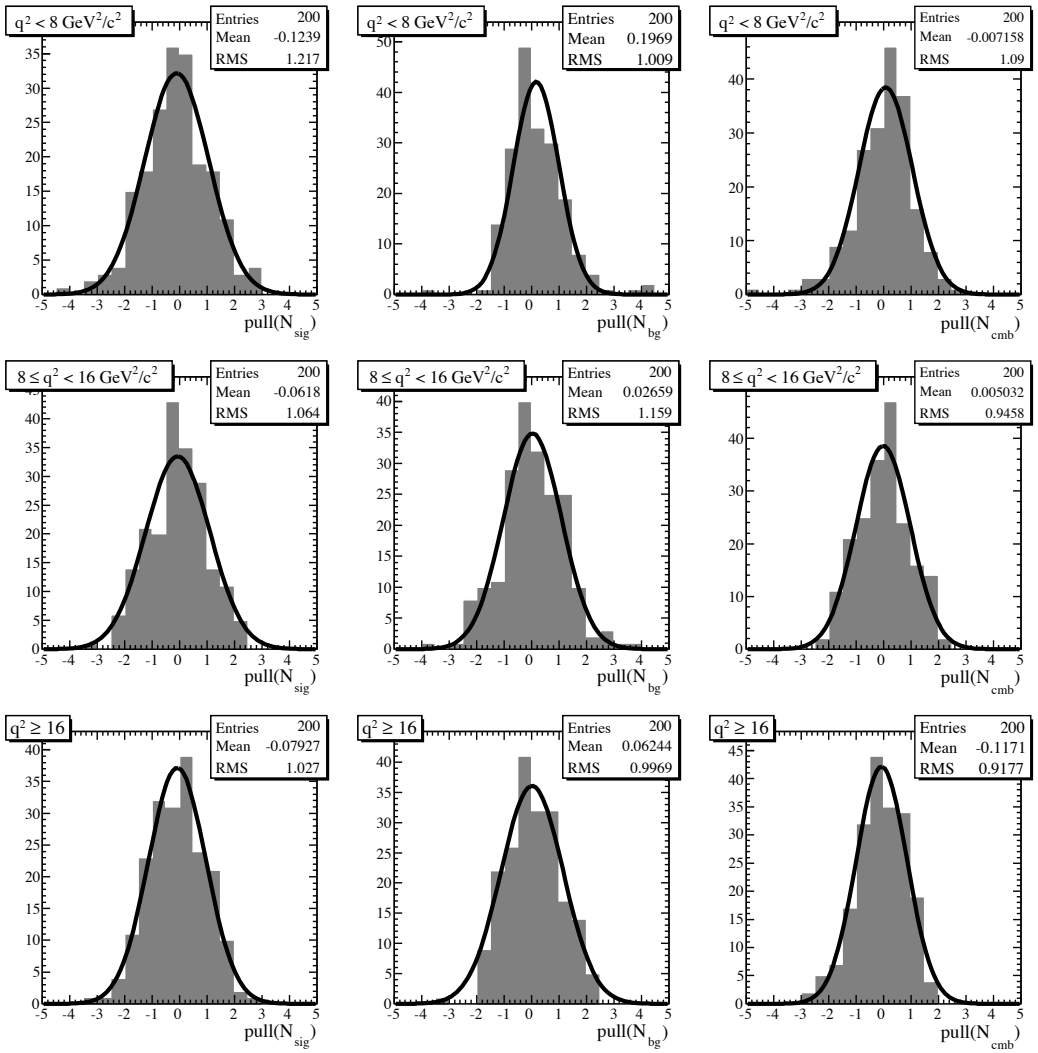

Figure 8.3: Analogous to Figure 8.2, for $\eta\ell\nu$ signal mode.

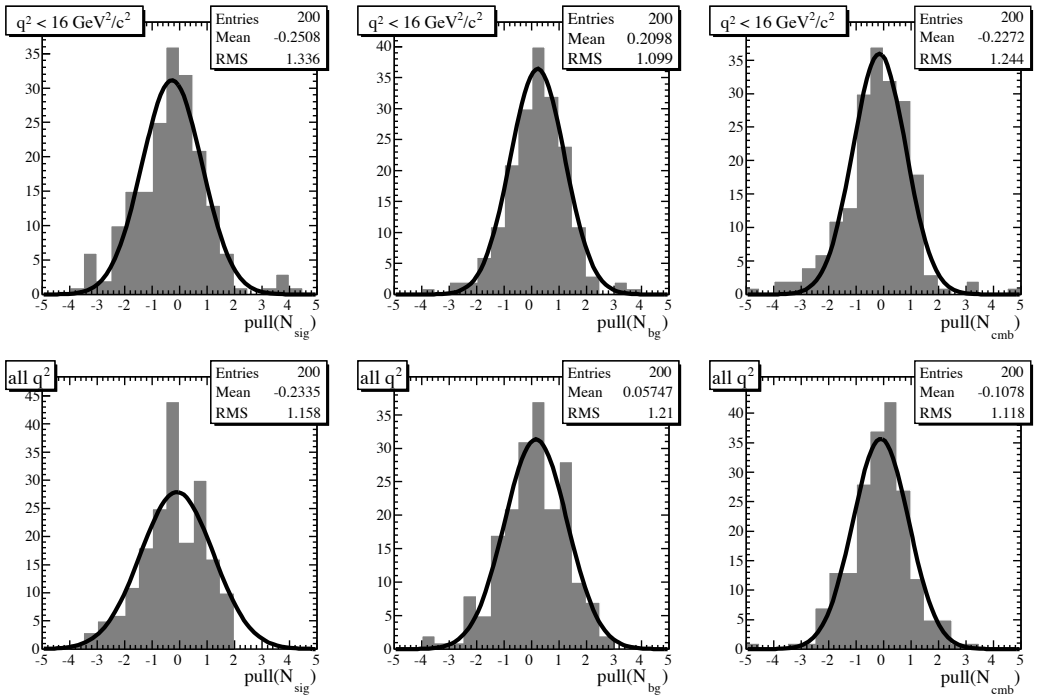

Figure 8.4: Analogous to Figure 8.3, for $\eta'\ell\nu$ signal mode, for $q^2 < 16$ GeV$^2/c^2$ bin (top) and full q^2 range (bottom).

8.4 Determination of branching fractions

For each signal mode, in the jth q^2 bin, $N_j^{\rm true}$ events are inferred, where, per §7.1–7.2,

$$N_j^{\rm true} = r_\varepsilon (\varepsilon^{-1})_{ji} N_i^{\rm measured}, \tag{8.6}$$

with $N_i^{\rm measured}$ given in Table 8.1, ε in Equations 7.4–7.7 and r_ε in Equations 7.9–7.10. This is related to the appropriate partial branching fraction over the given q^2 range by

$$2 \times \Delta\mathcal{B} = \frac{N_j^{\rm true}}{2 f_{00} N_{B\overline{B}}} \tag{8.7}$$

for $B^0 \to \pi^-\ell^+\nu$, where f_{00} is the $B^0\overline{B}^0$ fraction, $N_{B\overline{B}}$ the number of $B\overline{B}$ pairs recorded[5] and thus $2f_{00}N_{B\overline{B}}$ the number of B^0 mesons. The 2 on the left accounts for $B^0 \to \pi^- e^+\nu$ and $B^0 \to \pi^-\mu^+\nu$. Analogously,

$$2 \times \Delta\mathcal{B} = \frac{N_j^{\rm true}}{2(1 - f_{00}) N_{B\overline{B}}} \tag{8.8}$$

[5]See Table 5.1.

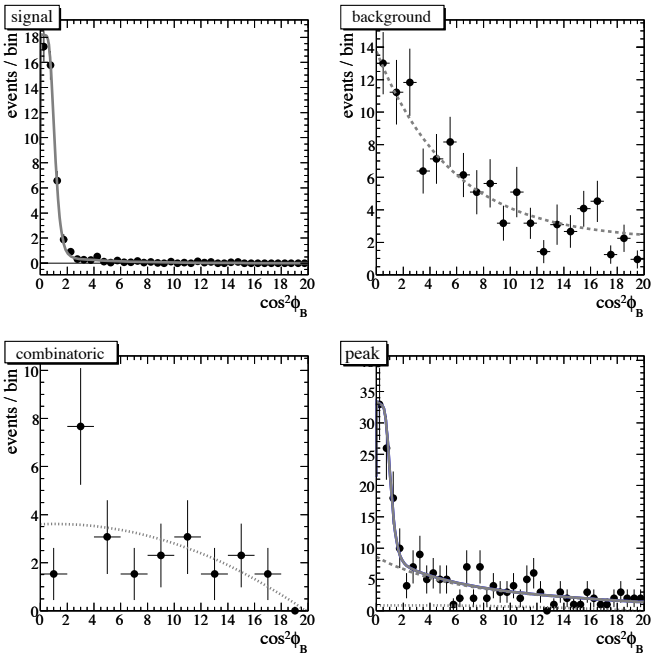

Figure 8.5: PDFs obtained from fit for $\pi^{\pm}\ell\nu$ signal mode in the $q^2 < 8$ GeV$^2/c^2$ bin, for signal (solid), background (dashed) and combinatoric (dotted). The peak sample is simultaneously fit to the sum of these, which are shown stacked in the SE plot.

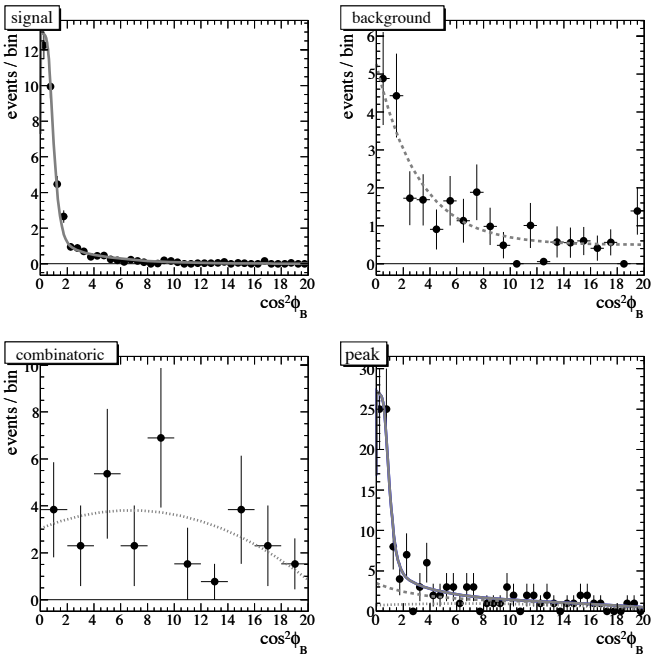

Figure 8.6: Analogous to Figure 8.5, for $\pi^0\ell\nu$ signal mode, $q^2 < 8$ GeV$^2/c^2$ bin.

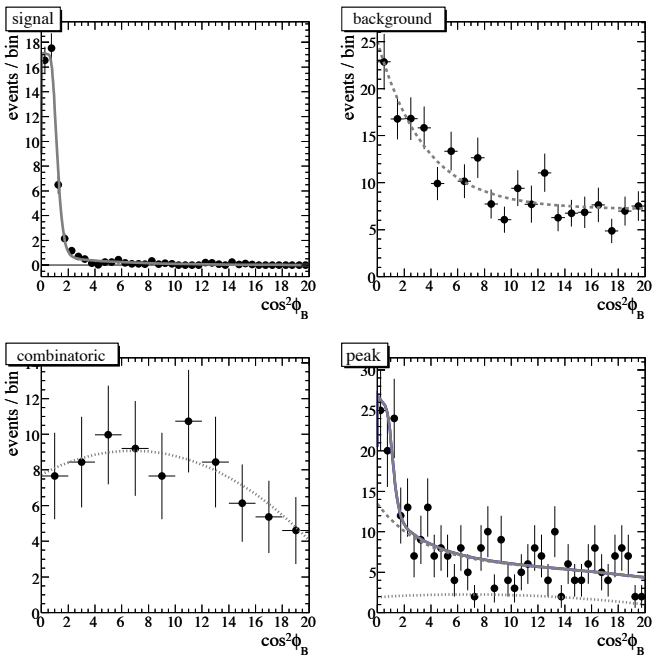

Figure 8.7: Analogous to Figure 8.13, for $\pi\ell\nu$ signal mode, $8 \leq q^2 < 16$ GeV$^2/c^2$ bin.

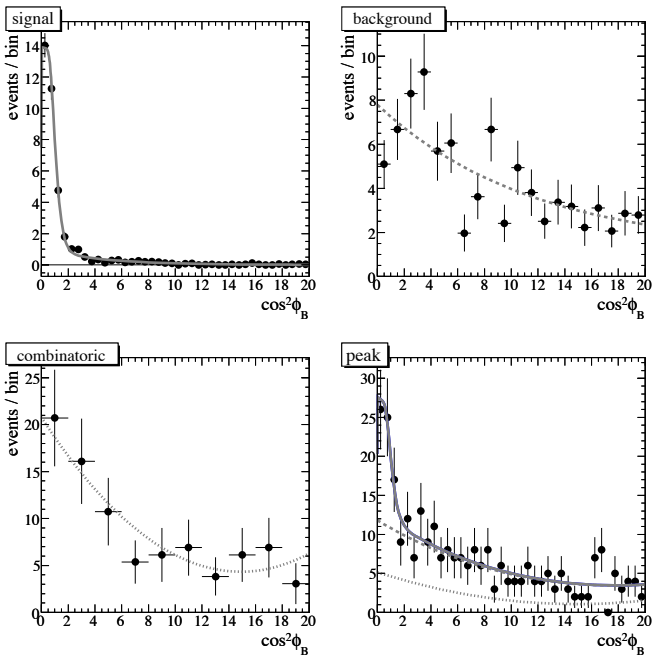

Figure 8.8: Analogous to Figure 8.10, for $\pi^0\ell\nu$ signal mode, $8 \leq q^2 < 16$ GeV$^2/c^2$ bin.

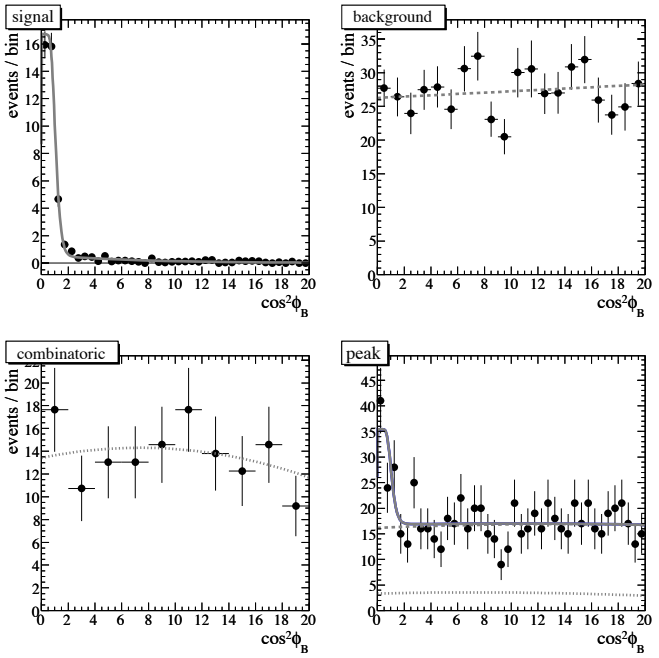

Figure 8.9: Analogous to Figure 8.6, for $\pi\ell\nu$ signal mode, $q^2 \geq 16$ GeV$^2/c^2$ bin.

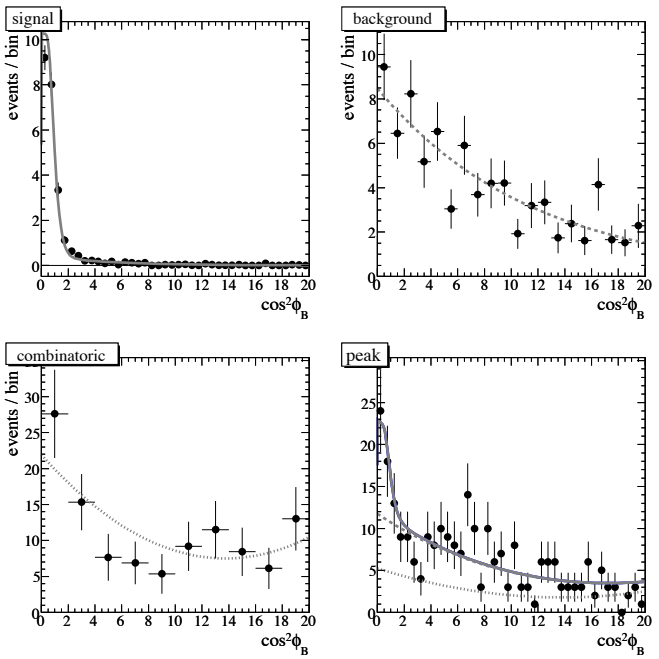

Figure 8.10: Analogous to Figure 8.14, for $\pi^0\ell\nu$ signal mode, $q^2 \geq 16$ GeV$^2/c^2$ bin.

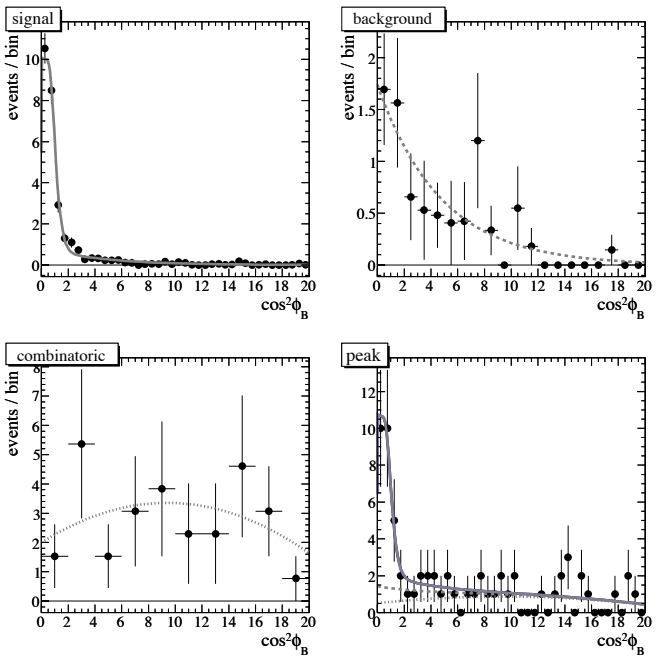

Figure 8.11: Analogous to Figure 8.15, for $\eta\ell\nu$ signal mode, $q^2 < 8$ GeV$^2/c^2$ bin.

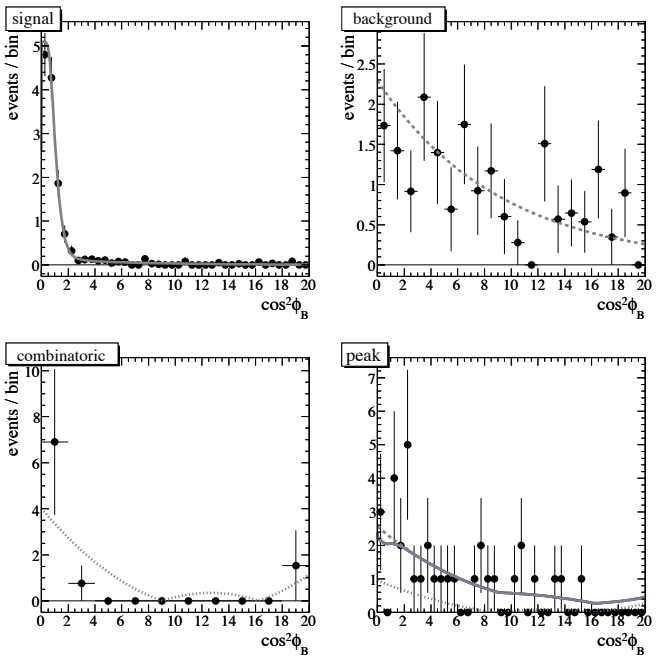

Figure 8.12: Analogous to Figure 8.7, for $\eta'\ell\nu$ signal mode, $q^2 < 16$ GeV$^2/c^2$ bin.

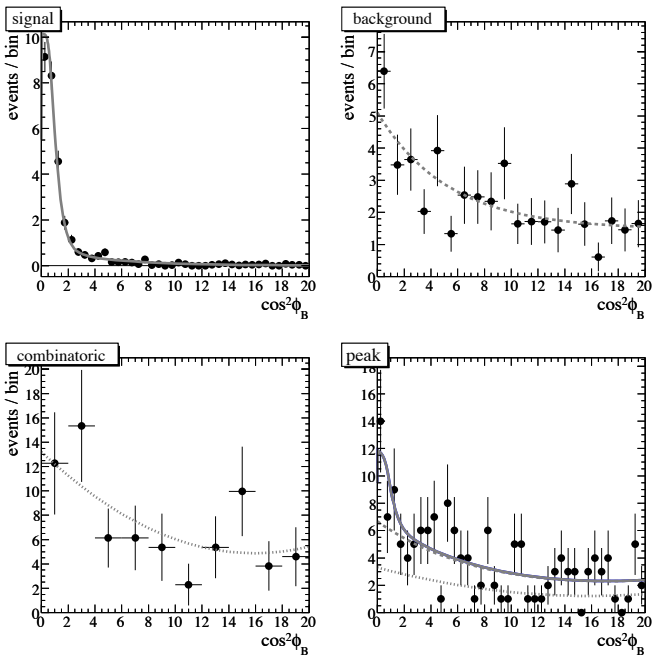

Figure 8.13: Analogous to Figure 8.9, for $\eta\ell\nu$ signal mode, $8 \leq q^2 < 16$ GeV$^2/c^2$ bin.

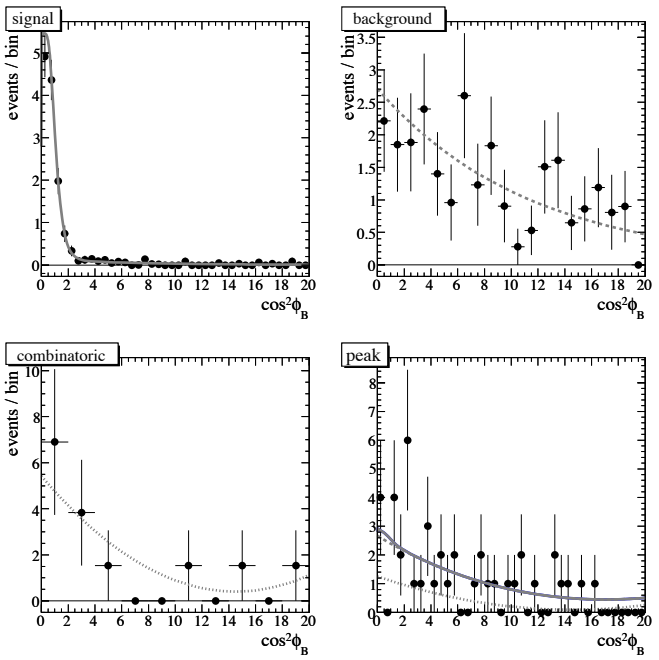

Figure 8.14: Analogous to Figure 8.12, for $\eta'\ell\nu$ signal mode, full q^2 range.

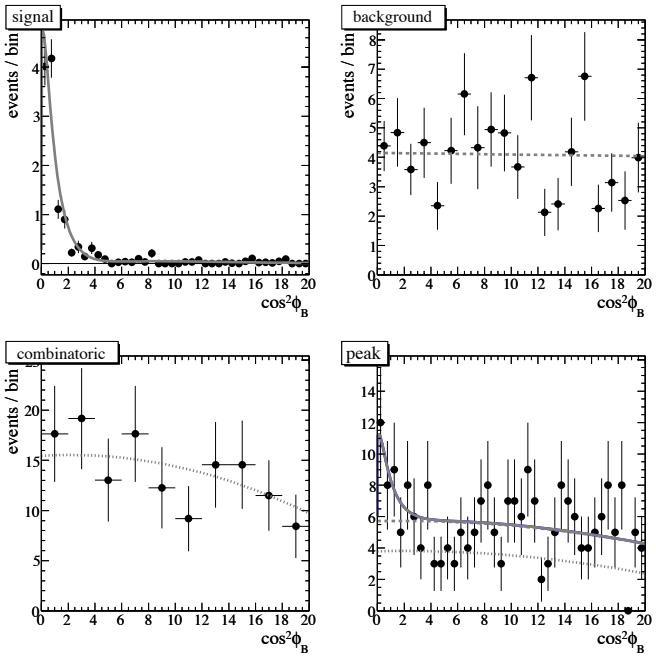

Figure 8.15: Analogous to Figure 8.8, for $\eta\ell\nu$ signal mode, $q^2 \geq 16$ GeV$^2/c^2$ bin.

for the $B^{\pm}$ decay modes.

For $\pi^{\pm}\ell\nu$, $\pi^0\ell\nu$ and $\eta\ell\nu$ modes, total branching fractions and $q^2 < 16$ GeV$^2/c^2$ partial branching fractions are determined from these partial branching fractions (rather than, e.g., from the signal yield over the combined bins and an aggregate efficiency) to lessen sensitivity to decay kinematics, and to simplify the evaluation of systematic uncertainties.[6]

[6]The slight statistical cost is a greater statistical uncertainty on the efficiency and that, for example, the statistical uncertainty on a $q^2 \leq 16$ GeV$^2/c^2$ branching fraction contains contributions from bin migration in both directions between the two constituent bins.

Chapter 9

Systematic uncertainties

The uncertainties on the branching fraction measurements are summarized in Tables 9.1–9.4. The stated statistical uncertainty from yield extraction accounts for finite statistics of both data and simulated data sets; also included are statistical uncertainties on the efficiencies due to finite statistics of the simulated signal data as in Equations 7.4–7.7 and statistical uncertainties on the double tag correction factors due to the finiteness the samples used in the double tag study, as listed in Equations 7.9–7.10.[1]

The systematic components of the uncertainty are explained below.

9.1 Modeling of physics processes

Simulated data, which are used extensively in these measurements, can be accurate only insofar as underlying physics processes are understood.

9.1.1 Charmless semileptonic decay

To demonstrate that the results of these measurements are not heavily sensitive to the specifics of charmless semileptonic B meson decays as modeled in the simulated data, the measurements

[1]The breakdown of the statistical uncertainty in Tables 9.1-9.4 is simplified for illustrative purposes. The listed uncertainties due to "yield" are uncertainties on the N_i^{measured}, not the N_j^{true}; in actuality, for a given signal mode, uncertainties on all N_i^{measured} contribute to the uncertainty on a given N_j^{true}, as suggested by Equation 7.3. The listed "efficiency" uncertainties are an approximation back-calculated from the true total statistical uncertainty (as calculated by Equation 7.3) assuming that the efficiency matrices (Equations 7.4-7.7) are diagonal, which is true to first order and useful in showing the size of the true contribution of the efficiency uncertainty to the total uncertainty.

Table 9.1: Summary of (fractional) uncertainties on branching fraction measurements for $B \to \pi^{\pm}\ell\nu$, in low ($q^2 < 8$), middle ($8 \leq q^2 < 16$), high ($q^2 \geq 16$), "low+mid" ($q^2 < 16$ GeV$^2/c^2$) bins and total (all q^2). All values are given in percent.

q^2 **bin**	**low**	**middle**	**high**	**low+mid**	**total**
yield	± 20	± 32	± 29	± 17	± 15
efficiency	± 4.6	± 5.4	± 4.0	± 3.3	± 2.6
double tag statistics	± 1.5				
total statistical	$\pm$**21**	$\pm$**33**	$\pm$**30**	$\pm$**18**	$\pm$**16**
$B \to \{\rho, \omega\}\ell\nu$ BF	$^{+0.24}_{-0.37}$	$^{+1.6}_{-0.95}$	$^{+0.18}_{-0.15}$	$^{+0.72}_{-0.58}$	$^{+0.54}_{-0.44}$
$B \to \eta\ell\nu$ BF	$^{+0}_{-0.070}$	$^{+0.0075}_{-0.00079}$	$^{+0.0086}_{-0.022}$	$^{+0}_{-0.042}$	$^{+0}_{-0.035}$
$B \to X_u\ell\nu$ BF	$^{+0.26}_{-0.52}$	$^{+2.9}_{-2.5}$	$^{+0.89}_{-0.91}$	± 1.2	± 1.1
shape function	$^{+0.20}_{-0.35}$	$^{+1.3}_{-0.86}$	$^{+0.37}_{-0.27}$	$^{+0.59}_{-0.53}$	$^{+0.52}_{-0.44}$
$B \to X_u\ell\nu$ FF	± 1.7	± 3.7	± 2.4	± 2.4	± 2.4
$B\overline{B}$ background	$^{+0.63}_{-0.90}$	$^{+3.4}_{-2.9}$	$^{+2.5}_{-2.4}$	$^{+1.7}_{-1.6}$	± 1.9
$B \to D\ell\nu$ BF	$^{+0}_{-0.13}$	$^{+0.76}_{-0}$	$^{+0.25}_{-0.17}$	$^{+0.20}_{-0}$	$^{+0.21}_{-0.053}$
$B \to D^*\ell\nu$ BF	$^{+2.0}_{-2.2}$	$^{+0.96}_{-1.1}$	± 1.9	$^{+1.6}_{-1.8}$	$^{+1.7}_{-1.8}$
$B \to \{D_1, D_2\}\ell\nu$ BF	$^{+1.6}_{-1.8}$	$^{+1.7}_{-1.3}$	$^{+1.7}_{-1.8}$	± 1.6	± 1.7
$B \to \{D_0^*, D_1'\}\ell\nu$ BF	$^{+0.42}_{-0.36}$	$^{+0.31}_{-0.19}$	$^{+0.11}_{-0.18}$	$^{+0.38}_{-0.30}$	$^{+0.29}_{-0.26}$
continuum background	± 0.88	± 1.4	± 3.6	± 1.1	± 1.2
final state radiation	± 1.2			± 0.60	-
tracking efficiency	± 0.72				
lepton PID efficiency	± 1.8				
neutral veto	± 0.53				
tag factorizability	± 0.26				
B counting	± 1.1				
f_{00}	± 1.4				
total systematic	$^{+\mathbf{4.5}}_{-\mathbf{4.8}}$	$^{+\mathbf{7.2}}_{-\mathbf{6.5}}$	$\pm$**6.4**	$^{+\mathbf{5.0}}_{-\mathbf{5.1}}$	$\pm$**5.1**

Table 9.2: Analogous to Table 9.1, for $B \to \pi^0 \ell\nu$.

q^2 **bin**	**low**	**middle**	**high**	**low+mid**	**total**
yield	± 22	± 27	± 38	± 17	± 16
efficiency	± 4.2	± 4.3	± 4.4	± 2.9	± 2.4
double tag statistics			± 0.60		
total statistical	$\pm$**22**	$\pm$**27**	$\pm$**38**	$\pm$**17**	$\pm$**16**
$B \to \{\rho, \omega\}\ell\nu$ BF	$^{+0.020}_{-0}$	$^{+0.30}_{-0.90}$	$^{+0.68}_{-0.79}$	$^{+0.13}_{-0.35}$	$^{+0.27}_{-0.46}$
$B \to \eta\ell\nu$ BF	$^{+0.021}_{-0}$	$^{+0.12}_{-0.82}$	$^{+0}_{-0.11}$	$^{+0.052}_{-0.32}$	$^{+0.037}_{-0.27}$
$B \to X_u\ell\nu$ BF	$^{+0.034}_{-0}$	$^{+1.2}_{-2.2}$	$^{+1.1}_{-1.5}$	$^{+0.51}_{-0.86}$	$^{+0.66}_{-1.0}$
shape function	$^{+0.077}_{-0.039}$	$^{+0.31}_{-1.0}$	$^{+0.69}_{-1.00}$	$^{+0.17}_{-0.44}$	$^{+0.30}_{-0.58}$
$B \to X_u\ell\nu$ FF	± 0.28	± 0.29	± 7.5	± 0.28	± 2.1
$B\overline{B}$ background	$^{+2.3}_{-2.2}$	$^{+7.4}_{-6.9}$	$^{+7.6}_{-6.5}$	$^{+4.4}_{-4.2}$	$^{+5.2}_{-4.7}$
$B \to D\ell\nu$ BF	± 0.78	$^{+0.37}_{-0.56}$	$^{+0.82}_{-0.95}$	$^{+0.61}_{-0.69}$	$^{+0.66}_{-0.75}$
$B \to D^*\ell\nu$ BF	± 1.1	$^{+1.3}_{-1.5}$	$^{+0.93}_{-1.0}$	$^{+1.1}_{-1.3}$	$^{+1.1}_{-1.2}$
$B \to \{D_1, D_2\}\ell\nu$ BF	± 1.9	$^{+1.3}_{-2.0}$	$^{+2.0}_{-2.1}$	$^{+1.6}_{-1.9}$	$^{+1.7}_{-2.0}$
$B \to \{D_0^*, D_1'\}\ell\nu$ BF	$^{+0.13}_{-0.032}$	$^{+0.073}_{-0.34}$	$^{+0.031}_{-0.12}$	$^{+0.011}_{-0.062}$	$^{+0.016}_{-0.076}$
continuum background	± 0.66	± 0.98	± 5.2	± 0.79	± 1.0
final state radiation		± 1.2		± 0.60	-
tracking efficiency			± 0.36		
π^0 efficiency			± 3.0		
lepton PID efficiency			± 1.8		
neutral veto			± 1.6		
tag factorizability			± 0.30		
B counting			± 1.1		
f_{00}			± 1.4		
total systematic	$\pm$**5.6**	$^{+\mathbf{9.0}}_{-\mathbf{9.1}}$	$\pm$**12**	$\pm$**6.6**	$^{+\mathbf{7.5}}_{-\mathbf{7.3}}$

Table 9.3: Analogous to Table 9.1, for $B \to \eta\ell\nu$.

q^2 **bin**	**low**	**middle**	**high**	**low+mid**	**total**
yield	± 36	± 71	± 61	± 34	± 30
efficiency	± 4.8	± 6.0	± 6.5	± 3.5	± 3.1
double tag statistics	± 0.60				
total statistical	$\pm$**36**	$\pm$**71**	$\pm$**61**	$\pm$**34**	$\pm$**30**
$B \to \{\rho, \omega\}\ell\nu$ BF	$^{+0.074}_{-0.075}$	± 1.5	$^{+0.74}_{-0.61}$	$^{+0.50}_{-0.48}$	$^{+0.57}_{-0.52}$
$B \to \pi\ell\nu$ BF	$^{+0.067}_{-0}$	$^{+0.59}_{-0.94}$	$^{+0}_{-0.73}$	$^{+0.23}_{-0.30}$	$^{+0}_{-0.30}$
$B \to X_u\ell\nu$ BF	$^{+0.18}_{-0.035}$	$^{+1.8}_{-3.1}$	$^{+1.4}_{-1.2}$	$^{+0.63}_{-1.0}$	$^{+0.90}_{-1.1}$
shape function	$^{+0.096}_{-0.037}$	$^{+1.4}_{-2.0}$	$^{+4.0}_{-0.93}$	$^{+0.47}_{-0.65}$	$^{+1.3}_{-0.71}$
$B \to X_u\ell\nu$ FF	± 0.29	± 2.6	± 1.9	± 1.1	± 0.13
$B\overline{B}$ background	$^{+0.20}_{-0.15}$	$^{+6.8}_{-6.5}$	$^{+3.6}_{-0.59}$	$^{+2.3}_{-2.2}$	$^{+2.7}_{-1.7}$
$B \to D\ell\nu$ BF	$^{+0.85}_{-0.71}$	$^{+0.19}_{-0.81}$	$^{+0.85}_{-1.4}$	$^{+0.61}_{-0.74}$	$^{+0.69}_{-0.96}$
$B \to D^*\ell\nu$ BF	$^{+1.2}_{-1.1}$	$^{+0.60}_{-0.97}$	$^{+3.6}_{-0}$	$^{+0.99}_{-1.1}$	$^{+0.88}_{-0}$
$B \to \{D_1, D_2\}\ell\nu$ BF	$^{+1.8}_{-1.9}$	$^{+1.7}_{-2.1}$	± 1.9	$^{+1.8}_{-2.0}$	$^{+1.8}_{-1.9}$
$B \to \{D_0^*, D_1'\}\ell\nu$ BF	$^{+0.18}_{-0.13}$	$^{+0.93}_{-1.1}$	$^{+0.26}_{-0}$	$^{+0.25}_{-0.30}$	$^{+0.25}_{-0.12}$
continuum background	± 0.058	± 0.101	± 0.29	± 0.074	± 0.076
final state radiation	± 1.2		± 2.3	± 0.60	-
η BFs	± 0.56				
tracking efficiency	± 0.49				
π^0 efficiency	± 1.7				
lepton PID efficiency	± 1.7				
neutral veto	± 1.6				
tag factorizability	± 0.30				
B counting	± 1.1				
f_{00}	± 1.4				
total systematic	$\pm$**4.4**	$^{+\mathbf{8.8}}_{-\mathbf{9.3}}$	$^{+\mathbf{8.4}}_{-\mathbf{5.5}}$	$^{+\mathbf{5.0}}_{-\mathbf{5.1}}$	$^{+\mathbf{5.2}}_{-\mathbf{4.7}}$

Table 9.4: Summary of (fractional) uncertainties on branching fraction measurements for $B \to \eta' \ell\nu$, in "low+mid" ($q^2 < 16$ GeV$^2/c^2$) bin and total (all q^2). All values are given in percent.

q^2 **bin**	**low+mid**	**total**
yield	± 440	± 609
efficiency	± 6.8	± 6.7
double tag statistics	± 0.60	
total statistical	$\pm$**440**	$\pm$**609**
$B \to \{\rho, \omega\}\ell\nu$ BF	$^{+0.0071}_{-0}$	$^{+0.25}_{-0.53}$
$B \to \pi\ell\nu$ BF	$^{+0.00076}_{-0}$	$^{+0.022}_{-0}$
$B \to X_u\ell\nu$ BF	$^{+0.030}_{-0}$	$^{+1.0}_{-0.77}$
shape function	$^{+0.030}_{-0}$	$^{+0.25}_{-0.52}$
$B \to X_u\ell\nu$ FF	± 0.30	± 1.1
$B\overline{B}$ background	$^{+87}_{-111}$	$^{+41}_{-56}$
$B \to D\ell\nu$ BF	$^{+0.61}_{-0.63}$	$^{+0.28}_{-0}$
$B \to D^*\ell\nu$ BF	± 1.2	$^{+2.5}_{-3.0}$
$B \to \{D_1, D_2\}\ell\nu$ BF	$^{+1.8}_{-2.7}$	± 3.1
$B \to \{D_0^*, D_1'\}\ell\nu$ BF	$^{+0}_{-1.8}$	$^{+140}_{-0.62}$
continuum background	± 2.7	± 2.3
final state radiation	± 0.60	-
η, η' BFs	± 3.2	
tracking efficiency	± 1.2	
π^0 efficiency	± 1.3	
lepton PID efficiency	± 1.7	
neutral veto	± 1.6	
tag factorizability	± 0.30	
B counting	± 1.1	
f_{00}	± 1.4	
total systematic	$^{+\mathbf{87}}_{-\mathbf{111}}$	$^{+\mathbf{146}}_{-\mathbf{57}}$

are repeated with simulated decays reweighted to implement the following variations:

- the $B \to \rho^{\pm}\ell\nu$, $B \to \rho^{0}\ell\nu$ and $B \to \omega\ell\nu$ branching fractions (BF) are varied $+\sigma$ and $-\sigma$ from their known central values,[2]
- the $B \to \pi^{\pm}\ell\nu$ and $B \to \pi^{0}\ell\nu$ branching fractions are varied $+\sigma$ and $-\sigma$ (for $\eta\ell\nu$ and $\eta'\ell\nu$ signal mode measurements only),
- the $B \to \eta\ell\nu$ branching fraction is varied $+\sigma$ and $-\sigma$ while the $B \to \eta'\ell\nu$ branching fraction is constrained to it (for $\pi^{\pm}\ell\nu$ and $\pi^{0}\ell\nu$ signal mode measurements only),
- the inclusive charmless $B \to X_u\ell\nu$ branching fraction is varied $+\sigma$ and $-\sigma$ (while the aforementioned exclusive branching fractions are held constant),
- the inclusive charmless $B \to X_u\ell\nu$ decay spectra are varied, considering eleven different points on the σ contour[3] in shape function and heavy quark effective theory parameter space [39],
- the (exclusive) charmless decay form factors (FF) follow the ISGW2 model [27] (rather than Ball & Zwicky). As ISGW2 is experimentally excluded at present, it is conservatively taken as a "σ upper limit" on form factor wrongness.

For each, the largest deviation in either direction is taken as the associated systematic uncertainty, except for the form factor variation, for which the (single) deviation is applied symmetrically.

9.1.2 Background spectra

The uncertainty associated with the accuracy of $B\overline{B}$ background modeling is quantified via the study of a signal-depleted control sample, specifically, events for which at least one of the following is true:

- there is (exactly) one track in the event with momentum no less than 200 MeV/c and not overlapping the $D\ell$ and $X\ell$ candidates,
- the event contains at least 200 MeV in extra neutral energy, and/or

[2] See Table 5.2.

[3] See §5, Footnote 13.

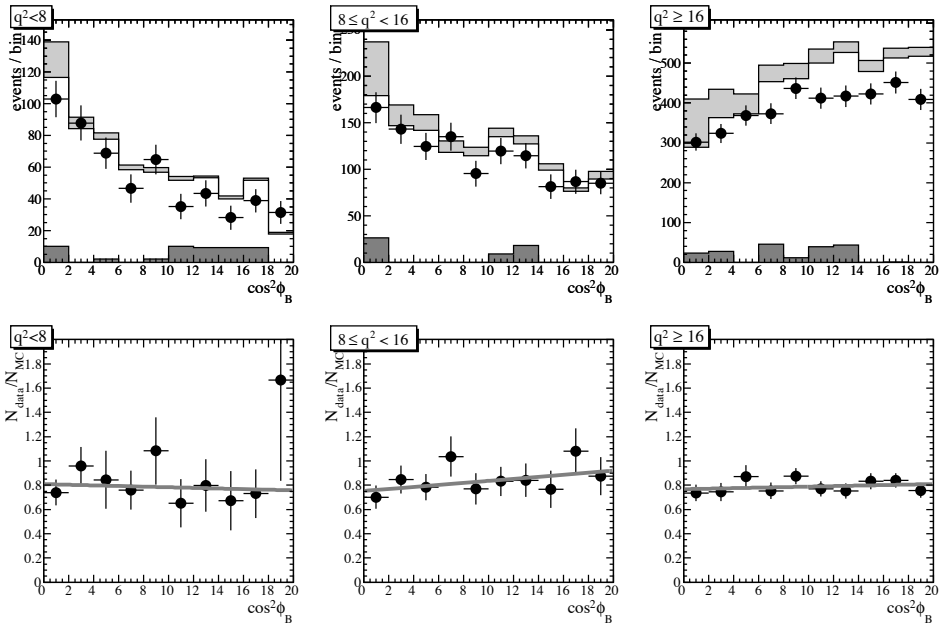

Figure 9.1: Comparison of $\cos^2\phi_B$ spectra in on-peak data to simulated and off-peak data for signal-depleted control sample, for $\pi^{\pm}\ell\nu$ signal mode. In the top row, points are data; histograms (stacked) are: simulated charmless semileptonic decays (light grey), other simulated $B\overline{B}$ events (white) and off-peak data ((dark) grey). The bottom row shows bin-by-bin ratios, with a linear fit.

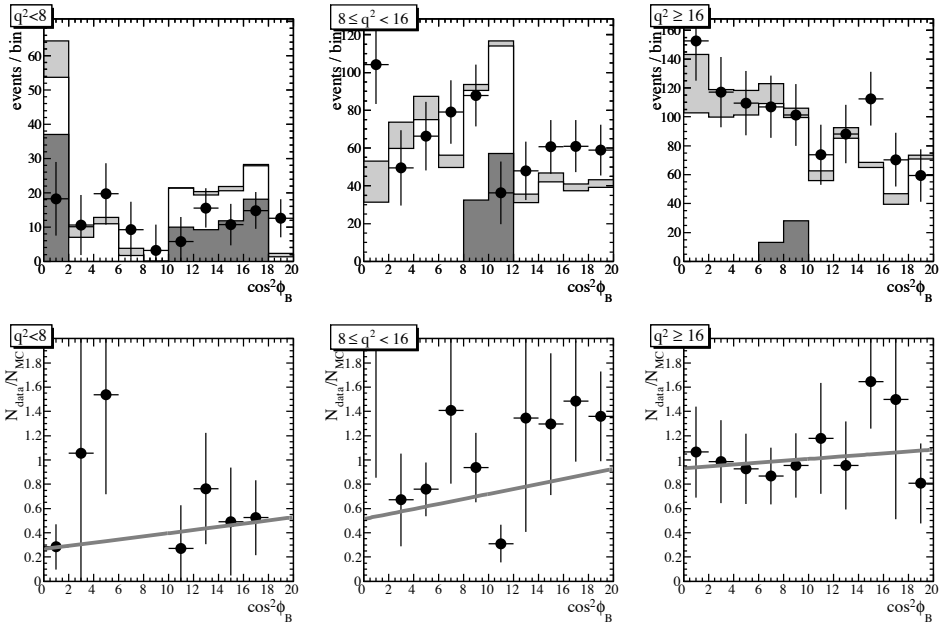

Figure 9.2: Analogous to Figure 9.1, for $\pi^0\ell\nu$ signal mode.

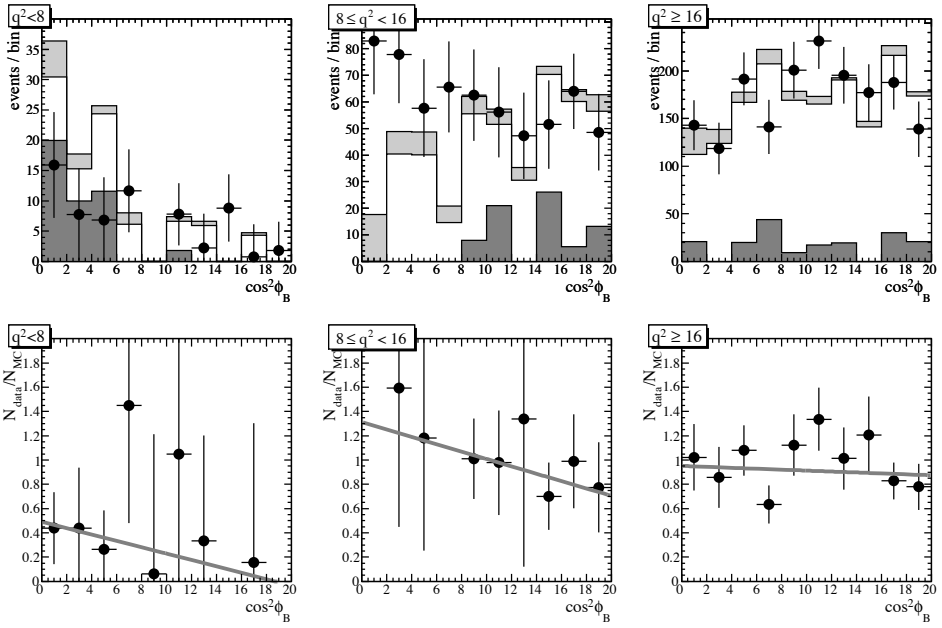

Figure 9.3: Analogous to Figure 9.1, for $\eta\ell\nu$ signal mode.

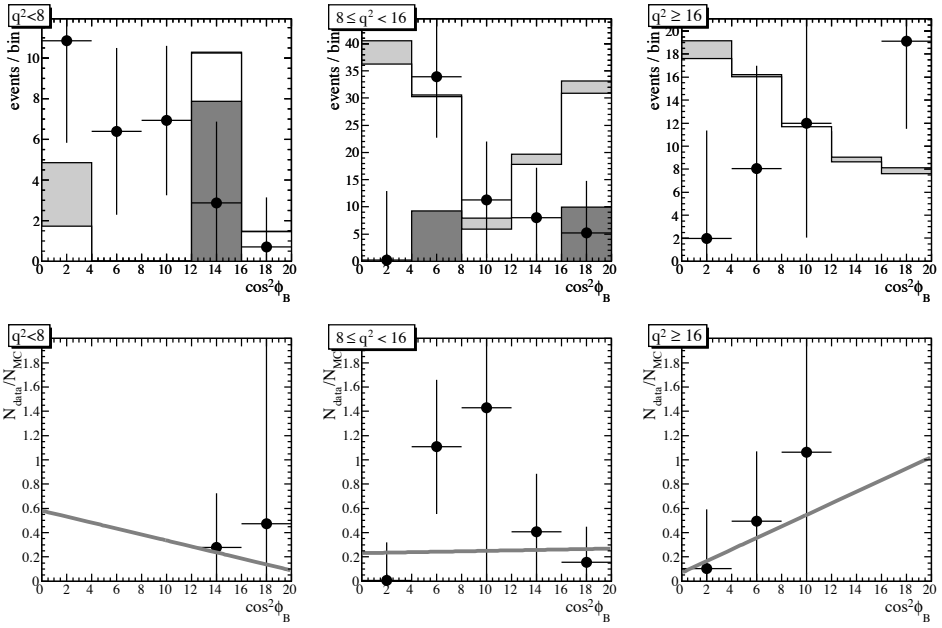

Figure 9.4: Analogous to Figure 9.1, for $\eta'\ell\nu$ signal mode.

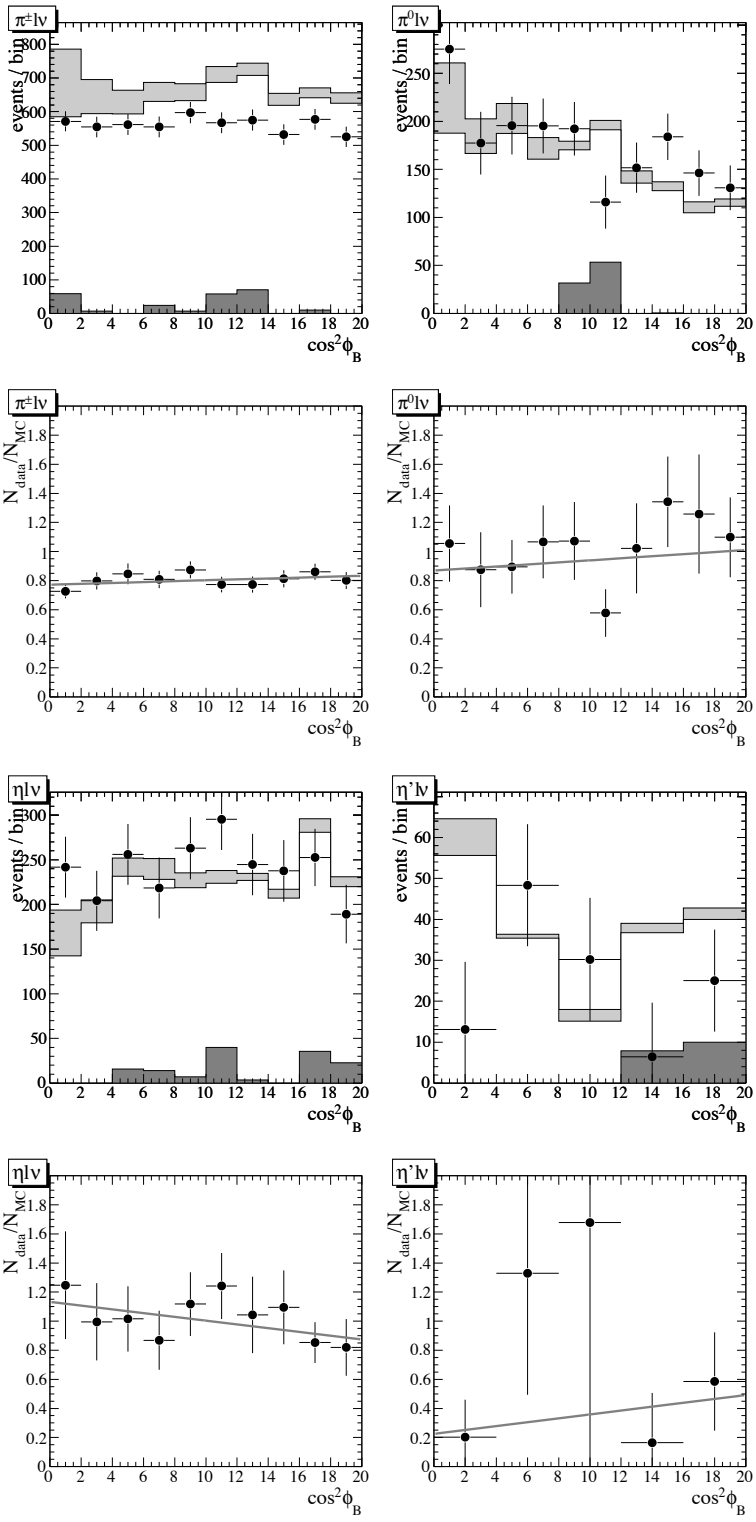

Figure 9.5: Analogous to Figures 9.1–9.4, but without separation into q^2 bins.

Table 9.5: Fit result for parameter b (described in text), measuring appropriately normalized slopes in the fits shown in Figures 9.1–9.5. Numbers are given in units of 10^{-2}. Listed uncertainties are statistical.

	$q^2 < 8$	$8 \leq q^2 < 16$	$q^2 > 16$ GeV$^2/c^2$	combined
$\pi\ell\nu$	-0.3 ± 1.3	1.1 ± 1.0	0.3 ± 0.5	0.4 ± 0.4
$\pi^0\ell\nu$	4.9 ± 10.2	4.0 ± 6.3	0.8 ± 2.4	0.8 ± 1.9
$\eta\ell\nu$	-5.3 ± 4.9	-2.3 ± 2.0	-0.4 ± 1.2	-1.1 ± 1.0
$\eta'\ell\nu$	-4.2 ± 8.3	0.8 ± 12.1	68 ± 702	5.9 ± 17.6

- the event contains a $K^0_S \to \pi^+\pi^-$ candidate not overlapping the $D\ell$ candidate,

in addition to all of the usual requirements (not contradicting which of these are true). The resultant $\cos^2\phi_B$ distributions are compared between and on-peak data and simulated (and off-peak) data; bin-by-bin ratios are χ^2 fit to a linear function $a \times (1 + b\cos^2\phi_B)$, as shown in Figures 9.1–9.5; fit results are presented in Table 9.5.

The charmless decays have nontrivial contributions in the low $\cos^2\phi_B$ region, much of which are events such as $B \to \rho^0\ell\nu$ (with $\rho^0 \to \pi^+\pi^-$) reconstructed as $B \to \pi^+\ell\nu$, in which the reconstructed $\cos^2\phi_B$ (with an "ignored" π^- track) is correlated with the true $\cos^2\phi_B$ (accounting for the whole ρ^0 meson). The studies described in §9.1.1 also account for uncertainties due to estimating contributions from such events (in the non-control sample).

As the overall background normalization is known to be different in data and simulated data, and is a floating parameter in the yield extraction, only the quantity b is relevant. It shows good agreement with zero, as desired.

The precision to which b can be determined to be zero is propagated to an uncertainty by repeating, for each signal mode, the yield extraction twice, with a weight of $1 \pm \sigma_b \cos^2\phi_B$, where σ_b is the uncertainty on b as derived from the fit over the full q^2 range, except in the $\eta'\ell\nu$ mode where, due to lack of statistics, the value derived for the $\pi^0\ell\nu$ mode[4] is used. The fractional deviations in each direction are taken as the associated systematic uncertainty.

9.1.3 Charmed semileptonic decay

This analysis is sensitive to uncertainties in charmed $B \to X_c\ell\nu$ branching fractions (and decay spectra) in two regards: in the modeling of $B\overline{B}$ background, for which the systematic

[4] i.e., the larger of the other two σ_be.

uncertainty applied in §9.1.2 in principle accounts, and in the calculation of the selection efficiency, for which the efficiency corrections derived in §7.2 account. However, the double tag procedure corrects only for overall tagging rates and assumes that $B \to X_c \ell\nu$ decays are modeled correctly. Thus, a conservative approach is taken: the yield extraction and efficiency studies (including double tag derived corrections) are repeated with events weighted to implement the following variations:[5]

- the $B \to D\ell\nu$ branching fractions are varied $\pm 15\%$, while all other $B \to X_c\ell\nu$ branching fractions are varied $\mp 1.8\%$ from their central values,
- the $B \to D^*\ell\nu$ branching fractions are varied $\pm 24\%$, while all other $B \to X_c\ell\nu$ branching fractions are varied $\mp 5.2\%$,
- the $B \to D_1\ell\nu$ and $B \to D_2\ell\nu$ branching fractions are varied $\pm 20\%$, while all other $B \to X_c\ell\nu$ branching fractions are varied $\mp 2\%$, and
- the $B \to D_0^*\ell\nu$ and $B \to D_1'\ell\nu$ branching fractions are varied $\pm 25\%$, while the nonresonant $B \to X_c\ell\nu$ branching fractions are varied $\mp 75\%$.

For each, the larger deviation in each direction is taken as the associated systematic uncertainty.

9.1.4 Continuum background

Because the expected contribution from continuum (non-$B\overline{B}$ pair production) background is small, it is not addressed explicitly in the yield extraction method. Instead, the abundances of background events in the approximate signal regions ($\cos^2\phi_B \geq 1.5$) are estimated and considered as systematic uncertainties.

All event and candidate selection requirements are applied to off-peak data (including candidate selection and D mass sideband subtraction), which is then scaled to the integrated luminosity and pair production cross section[6] of the on-peak data. The resulting $\cos^2\phi_B$

[5]These variations summarize the uncertainties found in Table 5.3, and take into account branching fractions constrained by isospin symmetry and/or with correlated uncertainties. For each variation, other $B \to X_c\ell\nu$ branching fractions are varied in the opposite direction such that the total $B \to X_c\ell\nu$ branching fractions (for variations of which the study in §7.2 accounts) are held constant.

[6]This contributes a factor of the ratio of squared center-of-mass energies: $(10.58\,\mathrm{GeV}/10.54\,\mathrm{GeV})^2$.

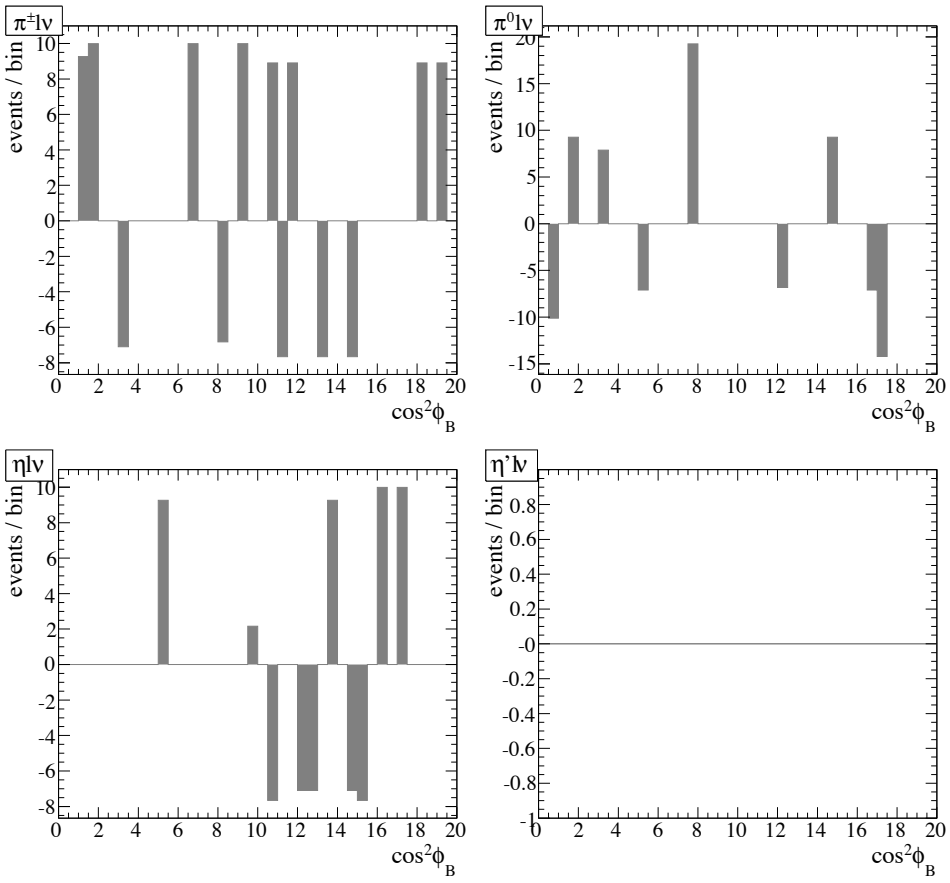

Figure 9.6: Off-peak data $\cos^2\phi_B$ spectra, scaled to the integrated luminosity and center-of-mass energy of the on-peak data.

Table 9.6: Estimated number of continuum events in the signal regions. The second column lists estimates taken directly from the (scaled) abundance of off-peak data fulfilling all selection criteria. The third column lists the abundances of off-peak data without selection for extra neutral energy. These are multiplied by a scale factor (fourth column) for a better estimate (fifth column) of the number of events in the signal region. (See text for details.)

	estimated	without extra energy cut	scale factor	estimated
$\pi^{\pm}\ell\nu$	9.3 ± 9.3	19.2 ± 6.9	0.096	1.8 ± 0.4
$\pi^0\ell\nu$	-10.1 ± 10.1	14.4 ± 15.1	0.099	1.4 ± 0.3
$\eta\ell\nu$	0.0 ± 0.0	-0.53 ± 0.85	0.049	0.026 ± 0.042
$\eta'\ell\nu$	0.0 ± 0.0	-0.07 ± 1.11	0.053	-0.004 ± 0.059

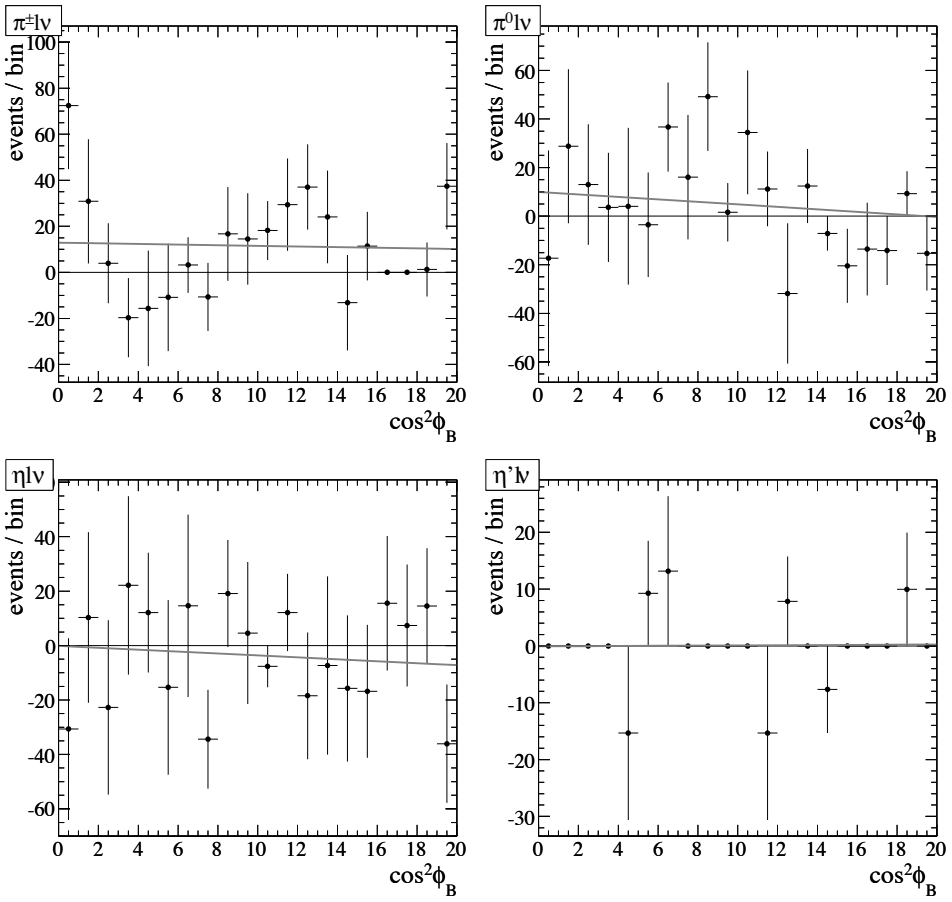

Figure 9.7: Off-peak data (scaled) without extra neutral energy requirement $\cos^2\phi_B$ spectra. Each is fit to a straight line.

spectra are shown in Figure 9.6; the abundances of events in the signal regions are consistent with zero and shown in Table 9.6.

However, these estimates carry large statistical uncertaintines and are thus refined using this method: off-peak data with all event and candidate selection requirements applied except those on extra neutral energy are considered. For each signal mode, the $\cos^2\phi_B$ spectrum is (unbinned maximum likelihood) fit to a straight line, shown in Figure 9.7. The fit result and uncertainty are used to estimate the number of events in the signal region. The effect of the extra neutral energy requirement is then approximated by scaling this estimate by the ratio of on-peak data events after and before the extra energy cut is applied (the "scale factor"). The results are shown in Table 9.6.

For each mode, the larger of this refined estimate and its uncertainty is taken as a systematic uncertainty. This is a rather conservative approach as the presence of continuum

backround does not directly shift the derived signal yield; insofar as the spectrum of the continuum background resembles that of the $B\overline{B}$ background, the fit can accommodate it somewhat in the the background yield.

Because continuum background events are observed to tend to populate the high q^2 region, for the calculation of uncertainties for the $q^2 \geq 16$ GeV$^2/c^2$ bins, it is assumed that all continuum background is concentrated in them. For uncertainties in other q^2 bins, it is assumed that continuum background events are distributed evenly across q^2. The fractional size of this uncertainty is computed directly from the extracted yield, i.e., using the approximation that the efficiency matrices (Equations 7.4–7.7) are diagonal.

9.1.5 Final state radiation

Final state radiation can shift the q^2 spectra at the B decay level to the q^2 spectra measured in the lab.[7] This has been found in Monte Carlo studies to be no greater than a 1.2% effect (at the underlying physics level) to the $\pi^{\pm}\ell\nu$ signal yield in each bin. This is taken conservatively[8] as a systematic uncertainty on the q^2 bin partial branching fractions $\Delta\mathcal{B}(B \to \pi\ell\nu)$. As the yields in the low ($q^2 < 8$ GeV$^2/c^2$) and middle ($8 \leq q^2 < 16$ GeV$^2/c^2$) bins are roughly equal, half of this is applied in the $q^2 < 16$ GeV$^2/c^2$ case.

This systematic uncertainty is also applied in the other modes, which have comparable kinematics. In the $q^2 \geq 16$ GeV$^2/c^2$ bin of the $\eta\ell\nu$ mode, this 1.2% is scaled by the ratio of the fractional yields in the $\pi^{\pm}\ell\nu$ and $\eta\ell\nu$ modes using results from Table 8.1, i.e., allowing for the same total rate of bin migration compared to a decreased yield in that bin. (For $\eta^{(\prime)}\ell\nu$ modes, final state radiation effects should in fact be smaller, as heavier mesons admit less phase space for radiation.)

9.1.6 Branching fractions of η, η' mesons

For the $\eta\ell\nu$ signal mode, uncertainties on η branching fractions (as listed in Table 5.4) are combined, taking into account the relative abundance of decays in each mode (after reconstruction) measured from simulated data.

[7] This effect is ameliorated by the fact that the kinematics of the final state meson, rather than that of the lepton, are used to determine q^2.

[8] This number reflects the total effect when, in fact, the effect is modeled in simulation.

The resulting uncertainty is applied to the $\eta'\ell\nu$ mode as well, along with an additional 3.1% for the uncertainty on $\mathcal{B}(\eta' \to \eta\pi^+\pi^-)$.

9.2 Modeling of detector response

Because the double tag study determines tagging efficiency directly from data,[9] systematic uncertainties associated with the modeling of detector response are applied only to reconstructed particles on the signal side of events. These measurements are sensitive to such effects primarily through the determination of the reconstruction efficiency. They are assumed to be independent of q^2.

The efficiency of charged track reconstruction has been measured in the study of three-prong τ decays ($\tau^+ \to \pi^+\pi^+\pi^-\overline{\nu}_\tau$) found in the recoil of the decay $\tau^- \to \ell^-\overline{\nu}_\ell\nu_\tau$ to be 0.36% (added linearly) per track. The $\pi^\pm\ell\nu$ and $\pi^0\ell\nu$ modes have two and one signal side tracks respectively; for $\eta^{(\prime)}\ell\nu$ channels, the average number of tracks is determined from reconstructed simulated signal events.

The efficiency of π^0 meson reconstruction is measured from the relative efficiencies of $\tau^+ \to \pi^+\overline{\nu}$ and $\tau^+ \to \rho^+\overline{\nu}$ reconstruction (in the recoil of $\tau^- \to e^-\overline{\nu}_e\nu_\tau$), which are determined by comparing measured data to Monte Carlo prediction. As $\rho^+ \to \pi^+\pi^0$, with knowledge of the tracking efficiency, the π^0 reconstruction efficiency can be inferred with 3% uncertainty (per π^0 candidate).

The lepton identification efficiencies (PID) were determined in the same studies, described in §5.1.3, by which the `PidLHElectrons` and `MuonNNTight` criteria were developed; the uncertainties thereon have been found to be ±2% and ±3% per electron and muon, repectively.

The $K^0_S \to \pi^+\pi^-$ efficiency has been measured with a large inclusive K^0_S data set to be accurate to within 3%. As the K^0_S efficiency affects the signal side of events only via the K^0_S veto, varying it has been found to have a negligible (less than a 1‰) effect on measured branching fractions; its contribution to the uncertainty is thus ignored.

[9] See §7.2.

Table 9.7: Ratios of double tag events found in on-peak data to those in simulated data, for various requirements on extra neutral energy.

$B^0\overline{B}^0$		B^+B^-	
maximum $E^*_{\rm extra}$	$N_{\rm data}/N_{\rm MC}$	maximum $E^*_{\rm extra}$	$N_{\rm data}/N_{\rm MC}$
280 MeV	0.946 ± 0.029	140 MeV	0.996 ± 0.011
140 MeV	0.932 ± 0.026	70 MeV	1.008 ± 0.015
∞	0.941 ± 0.025	∞	0.980 ± 0.011

Table 9.8: Number of combinatoric events surviving sideband subtraction in the double tag analysis.

	$B^0\overline{B}^0$	B^+B^-
one D bad	7.58 ± 8.32	-6.90 ± 28.3
both Ds bad	-2.61 ± 2.51	3.03 ± 19.7

9.3 Double tag analysis

Several systematic uncertainties are associated with the double tag correction factors derived in §7.2.

9.3.1 Neutral veto

To quantify possible effects of the extra energy requirement on the tagging efficiency, the study of double tag events is repeated, varying requirements on extra neutral energy: it is tightened to the values used in the main analysis, and removed completely. The ratios of double tag events found in on-peak data to those found in simulated data are shown in Table 9.7. For each mode, the greater fractional deviation in $N_{\rm data}/N_{\rm MC}$ is applied as a symmetric systematic uncertainty. Although it is the square root of this quantity that is used in calculating measured branching fractions,[10] this uncertainty is not halved to hedge for the possibility that it is not a per-tag effect.

9.3.2 Factorizability of tags

An untested assumption is made in deriving the efficiency correction factor: that D backgrounds can be factorized. If this is the case, simulated double tag events in which one or

[10] See Equation 7.8.

both tags is not matched to a true D meson should be nonexistent in the D mass peak region after sideband subtraction (up to statistical uncertainty).

Indeed this is the case; results are shown in Table 9.8. The larger of the (absolute) value and its uncertainty for the two cases (one or both bad D candidates) are added linearly and taken as a systematic uncertainty.

9.4 Bremsstrahlung modeling

As many studies of $b \to u\ell\nu$ transitions rely on lepton momentum spectra to distinguish them from more copious $b \to c\ell\nu$ backgrounds and are thus limited by how well bremsstrahlung processes are understood, several studies were performed to demonstrate that the above systematic uncertainties sufficiently account for such effects.

In these measurements, the effect of uncertainty in modeling bremsstrahlung on $D\ell\nu$ tagging efficiencies and $B\overline{B}$ background $\cos^2\phi_B$ spectra has been taken into account via the double tag (§7.2) and $B\overline{B}$ background (§9.1.2) studies respectively. The effect of inner bremsstrahlung[11] on the q^2 distribution is taken into account by the final state radiation study (§9.1.5). Still, such uncertainty can still lead to inaccurate determination of:

- signal efficiencies (through lepton acceptance), and
- signal $\cos^2\phi_B$ spectra.

The potential effect of the former is studied with a sample of simulated events, each containting a $B \to \pi^{\pm} e\nu$ decay.[12] A set of $400,000$ events, half with and half without simulation of inner bremsstrahlung via the `PHOTOS` radiation simulator [44], is generated. (Detector effects are not considered in this study.) The electron momentum spectra, after a rough fiducial cut on the electron (laboratory frame) direction ($0.35 \leq \theta_e \leq (\pi - 0.45)$), are shown in Figure 9.8. For a lepton absolute momentum requirement of $800\,\mathrm{MeV}/c$, as is applied to events in these measurements, the estimated total effect of bremsstrahlung is a 1.3% reduction in the electron efficiency. However, given that electrons constitute roughly half of

[11] The determination of q^2 is via X_u kinematics rather than that of the lepton, and is thus manifestly insensitive to outer bremsstrahlung.

[12] These are generated according to the ISGW2 [27] form factor model, the specifics of which are unimportant for this study.

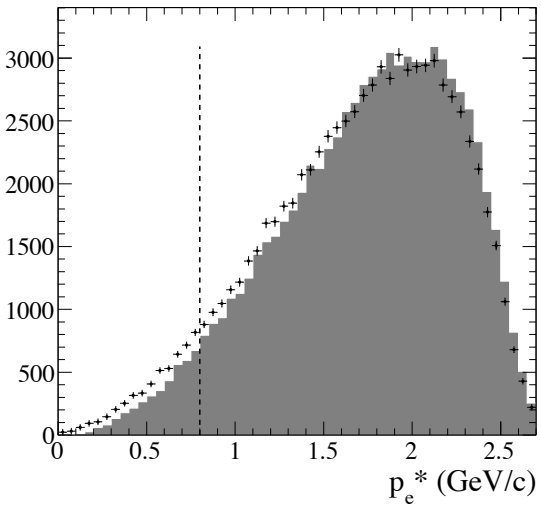

Figure 9.8: Electron (true) momentum spectrum for $B \to \pi^{\pm}\ell\nu$ decays, simulated with (points) and without (shaded) bremsstrahlung. Leptons are required to have absolute momentum greater than $800\,\mathrm{MeV}/c$.

the lepton sample and that the simulated data is not expected to be 100% wrong, the true uncertainty is, at most, several times smaller than that.

The potential effect of outer bremsstrahlung on the signal efficiency is estimated in a similar manner. Simulated $B \to \pi^{\pm}e\nu$ events fulfilling all selection criteria as well as the requirement that the true absolute momentum of the (signal side) electron be no less than $800\,\mathrm{MeV}/c$, the p_e^* spectra are shown in Figure 9.9. The difference in efficiency of an absolute momentum requirement $p_e^* \geq 1.6\,\mathrm{GeV}/c$,[13] when applied to the true lepton momentum versus the measured lepton momentum, is an 8% reduction in acceptance. This is a particularly conservative upper limit, given that:

- the detector simulation also includes $\mathrm{d}E/\mathrm{d}x$,
- the detector simulation also includes resolution, which is asymmetric because of the slope of the spectra $p_e^* = 1.6\,\mathrm{GeV}/c$,
- these electrons are harder than the sample used in the measurements and thus tend to radiate more energy, and

[13]The $p_\ell^* \geq 0.8\,\mathrm{GeV}/c$ requirement cannot be studied directly without costing a significant amount of computational overhead, as the `BToDlnu` skim includes a minimum lepton momentum requirement.

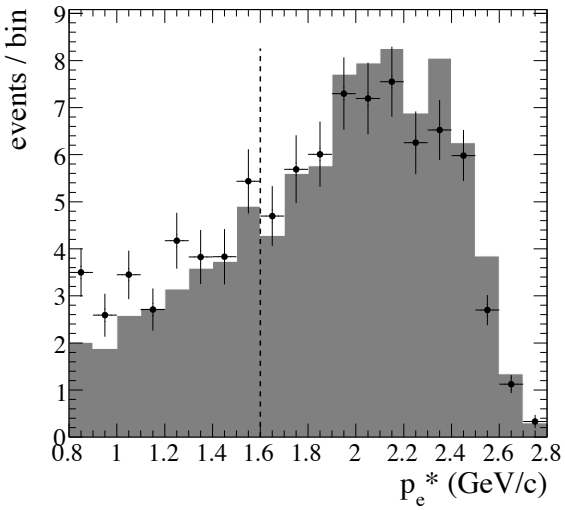

Figure 9.9: Electron momentum spectrum for $B \to \pi^{\pm}\ell\nu$ decays, simulated with (points) and without (shaded) detector simulation.

- these electrons are more clustered near $p_e^* = 1.6\,\mathrm{GeV}/c$ than is the full spectrum around $p_e^* = 0.8\,\mathrm{GeV}/c$.

Again, given that roughly half of reconstructed leptons are electrons, the modeling of outer bremsstrahlung in the *BABAR* simulation would have to be quite incorrect to show an appreciable effect. However, studies of radiative Bhabha events have shown that the effective density of detector material (X/X_0) in simulation is accurate to within 3%.

The effect of bremsstrahlung modeling on the signal $\cos^2\phi_B$ spectra is evaluated by performing the $B \to \pi^{\pm}\ell\nu$ signal extraction[14] without and with the bremsstrahlung photon recovery procedure described in §6.3.2 applied to the signal sample.[15] Not recovering bremsstrahlung photons results in -0.4%, -0.2% and $+0.1\%$ shifts in the yield in the three q^2 bins (low to high).

As these effects are on the order per mill or smaller, they are considered negligible. Assuming comparable lepton momentum spectra, this conclusion is generalized to all other signal modes.

Corresponding effects from muons are far smaller at energies attainable at *BABAR*.

[14] on toy data.

[15] Because recovered photons are considered in the calculation of $\cos^2\phi_B$, this approximates increasing the bremsstrahlung rate by the inverse of the recovery efficiency.

9.5 Other uncertainties

The size of the data samples are determined by counting Bhabha and dimuon ($e^+e^- \to \mu^+\mu^-$) events; the number of $B\overline{B}$ pairs in the on-peak data sample ("B counting") is known up to 1.1% (statistical plus systematic) uncertainty.

The fraction of these $B\overline{B}$ pairs that are $B^0\overline{B}^0$ pairs is known to be $f_{00} = 0.491 \pm 0.007$ [9], which translates to a 1.4% systematic uncertainty on measured branching fractions.[16]

[16]The study described in §9.1.2 accounts for the effect of the f_{00} uncertainty on the $\cos^2\phi_B$ shape of the $B\overline{B}$ background.

Chapter 10

Results

The partial and total branching fractions measured are given in Table 10.1.

10.1 Correlation of statistical uncertainties

Events that appear signal-like in multiple modes are not explicitly rejected in the event and candidate selection process; their presence can in principle correlate the statistical uncertainties on the measured branching fractions.

To estimate the potential effect of this, for each pair of signal modes, simulated signal events for both modes are subject to all selection criteria described in §6 for both modes. The number of events passing selection criteria and appearing signal-like ($\cos^2 \phi_B \leq 1.5$) in both modes is listed in Table 10.2 and is used to estimate the pairwise correlation between the statistical uncertainties of the measured branching fractions in the two modes.

Because quoted statistical uncertainties also include statistical uncertainties on the reconstruction efficiency, the B^+ branching fractions are also in principle correlated by the common double tag[1] correction, given by Equation 7.10: a contribution to the statistical uncertainty of 0.60% is common to all $B \to \pi^0 \ell\nu$, $B \to \eta \ell\nu$ and $B \to \eta' \ell\nu$ branching fractions.

Both of these correlations are considered negligible.

[1] See §7.2.

Table 10.1: Charmless semileptonic B branching fractions measured, in units of 10^{-4}; the first uncertainty stated is statistical, the second systematic. Ranges for q^2 are given in GeV^2/c^2. The combined $B \to \pi\ell\nu$ branching fractions are expressed as $B^0 \to \pi^-\ell^+\nu$ branching fractions.

	$q^2 < 8$	$8 \le q^2 < 16$	$q^2 \ge 16$	$q^2 < 16$	total
$B^0 \to \pi^-\ell^+\nu$	$0.59 \pm 0.12 \pm 0.03$	$0.34 \pm 0.11 \pm 0.02$	$0.46 \pm 0.14 \pm 0.03$	$0.92 \pm 0.16 \pm 0.05$	$1.38 \pm 0.21 \pm 0.07$
$B^+ \to \pi^0\ell^+\nu$	$0.43 \pm 0.09 \pm 0.02$	$0.29 \pm 0.08 \pm 0.03$	$0.24 \pm 0.09 \pm 0.03$	$0.73 \pm 0.12 \pm 0.05$	$0.96 \pm 0.15 \pm 0.07$
$B^+ \to \eta\ell^+\nu$	$0.28 \pm 0.10 \pm 0.01$	$0.16 \pm 0.11 \pm 0.01$	$0.21 \pm 0.13^{+0.02}_{-0.01}$	$0.43 \pm 0.15 \pm 0.02$	$0.64 \pm 0.20 \pm 0.03$
$B^+ \to \eta'\ell^+\nu$	-	-	-	$-0.05 \pm 0.22^{+0.04}_{-0.06}$	$0.04 \pm 0.22^{+0.05}_{-0.02}$
combined $B \to \pi\ell\nu$	$0.67 \pm 0.10 \pm 0.03$	$0.43 \pm 0.09 \pm 0.03$	$0.46 \pm 0.11 \pm 0.04$	$1.08 \pm 0.13^{+0.05}_{-0.06}$	$1.54 \pm 0.17 \pm 0.09$

Table 10.2: For each pair of signal modes, the number of events expected to be reconstructed as signal in each (N_1, N_2) and both ($N_{\rm both}$). The correlation is calculated as $\sigma^2_{\rm both}/\sigma_1\sigma_2$, where σ_i is the (statistical) uncertainty on N_i.

mode 1	mode 2	N_1	N_2	$N_{\rm both}$	correlation
$\pi^\pm\ell\nu$	$\pi^0\ell\nu$	119 ± 3	77 ± 2	0.052 ± 0.050	0.041%
$\pi^\pm\ell\nu$	$\eta\ell\nu$	119 ± 3	54 ± 2	0	0
$\pi^\pm\ell\nu$	$\eta'\ell\nu$	119 ± 3	11 ± 1	0	0
$\pi^0\ell\nu$	$\eta\ell\nu$	78 ± 2	57 ± 2	0.58 ± 0.15	0.67%
$\pi^0\ell\nu$	$\eta'\ell\nu$	77 ± 2	11 ± 1	0	0
$\eta\ell\nu$	$\eta'\ell\nu$	54 ± 2	12 ± 1	0.044 ± 0.058	0.23%

10.2 Combined $B \to \pi\ell\nu$ branching fraction

Measured partial and total branching fractions for $B^0 \to \pi^-\ell^+\nu$ and $B^+ \to \pi^0\ell^+\nu$ are combined assuming isospin symmetry:

$$\Gamma(B^0 \to \pi^-\ell^+\nu) = 2 \times \Gamma(B^+ \to \pi^0\ell^+\nu). \tag{10.1}$$

The ratio of decay widths is the inverse of the ratio of lifetimes $\tau_{B^+}/\tau_{B^0} = 1.071 \pm 0.009$ [9]; thus:

$$\mathcal{B}(B^0 \to \pi^-\ell^+\nu) = (1.867 \pm 0.016) \times \mathcal{B}(B^+ \to \pi^0\ell^+\nu). \tag{10.2}$$

and analogous for the partial branching fractions.

The $B^0 \to \pi^-\ell^+\nu$ and $B^+ \to \pi^0\ell^+\nu$ branching fractions are averaged to minimize the total uncertainty on the combined branching fraction.[2] Statistical uncertainties are considered uncorrelated; each component of the systematic uncertainty in the $\pi^-\ell^+\nu$ mode is conservatively assumed to be fully correlated with the corresponding component in the $\pi^0\ell^+\nu$ mode, with the exception of the uncertainties from f_{00} (which are anticorrelated). The statistical uncertainty from the yield extraction is taken to scale with the square root of the central value; systematic uncertainties associated with background modeling—branching fractions, shape function, $B\overline{B}$ background $\cos^2\phi_B$ shape and continuum background—are taken not to vary; all other uncertainties are taken to scale linearly.

The result is given in Table 10.1. Partial branching fractions compared to several form factor calculations are shown in Figure 10.1.

[2] In the case of asymmetric (systematic) uncertainty, the average uncertainty is minimized.

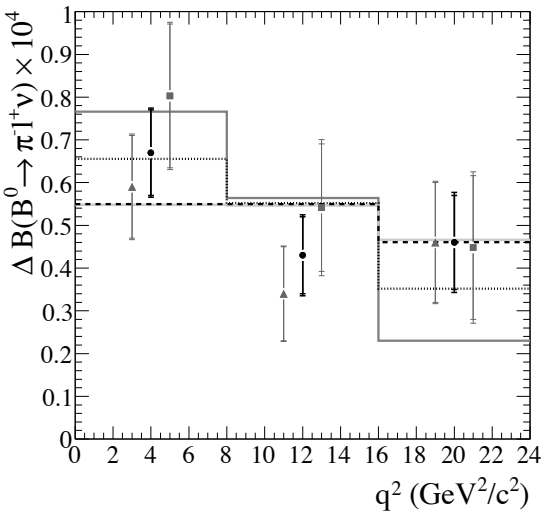

Figure 10.1: Decay spectrum for $B^0 \to \pi^- \ell^+ \nu$, in three bins of q^2, as measured by $B^0 \to \pi^- \ell^+ \nu$ (triangles) and $B^+ \to \pi^0 \ell^+ \nu$ decays (squares), and combined (circles); statistical (inner error bars) and total (outer) uncertainties are shown. Underlaid are theoretical calculations, scaled to the measured total branching fraction: Ball & Zwicky (light grey) [26], ISGW2 ((dark) grey) [27], HPQCD (dotted) [25] and FNAL (dashed) [24].

10.3 Upper limits for $\mathcal{B}(B^+ \to \eta' \ell \nu)$

Branching fractions for $B^+ \to \eta' \ell \nu$ are measured to be consistent with zero; 90% upper limits are calculated. For the total and partial branching fractions, the appropriate likelihood (Equation 8.4) as a function of the extracted signal yield is translated into a likelihood of the branching fraction. This likelihood is smeared by a Gaussian resolution function whose width $\sigma(y)$ represents all other uncertainties,[3] which scale with the branching fraction y as described as in §10.2; the smeared likelihood is given by

$$\tilde{L}(x) = \int L(y) \frac{e^{-\frac{(x-y)^2}{2\sigma^2(y)}}}{\sigma(y)\sqrt{2\pi}} dy. \tag{10.3}$$

The 90% confidence upper limit is the branching fraction z such that

$$\frac{\int_0^z \tilde{L}(x)dx}{\int_0^\infty \tilde{L}(x)dx} = 0.9, \tag{10.4}$$

[3]For simplicity, the uncertainties are symmetrized by averaging.

i.e., this is a Bayesian confidence limit with a flat prior in the physical ($z \geq 0$) region;

$$\Delta\mathcal{B}(B^+ \to \eta'\ell^+\nu) < 0.37 \times 10^{-4} \quad q^2 < 16 \ \mathrm{GeV}^2/c^2 \tag{10.5}$$

and

$$\mathcal{B}(B^+ \to \ell^+\eta'\nu) < 0.47 \times 10^{-4}. \tag{10.6}$$

The ratio of the branching fractions of the η' and η decays is measured to be

$$\frac{\mathcal{B}(B^+ \to \eta'\ell^+\nu)}{\mathcal{B}(B^+ \to \eta\ell^+\nu)} = 0.063 \pm 0.381 \pm 0.057, \tag{10.7}$$

with the first uncertainty statistical and the second systematic, or, using a method analogous to that described above and taking all correlations between $\eta\ell\nu$ and $\eta'\ell\nu$ branching fractions into account, cp. §10.2,

$$\frac{\mathcal{B}(B^+ \to \eta'\ell^+\nu)}{\mathcal{B}(B^+ \to \eta\ell^+\nu)} < 0.57 \tag{10.8}$$

to 90% confidence.

10.4 Extraction of $|V_{ub}|$

The $B^0 \to \pi^-\ell^+\nu$ differential decay rate, in the massless lepton limit, is given by

$$\frac{d\Gamma}{dq^2}(B^0 \to \pi^-\ell^+\nu) = \frac{G_{\mathrm{F}}^2|V_{ub}|^2}{192\pi^3 m_{B^0}^3}\lambda^{3/2}(q^2)|f_+^\pi(q^2)|^2, \tag{10.9}$$

where $\lambda(q^2) \equiv (q^2 + m_{B^0}^2 - m_\pi^2)^2 - 4m_{B^0}^2 m_\pi^2$ and f_+^π as described in §2.3 is a form factor containing QCD physics; thus the precision to $|V_{ub}|$ can be determined is from the measured (partial) branching fractions is limited by knowledge of the reduced decay rates $\Delta\zeta$:

$$\Delta\zeta(q^2_{\mathrm{min}}, q^2_{\mathrm{max}}) \equiv \int_{q^2_{\mathrm{min}}}^{q^2_{\mathrm{max}}} \frac{G_{\mathrm{F}}^2}{192\pi^3 m_{B^0}^3}\lambda^{3/2}(q^2)|f_+^\pi(q^2)|^2 dq^2. \tag{10.10}$$

Specifically,

$$|V_{ub}| = \sqrt{\frac{\Delta\mathcal{B}}{\tau_{B^0}\Delta\zeta}}, \tag{10.11}$$

where $\Delta\mathcal{B}$ and $\Delta\zeta$ are taken over the same q^2 range, and $\tau_{B^0} = 1.530 \pm 0.009\,\mathrm{ps}^{-1}$ [9].

Four calculations of f_+^π discussed in §2.3 are used to extract $|V_{ub}|$: Ball & Zwicky [26],

Table 10.3: Results for $|V_{ub}|$ using various form factor calculations and q^2 ranges (which are given in GeV^2/c^2).

FF model	q^2 range	$\Delta\zeta$ (ps^{-1})	$\lvert V_{ub}\rvert$ (10^{-3})
$B \to \pi\ell\nu$			
Ball & Zwicky	< 16	5.44 ± 1.43	$3.61 \pm 0.22 \pm 0.09^{+0.59}_{-0.40}$
HPQCD	> 16	2.07 ± 0.57	$3.79 \pm 0.44 \pm 0.16^{+0.66}_{-0.43}$
FNAL	> 16	1.83 ± 0.50	$4.03 \pm 0.47 \pm 0.17^{+0.70}_{-0.46}$
APE	> 16	1.80 ± 0.86	$4.07 \pm 0.47 \pm 0.17^{+1.56}_{-0.72}$
$B \to \pi\ell\nu$			
Ball & Zwicky	full	7.74 ± 2.32	$3.61 \pm 0.20 \pm 0.10^{+0.70}_{-0.44}$
HPQCD	full	9.10 ± 3.13	$3.33 \pm 0.19 \pm 0.09^{+0.78}_{-0.46}$
FNAL	full	6.24 ± 2.12	$4.02 \pm 0.23 \pm 0.11^{+0.93}_{-0.55}$
APE	full	7.0 ± 2.9	$3.79 \pm 0.21 \pm 0.11^{+1.16}_{-0.60}$
Ball & Jones			
$B^+ \to \eta\ell^+\nu$	< 16	2.41 ± 0.42	$3.32 \pm 0.57^{+0.08+0.34}_{-0.09-0.26}$

HPQCD [25], FNAL [24] and APE [21]. The extraction via the light cone sum rules calculation (Ball & Zwicky) is done using the partial branching fraction over the $0 \leq q^2 < 16\ \mathrm{GeV}^2/c^2$ range, while extraction via the three lattice QCD calculations is done over $q^2 \geq 16\ \mathrm{GeV}^2/c^2$, the respective regimes in which these form factor calculations are held to be valid. The four extractions are repeated using the total branching fraction.[4]

Though the Ball & Jones [29] calculation of f_+^η is not yet mature, as an exercise, it is also used to extract $|V_{ub}|$ from the $B^+ \to \eta\ell^+\nu$ branching fraction over the $0 \leq q^2 < 16\ \mathrm{GeV}^2/c^2$ range, using an analogue of Equation 10.11 and taking $\tau_{B^+} = 1.638 \pm 0.011\,\mathrm{ps}^{-1}$ [9]. The corresponding calculation of $f_+^{\eta'}$ is not used to determine $|V_{ub}|$, as $\Delta\mathcal{B}(B^+ \to \eta'\ell^+\nu)$ is measured to be negative for the $0 \leq q^2 < 16\ \mathrm{GeV}^2/c^2$ range.

Appropriate reduced decay rates and associated uncertainties are provided by the authors of the respective form factor calculations, with the exception of that due to Ball and Jones. The various results for $|V_{ub}|$ are given in Table 10.3.

[4]Each form factor calculation is accepted as valid only in a specific range of q^2; however, with assumptions about an (approximate) analytic form for f_+^π, results can be extrapolated to a total reduced decay rate. This is something of an exercise; the associated theoretical uncertainties on $|V_{ub}|$ tend to be larger.

Chapter 11

Cross-checks

To affirm the robustness of the analysis method, it is repeated with various changes:

1. The tag side lepton must be an electron.
2. The tag side lepton must be a muon.
3. The signal side lepton must be an electron.
4. The signal side lepton must be a muon.
5. The tag side lepton must have no less than $1\,\mathrm{GeV}/c$ absolute momentum.
6. The tag side lepton must have no less than $1.2\,\mathrm{GeV}/c$ absolute momentum.
7. The signal side lepton must have no less than $1.2\,\mathrm{GeV}/c$ absolute momentum.
8. The signal side lepton must have no less than $1.2\,\mathrm{GeV}/c$ absolute momentum.
9. The D mass peak region window is narrowed to 2.2σ.
10. The D mass peak region window is widened to 3σ.
11. Events with K^0_S candidates are not rejected.
12. Different criteria are used to identify looper and ghost tracks,[1] namely:
    - for like charge loopers, $p_\mathrm{t} < 180\,\mathrm{MeV}/c$, $|\Delta p_\mathrm{t}| < 100\,\mathrm{MeV}/c$, $|\Delta\phi| < 0.22$ and $|\Delta\theta| < 0.215$;

[1] See §6, Footnote 7.

- for opposite charge loopers, $p_t < 180\,\mathrm{MeV}/c$, $|\Delta p_t| < 100\,\mathrm{MeV}/c$, $|\Delta\phi| < 0.19$ and $|\Delta\theta| < 0.3$; and
- for ghosts, $p_t < 350\,\mathrm{MeV}/c$, $|\Delta p_t| < 100\,\mathrm{MeV}/c$, $|\Delta\phi| < 0.22$ and $|\Delta\theta| < 0.215$.

13. Neutral clusters must have lateral moment less than 0.6.
14. Neutral clusters must have $\Delta\alpha \geq 0.80$ separation from tracks.
15. Both #13 and #14.
16. Neutral clusters must have more than 50 MeV (laboratory frame) energy.
17. Neutral clusters must have more than 100 MeV (laboratory frame) energy.
18. There must be no (less than 90 MeV) extra neutral energy for $B^0\overline{B}^0$ (B^+B^-) events.
19. There must be less than 170 MeV (290 MeV) extra neutral energy for $B^0\overline{B}^0$ (B^+B^-) events.
20. Events with J/ψ candidates are not rejected.
21. Leptons must have like charge.
22. Leptons must have opposite charge.
23. Yield is extracted over $0 \leq \cos^2\phi_B < 15$.
24. Yield is extracted over $0 \leq \cos^2\phi_B < 30$.
25. The η meson is reconstructed only via the decay $\eta \to \gamma\gamma$.
26. The η meson is reconstructed only via the decay $\eta \to \pi^+\pi^-\pi^0$.
27. The η meson is reconstructed only via the decay $\eta \to \pi^0\pi^0\pi^0$.

Figures 11.1–11.3 present the results of these cross-checks as fractional deviations, i.e., for a given signal mode and q^2 bin, $(\tilde{N}/N) - 1$, where $\tilde{N}$ and N are partial branching fractions measured in the cross-check and primary analyses respectively. As the cross-check samples tend to be largely subsets or supersets of the data selected for the primary analysis, in calculating the uncertainties on the fractional deviations, the correlation coefficient $\rho_{\tilde{N},N}$ is assumed to be $\sigma_{\tilde{N}}/\sigma_N$ or its inverse (whichever is not greater than unity). Uncertainties considered are statistical only.

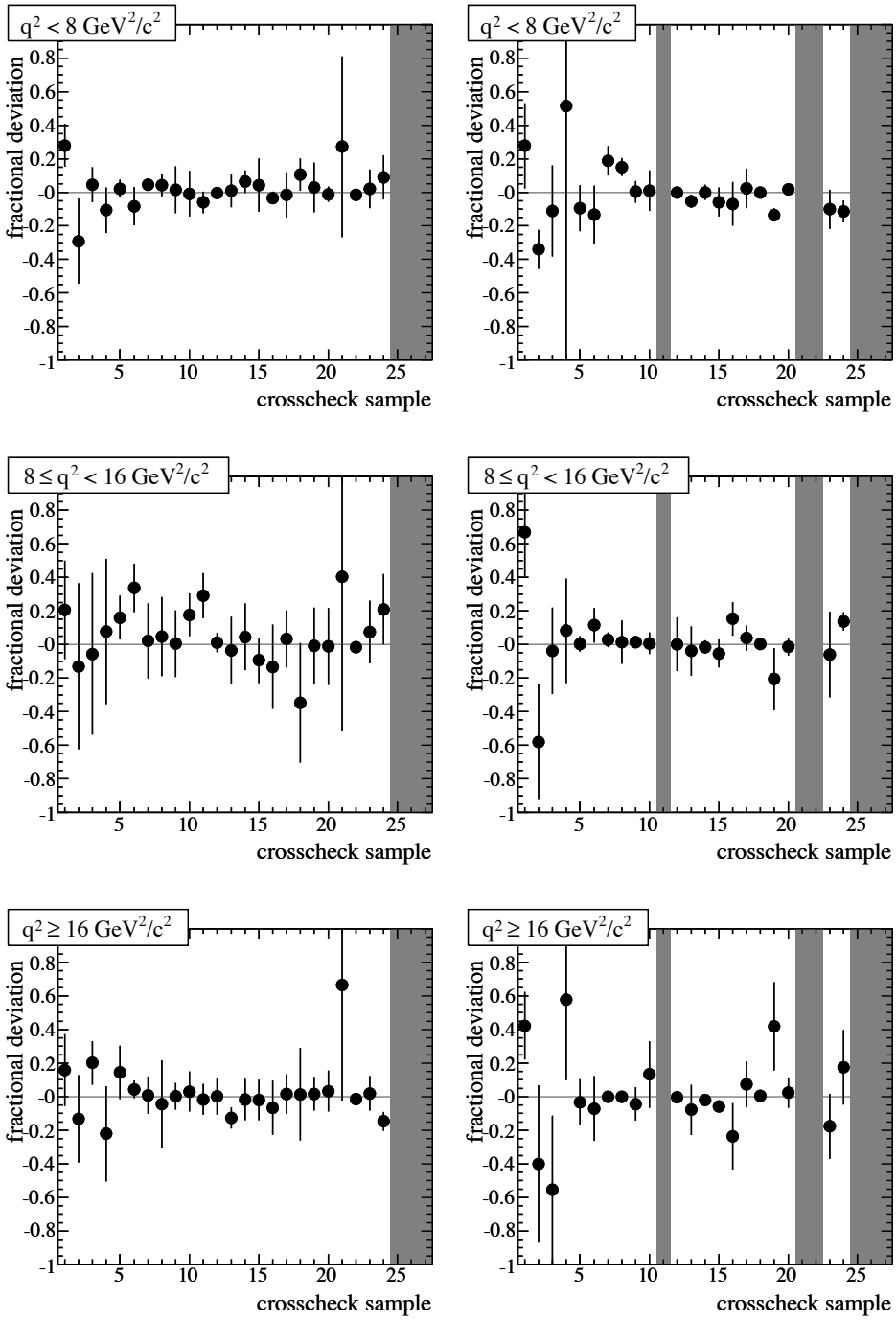

Figure 11.1: Branching fraction results of cross-check analyses for $\pi^{\pm}\ell\nu$ (left) and $\pi^0\ell\nu$ (right) for low (top), intermediate (middle) and high (bottom) q^2 bins. Values on the $\hat{x}$-axis are defined in §11; results are expressed as fractional deviation from nominal values; uncertainties are statistical only. Shaded regions indicate cross-checks not applicable for the given mode.

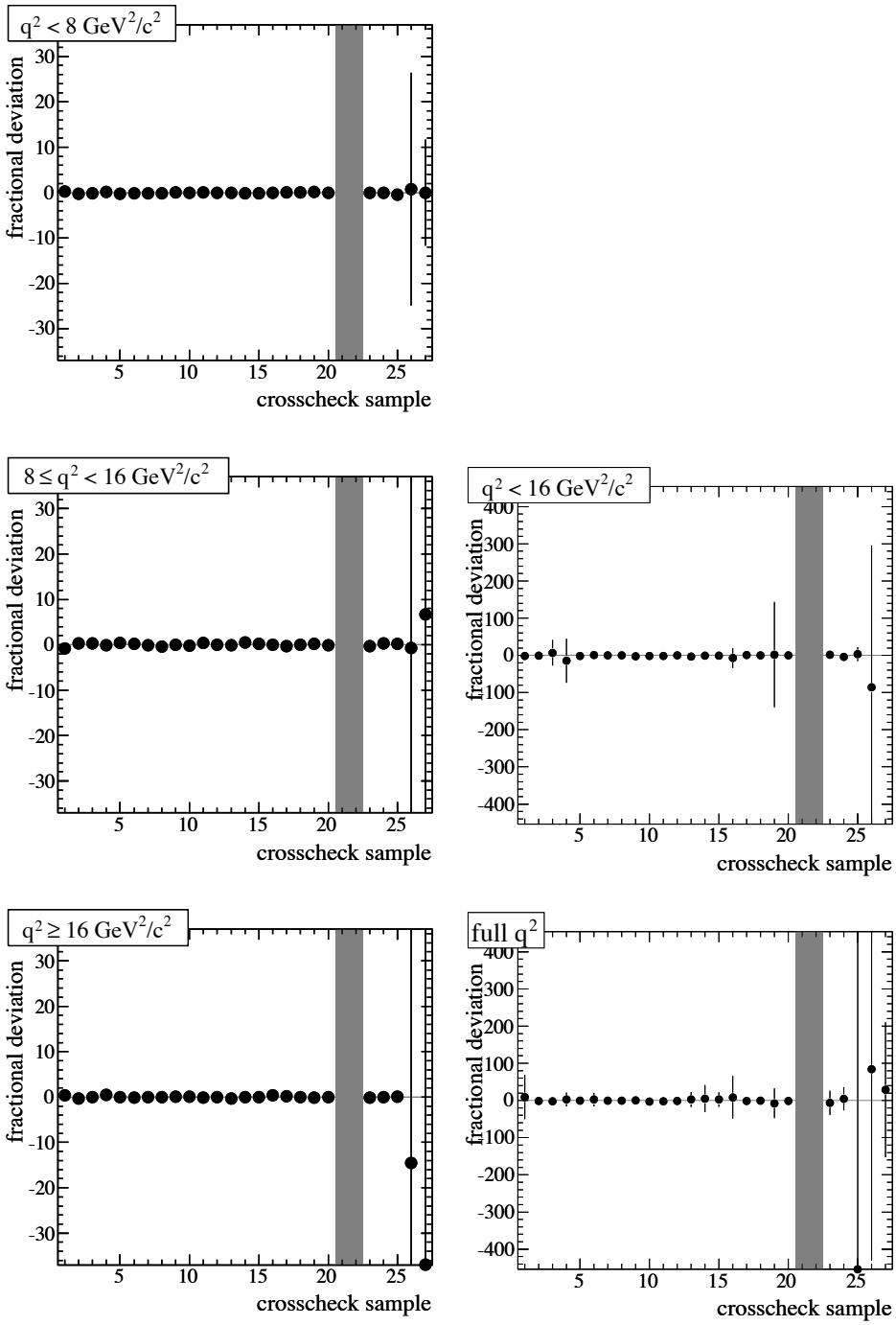

Figure 11.2: Analogous to Figure 11.1 for $\eta\ell\nu$ signal mode (left); for $\eta'\ell\nu$ signal mode (right), results of cross-check analyses for $q^2 < 16$ GeV$^2/c^2$ bin (middle) and over full q^2 range (bottom) are shown.

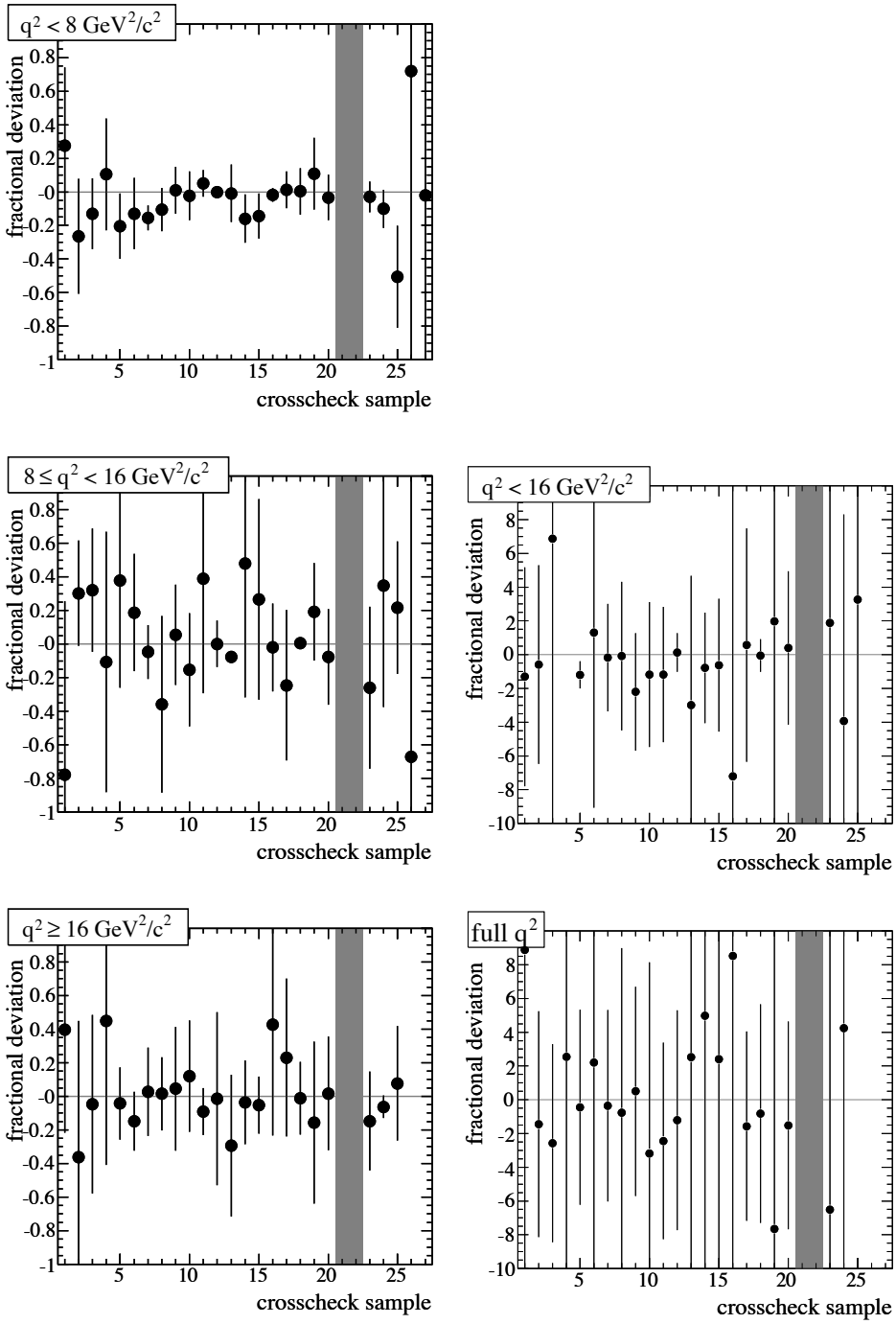

Figure 11.3: Close-up of Figure 11.2: result of of cross-check analyses for $\eta\ell\nu$ (left) and $\eta'\ell\nu$ (right) signal modes. In $\eta\ell\nu$ ($\eta'\ell\nu$) plots, points with absolute value greater than unity (ten) have been removed.

As expected, the results are clustered around zero, with statistical deviations. Cross-check #27 fails for the partial $\eta'\ell\nu$ branching fraction; the reconstruction of $\eta' \to \eta\pi\pi$ through $\eta \to \pi^0\pi^0\pi^0$ has a low enough efficiency that, up to statistics, the efficiency matrix (analogous to Equation 7.7) is not invertible.

Chapter 12

Discussion

The pionic branching fractions measured are consistent with the world averages.[1] They represent a roughly 30% improvement in precision over the previous *BABAR* measurements in this channel [18] and are competitive with other measurements [16]; no current tagged measurement is measurably better. The branching fraction for $B^+ \to \eta \ell^+ \nu$, which has heretofore not been measured with statistical significance, is measured to 3.2σ. The lack of signal in the $B^+ \to \eta' \ell^+ \nu$ channel directly contradicts a recently published measurement [45]. These comparisons are summarized in Figure 12.1.

These measurements are still statistics limited. The *BABAR* experiment completed data taking at the $\Upsilon(4S)$ resonance in December 2007, accumulating a total data set of $433\,\mathrm{fb}^{-1}$; an update of the analyses presented in this Dissertation to include this full data set can be expected to improve statistical uncertainties by 12%.[2] An earlier measurement of $\mathcal{B}(B \to \pi \ell \nu)$ using fully hadronically reconstructed (recoil) B mesons[3] [18] suggests comparable uncertainties; the statistical independence of measurements in these two channels could provide an almost 40% improvement when combining tagged measurements over the full *BABAR* data set. One might optimistically hope to observe (with 5σ significance) the decay $B^+ \to \eta \ell^+ \nu$ using tagged measurements alone. Knowledge of these branching fractions can only improve as these results are combined with present and future measurements in these and

[1] World averages do not include the results presented in this Dissertation.

[2] This translates, with the assumption that the systematic uncertainties are unchanged, to a 8% (10%) increase in total precision on $\mathcal{B}(B^0 \to \pi^- \ell^+ \nu)$ ($\mathcal{B}(B^+ \to \eta^{(\prime)} \ell^+ \nu)$).

[3] See §2.2.

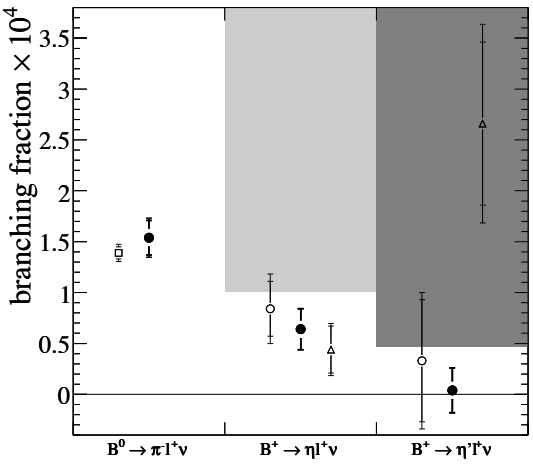

Figure 12.1: Total branching fractions measured (filled circles). Also shown are the $B^0 \to \pi^-\ell^+\nu$ world average (square) [16], $B^+ \to \eta\ell^+\nu$ and $B^+ \to \eta'\ell^+\nu$ results from the *BABAR* analysis with full hadronic recoil B reconstruction (open circles) [46] and a recent CLEO publication (squares) [45]. Statistical (inner error bars) and total (outer) uncertainties are shown. Shaded regions are excluded with 90% confidence by CLEO ((dark) grey) and this measurement (light grey).

other[4] channels, at *BABAR* and elsewhere.

Figure 12.2 shows $|V_{ub}|$ as extracted from measured $B \to \pi\ell\nu$ partial branching fractions and several form factor calculations, compared to the corresponding values as determined from the partial branching fraction world average. Uncertainties are heavily dominated by those from form factor calculations; improvement is expected. Also shown are the world average values of $|V_{ub}|$ as measured from inclusive $b \to u\ell\nu$ decays,[5] combining inclusive[6] and exclusive experimental results and from a fit of the position of the Unitarity Triangle apex $(\overline{\rho}, \overline{\eta})$ using all known constraints,[7] including β. These values are all in good agreement.

[4]It is more difficult to project the precision of future untagged measurements [19] as, given the sizes of data sets at today's collider experiments, they are becoming increasingly limited by systematic uncertainties, as large potential backgrounds exist and must be well described.

[5]See Figure 2.2.

[6]The "inclusive" results cited here and in Figure 2.2 are newer than the "combined" and "CKM" results, which were computed using an older inclusive average ($|V_{ub}| = (4.31 \pm 0.17 \pm 0.35) \times 10^{-3}$, with the first uncertainty experimental and the second theoretical) that used shape function parameters derived from $b \to s\gamma$ and $b \to c\ell\nu$ spectra. See §5, Footnote 13.

[7]See Figure 1.1.

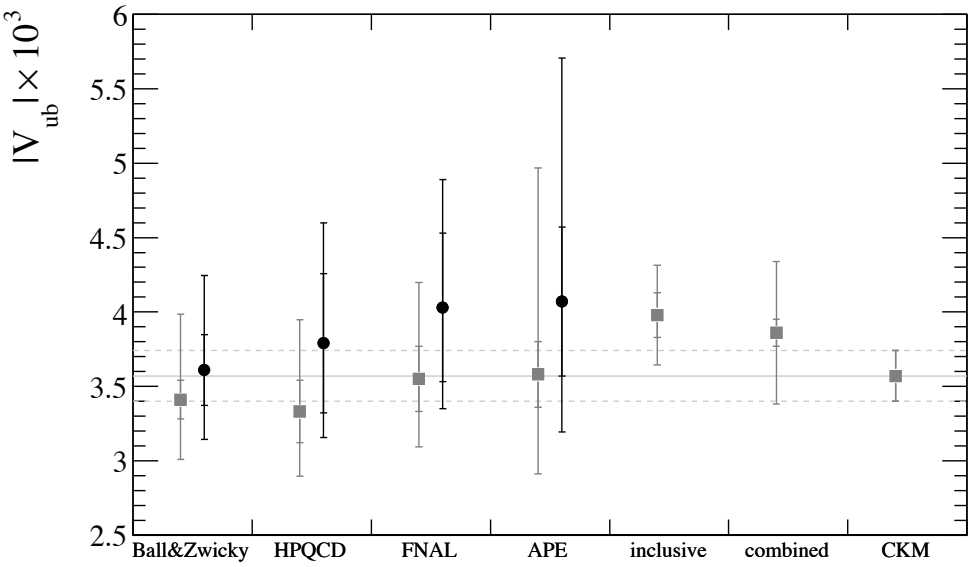

Figure 12.2: Values of $|V_{ub}|$ as extracted from measurements presented in this Dissertation (circles) and current world averages (squares) [11, 16]. Where two sets of error bars are shown, inner (outer) error bars represent experimental (total) uncertainty. See text for details.

Chapter 13

Conclusions

The following partial branching fractions for charmless semileptonic decays, where the first uncertainty given is statistical and the second systematic, have been measured:

$$\Delta\mathcal{B}(B^0 \to \pi^-\ell^+\nu) = \begin{cases} (0.59 \pm 0.12 \pm 0.03) \times 10^{-4} & q^2 < 8 \ \text{GeV}^2/c^2 \\ (0.34 \pm 0.11 \pm 0.02) \times 10^{-4} & 8 \leq q^2 < 16 \ \text{GeV}^2/c^2 \\ (0.46 \pm 0.14 \pm 0.03) \times 10^{-4} & q^2 > 16 \ \text{GeV}^2/c^2, \end{cases} \tag{13.1}$$

$$\Delta\mathcal{B}(B^+ \to \pi^0\ell^+\nu) = \begin{cases} (0.43 \pm 0.09 \pm 0.02) \times 10^{-4} & q^2 < 8 \ \text{GeV}^2/c^2 \\ (0.29 \pm 0.08 \pm 0.03) \times 10^{-4} & 8 \leq q^2 < 16 \ \text{GeV}^2/c^2 \\ (0.24 \pm 0.09 \pm 0.03) \times 10^{-4} & q^2 > 16 \ \text{GeV}^2/c^2, \end{cases} \tag{13.2}$$

$$\Delta\mathcal{B}(B^+ \to \eta\ell^+\nu) = \begin{cases} (0.28 \pm 0.10 \pm 0.01) \times 10^{-4} & q^2 < 8 \ \text{GeV}^2/c^2 \\ (0.16 \pm 0.11 \pm 0.01) \times 10^{-4} & 8 \leq q^2 < 16 \ \text{GeV}^2/c^2 \\ (0.21 \pm 0.13^{+0.02}_{-0.01}) \times 10^{-4} & q^2 > 16 \ \text{GeV}^2/c^2 \end{cases} \tag{13.3}$$

and

$$\Delta\mathcal{B}(B^+ \to \eta'\ell^+\nu) = (-0.05 \pm 0.22^{+0.04}_{-0.06}) \times 10^{-4} \quad q^2 < 16 \ \text{GeV}^2/c^2 \tag{13.4}$$

as well as the total branching fractions:

$$\mathcal{B}(B^0 \to \pi^-\ell^+\nu) = (1.38 \pm 0.21 \pm 0.07) \times 10^{-4}, \tag{13.5}$$

$$\mathcal{B}(B^+ \to \pi^0\ell^+\nu) = (0.96 \pm 0.15 \pm 0.07) \times 10^{-4}, \tag{13.6}$$

$$\mathcal{B}(B^+ \to \eta\ell^+\nu) = (0.64 \pm 0.20 \pm 0.03) \times 10^{-4} \text{ and} \tag{13.7}$$

$$\mathcal{B}(B^+ \to \eta'\ell^+\nu) = (0.04 \pm 0.22^{+0.05}_{-0.02}) \times 10^{-4}. \tag{13.8}$$

This represents first evidence of the $B^+ \to \eta \ell^+ \nu$ decay, with 3.2σ significance.

The $B^+ \to \eta' \ell^+ \nu$ branching fractions are consistent with zero; upper limits

$$\Delta\mathcal{B}(B^+ \to \eta' \ell^+ \nu) < 0.37 \times 10^{-4} \quad q^2 < 16 \ \text{GeV}^2/c^2, \tag{13.9}$$

$$\mathcal{B}(B^+ \to \eta' \ell^+ \nu) < 0.47 \times 10^{-4} \text{ and} \tag{13.10}$$

$$\frac{\mathcal{B}(B^+ \to \eta' \ell^+ \nu)}{\mathcal{B}(B^+ \to \eta \ell^+ \nu)} < 0.57 \tag{13.11}$$

are set with 90% confidence.

The pionic branching fractions are combined, assuming isospin symmetry, to obtain

$$\Delta\mathcal{B}(B^0 \to \pi^- \ell^+ \nu) = \begin{cases} (0.67 \pm 0.10 \pm 0.03) \times 10^{-4} & q^2 < 8 \ \text{GeV}^2/c^2 \\ (0.43 \pm 0.09 \pm 0.03) \times 10^{-4} & 8 \le q^2 < 16 \ \text{GeV}^2/c^2 \\ (0.46 \pm 0.11 \pm 0.04) \times 10^{-4} & q^2 > 16 \ \text{GeV}^2/c^2 \end{cases} \tag{13.12}$$

and

$$\mathcal{B}(B^0 \to \pi^- \ell^+ \nu) = (1.54 \pm 0.17 \pm 0.09) \times 10^{-4}. \tag{13.13}$$

Combined with various calculations of the $B \to \pi \ell \nu$ form factor, this translates to $|V_{ub}|$ between 3.61 and 4.07×10^{-3}.

Bibliography

[1] M. Spiropulu (2000). *A Blind Search for Supersymmetry in $p\overline{p}$ Collisions at $\sqrt{s} = 1.8\,\mathrm{TeV}$ using the Missing Energy plus Multijet channel*. Ph.D. thesis. Harvard University, Cambridge, Massachusetts.

[2] C. L. O'Connell (2005). *Plasma Production via Field Ionization*. Ph.D. thesis. Stanford University, Palo Alto, California.

[3] A. T. Holloway (2006). *The First Direct Limit on the t Quark Lifetime*. Ph.D. thesis. Harvard University, Cambridge, Massachusetts.

[4] M. A. Mazur (2007). *Study of Exclusive Semileptonic B Meson Decays to Tau Leptons*. Ph.D. thesis. University of California, Santa Barbara, California.

[5] S. Weinberg, *A Model of Leptons*. Phys. Rev. Lett. **19** (1967) 1264.
A. Salam, *Elementary Particle Theory*. Almquist & Wiksells (1969) Stockholm.
S. L. Glashow, J. Iliopoulos & L. Maiani, *Weak Interactions with Lepton-Hadron Symmetry*. Phys. Rev. D **2** (1970) 1285.

[6] N. Cabibbo, *Unitary Symmetry and Leptonic Decays*. Phys. Rev. Lett. **10** (1963) 531.
M. Kobayashi & T. Maskawa, *CP Violation in the Renormalizable Theory of Weak Interaction*. Prog. Theor. Phys. **49** (1973) 652.

[7] J. H. Christenson & al., *Evidence for the 2π Decay of the K_2^0 Meson*. Phys. Rev. Lett. **13** (1964) 138.

[8] Z. Maki, M. Nakagawa & S. Sakata, *Remarks on the Unified Model of Elementary Particles*. Prog. Theor. Phys. **28** (1962) 870.

[9] W.-M. Yao & al. (Particle Data Group), *The Review of Particle Physics*. J. Phys. **G33** (2006) 1.

[10] L. Wolfenstein, *Parametrization of the Kobayashi-Maskawa Matrix*. Phys. Rev. Lett. **51** (1983) 1945.

[11] J. Charles & al. (CKMFitter Group), *CP Violation and the CKM Matrix: Assessing the Impact of the Asymmetric B Factories*. Eur. Phys. Jour. C **41** (2005) 1.
Update (summer 2007): `http://ckmfitter.in2p3.fr`.

[12] The *BABAR* Collaboration, B. Aubert & al., *Improved Measurement of CP Violation in Neutral B Decays to $c\overline{c}s$*. Phys. Rev. Lett. **99** (2007) 171803.

[13] The *BABAR* Collaboration, B. Aubert & al., *Measurement of the Inclusive Electron Spectrum in Charmless Semileptonic B Decays Near the Kinematic Endpoint and Determination of $|V_{ub}|$*. Phys. Rev. D **73** (2006) 012006.

[14] The *BABAR* Collaboration, B. Aubert & al., *Determination of $|V_{ub}|$ from Measurements of the Electron and Neutrino Momenta in Inclusive Semileptonic B Decays*. Phys. Rev. Lett. **95** (2005) 111801.
Erratum: ibid. **97** (2006) 019903.

[15] The *BABAR* Collaboration, B. Aubert & al., *Measurements of Partial Branching Fractions for $\overline{B} \to X_u \ell \overline{\nu}$ and Determination of $|V_{ub}|$*. `arXiv:0708.3702v1`, 28 August 2007.

[16] E. Barberio & al. (Heavy Flavor Averaging Group), *Averages of b-hadron properties at the end of 2006*. `hep-ex/arXiv:0704.3575v1`, 26 April 2007.
Update (Lepton Photon 2007): `http://www.slac.stanford.edu/xorg/hfag`.

[17] B. O. Lange & al., *Theory of Charmless Inclusive B Dceays and the Extraction of V_{ub}*. Phys. Rev. D **72** (2005) 073006.
This is an update of [38].

[18] The *BABAR* Collaboration, B. Aubert & al., *Measurement of the $B \to \pi \ell \nu$ Branching Fraction and Determination of $|V_{ub}|$ with Tagged B Mesons*. Phys. Rev. Lett. **97** (2006) 211801.

[19] The *BABAR* Collaboration, B. Aubert & al., *Measurement of the $B^0 \to \pi \ell \nu$ Form-Factor Shape and Branching Fraction, and Determination of $|V_{ub}|$ with a Loose Neutrino Reconstruction Technique*. Phys. Rev. Lett. **98** (2007) 091801.

[20] F. J. Gilman & R. L. Singleton, *Analysis of semileptonic decays of mesons containing heavy quarks*. Phys. Rev. D **41** (1990) 142.

[21] A. Abada & al. (APE Collaboration), *Heavy $\to$ Light semileptonic decays of pseudoscalar mesons from lattice QCD*. Nucl. Phys. B **619** (2001) 565.

[22] D. Bećirević & A. Kaidalov, *Comment on the heavy $\to$ light form factors*. Phys. Lett. B **478** (2000) 417.

[23] T. Becher & R. J. Hill, *Comment on form factor shape and extraction of $|V_{ub}|$ from $B \to \pi \ell \nu$*. Phys. Lett. B **633** (2006) 61.

[24] M. Okamoto & al. (FNAL Collaboration), *Semileptonic $D \to \pi/K$ and $B \to \pi/D$ decays in $2+1$ flavor lattice QCD*. Nucl. Phys. Proc. Suppl. **140** (2005) 461.

[25] E. Gulez & al. (HPQCD Collaboration), *B Meson Semileptonic Form Factors from Unquenched Lattice QCD*. Phys. Rev. D **73** (2006) 074502.
Erratum: ibid. **75** (2007) 119906.

[26] P. Ball & R. Zwicky, *New results on $B \to \pi, K, \eta$ decay form factors from light-cone sum rules*. Phys. Rev. D **71** (2005) 014015;
P. Ball & R. Zwicky, *$B_{d,s} \to \rho, \omega, K^*, \phi$ decay form factors from light-cone sum rules reexamined*. Phys. Rev. D **71** (2005) 014029.

[27] D. Scora & N. Isgur, *Semileptonic meson decays in the quark model: An update*. Phys. Rev. D **52** (1995) 2783.

[28] C. S. Kim & al., *$B \to \eta' \ell \nu$ decays and the flavor-singlet form factor*. Phys. Lett. B **590** (2004) 223.

[29] P. Ball & G. W. Jones, *$B \to \eta^{(\prime)}$ Form Factors in QCD*. JHEP **08** (2007) 25.

[30] The *BABAR* Collaboration, B. Aubert & al., *The BABAR detector*. Nucl. Instrum. Methods Phys. Res., Sect. A **479** (2002) 1.

[31] D. J. Lange, *The* `EvtGen` *particle decay simulation package*. Nucl. Instrum. Methods Phys. Res., Sect. A **462** (2001) 152.

[32] S. Agostinelli & al. (GEANT Collaboration), `GEANT4`—*a simulation toolkit*. Nucl. Instrum. Methods Phys. Res., Sect. A **506** (2003) 250.

[33] The *BABAR* Collaboration, *Measurement of the* $B^+ \to \eta\ell^+\nu$ *and* $B^+ \to \eta'\ell^+\nu$ *Branching Fractions using* $\Upsilon(4S) \to B\overline{B}$ *Events Tagged by a Fully Reconstructed B Meson*. `arXiv:hep-ex/0607066v1`, 26 July 2006.

[34] C. Schwanda & al. (Belle Collaboration), *Evidence for* $B^+ \to \omega l^+\nu$. Phys. Rev. Lett. **93** (2004) 131803.

[35] The *BABAR* Collaboration, *Measurement of the Relative Branching Fractions of* $\overline{B} \to D/D^*/D^{**}\ell^-\overline{\nu}_\ell$ *Decays in Events with a Fully Reconstructed B Meson*. `arXiv:hep-ex/0703027v1`, 16 March 2007.

[36] The *BABAR* Collaboration, *Measurement of the Decay* $B^- \to D^{*0}e^-\overline{\nu}_e$. `arXiv:0707.2655v1`, 18 July 2007.

[37] The *BABAR* Collaboration, *Measurement of Semileptonic B Decays into Orbitally-Excited Charm Mesons*. *BABAR* Analysis Document #1565 (internal), presented at ICHEP 2006.

[38] De Fazio & Neubert, $B \to X_u\ell\overline{\nu}_\ell$ *decay distributions to order* α_s. JHEP **9906** (1999) 017.

[39] O. Buchmüller & H. Flächer, *Fit to Moments of Inclusive* $B \to X_c\ell\nu$ *and* $B \to X_s\gamma$ *Decay Distributions using Heavy Quark Expansions in the Kinetic Scheme*. Phys. Rev. D **73** (2006) 073008.

[40] T. Sjöstrand, *High-Energy-Physics Event Generation with* `Pythia5.7` *and* `Jetset7.4`. Comput. Phys. Commun. **82** (1994) 74.

[41] I. Caprini, L. Lellouch & M. Neubert, *Dispersive bounds on the shape of* $\overline{B} \to D^*\ell\overline{\nu}$ *form factors*. Nucl. Phys. B **530** (1998) 153.

[42] G. C. Fox & S. Wolfram, *Observables for the Analysis of Event Shapes in* e^+e^- *Annihilation and Other Processes*. Phys. Rev. Lett. **41** (1978) 1581.

[43] K. Cranmer, *Kernel Estimation in High-Energy Physics*. Comput. Phys. Commun. **136** (2001) 198.

[44] E. Barberio & Z. Was, `PHOTOS`*: A Universal Monte Carlo for QED radiative corrections. Version 2.0*. Comput. Phys. Commun. **79** (1994) 291.

[45] N. E. Adam & al. (CLEO Collaboration), *A Study of Exclusive Charmless Semileptonic B Decay and* $|V_{ub}|$. Phys. Rev. Lett. **99** (2007) 041802.

[46] The *BABAR* Collaboration, B. Aubert & al., *Measurement of the* $B^+ \to \eta\ell^+\nu$ *and* $B^+ \to \eta'\ell^+\nu$ *branching fractions using* $\Upsilon(4S) \to B\overline{B}$ *events tagged by a fully reconstructed B meson*. `arXiv:hep-ex/0607066`, 26 July 2006.